TECHNISCHE UNIVERSITÄT WIEN

DISSERTATION

Characterization and modeling of micro/substructure evolution in aluminum alloy

Carried out for the purpose of obtaining the degree of Doctor technicae (Dr. techn.),
under the supervision of

Univ.-Prof. Dipl.-Ing. Dr.techn. Ernst Kozeschnik
E308
Institute of Materials Science and Technology

Submitted at TU Wien
Faculty of Mechanical and Industrial Engineering

by
MSc. Qi Yang
Mat.No.: 12045460

Vienna, October 2024

_____

Personal Signature

This dissertation has been reviewed by

Assoc.Prof. Dr.techn. Maria Cecilia Poletti
Institute of Materials Science, Joining and Forming, TU Graz.

Univ.-Prof. Dipl.-Ing. Dr.techn. Martin Stockinger
Chair of Metal Forming, University of Leoben.

Affidavit

I declare in lieu of oath, that I wrote this thesis and carried out the associated research myself, using only the literature cited in this volume. If text passages from sources are used literally, they are marked as such.

I confirm that this work is original and has not been submitted for examination elsewhere, nor is it currently under consideration for a thesis elsewhere.

I acknowledge that the submitted work will be checked electronically-technically using suitable and state-of-the-art means (plagiarism detection software). On the one hand, this ensures that the submitted work was prepared according to the high-quality standards within the applicable rules to ensure good scientific practice "Code of Conduct" at the TU Wien. On the other hand, a comparison with other student theses avoids violations of my personal copyright.

(Qi Yang)

Vienna, October 2024

Acknowledgment

First and foremost, I would like to express my appreciation and sincere thanks to my supervisor, Prof. Ernst Kozeschnik, who has provided me with excellent guidance and encouragement throughout the pursuit of this degree. The experiences and support I have gained from him have been both academically and personally precious.

A special thanks also goes to my dear colleagues Tomasz Wojcik, Helmut Oswald, and Heinz Kaminski for their selfless help and support in the sample preparation and experiments. My sincere thanks also go to the staff of the Laboratory at the Institute of Materials Science and Technology (WWWT), for their great help in my experiments and sample preparation. I am grateful to Robert Kahlenberg for his guidance and support upon my arrival in Vienna. I am also thankful to all my colleagues at TU Wien for the enjoyable experience.

I want to express my gratitude to TU Wien and the China Scholarship Council for providing me with the great opportunity to pursue my studies abroad, this experience has been a significant milestone in my life. It is both a pleasure and an honor to work in the WWWT at TU Wien.

Lastly and this is the most important, I want to thank my parents and family for their trust and support in my life journey.

"A calm and modest life brings more happiness than the pursuit of success combined with constant restlessness"

"Where there is a will, there is a way"

- Albert Einstein

List of Publications

Journal papers

[1] Q. Yang, T. Wojcik, and E. Kozeschnik. Continuous dynamic recrystallization and deformation behavior of an AA1050 aluminum alloy during high-temperature compression. Metals, 2024, vol. 14, pp. 889.

[2] Q. Yang, T. Wojcik and E. Kozeschnik. Subgrain size modeling and substructure evolution in an AA1050 aluminum alloy during high-temperature compression. Materials, 2024, vol. 17, pp. 4385.

[3] Q. Yang, T. Wojcik and E. Kozeschnik. A dislocation-based model for substructure evolution and flow stress of aluminum alloys during high-temperature compression. (submitted manuscript)

Conference presentations

[1] Q. Yang, T. Wojcik, and E. Kozeschnik. Characterization and modeling of continuous dynamic recrystallization and sub-grain size evolution during high-temperature compression of aluminum alloy, (oral presentation), MSE 2024, Darmstadt, Germany, 24. - 26.09.2024.

[2] Q. Yang, and E. Kozeschnik. Continuous dynamic recrystallization of aluminum alloy during high temperature compression deformation, (poster presentation), Thermec 23, Vienna, Austria, 02. - 08.07.2023.

Abstract

For materials with high stacking fault energy (SFE), such as aluminum alloys, dynamic recovery (DRV) and dynamic recrystallization (DRX) are critical softening mechanisms during plastic deformation, resulting in microstructural and substructural evolution.

This study investigates the effect of compression parameters on the microstructural evolution of an AA1050 aluminum alloy at elevated temperatures. The formation of well-defined substructures and the subsequent development of DRX grains indicate that recrystallization can occur during high-temperature compression. The mechanisms driving microstructural evolution and DRX are summarized by analyzing the flow stress, variations in misorientation angle, DRX fraction, and the distribution of subgrains and grain boundaries.

The mechanisms of subgrain generation, refinement, and coarsening are analyzed based on experimental investigations of microstructure and substructure. Two subgrain size evolution models (empirical and substructure-based) are applied with multiple internal state variables. These models successfully simulate average subgrain size, with both experimental and simulated results reproducing the thermo-mechanical behavior during continuous deformation.

Finally, the laws governing hot deformation and microstructural evolution are integrated into a dislocation-based model framework, which primarily includes the evolution of internal dislocation density, wall dislocation density, subgrain size, subgrain misorientation, and flow stress. This dislocation model is successfully applied to the microstructural evolution of AA1050 and other aluminum alloys under various deformation conditions.

Table of Contents

Section A

1. Introduction

In the past few decades, researchers [1-3] have extensively studied the microstructural evolution and recrystallization behavior of different materials in hot forming, including work hardening (WH), dynamic recovery (DRV), static recovery (SRV), dynamic recrystallization (DRX), grain growth, and other related microstructural evolutions [4-9]. These phenomena play a critical role in determining the final mechanical properties of Al alloys.

In materials with high stacking fault energy (SFE), DRV and continuous dynamic recrystallization (CDRX) are the main softening mechanisms during hot deformation, as observed in various series of Al alloys [10-14]. Low-angle subgrain boundaries, defined by misorientation angles between 2° and 15°, are formed by the absorption of mobile dislocations and gradually transform into high-angle grain boundaries (HAGBs) with misorientation angles exceeding 15° [15-17]. This process produces a well-defined substructure that favors subsequent DRX during high temperature deformation.

This study investigates the microstructural evolution of AA1050 aluminum alloy under different strains, temperatures, and strain rates through a single-pass isothermal compression process. The evolution of the microstructural mechanisms is evaluated by analyzing flow stress, misorientation angle variations, recrystallized grain distribution, etc.

Several modeling approaches have been developed to reproduce the microstructural evolution during the hot deformation, recovery, and recrystallization [7-9]. The present study has formulated a dislocation-based model based on experimental data, utilizing physically meaningful variables to capture the evolution of dislocation density, subgrain size, subgrain boundary misorientation, and flow stress.

This thesis is divided into two sections. The first section (section A) presents the experimental results and the corresponding microstructure model. A schematic representation of the research framework is provided in Figure. 1.1. The main objectives of this work are outlined in Chapter 2. Chapter 3 reviews the state-of-the-art and relevant literature that supports the experiments and models described in this thesis. Chapter 4 introduces the detailed material and experimental procedures. The subgrain size models that have already been published and the subsequent comprehensive dislocation-based model framework are presented in Chapter 5. Chapter 6 discusses the experimental and simulation results, with the corresponding analysis. The models for dislocation density and substructure evolution are simulated individually, compared with experimental results, and their main mechanisms are discussed. The second section (section B) comprises three scientific papers that constitute a significant portion of this

work.

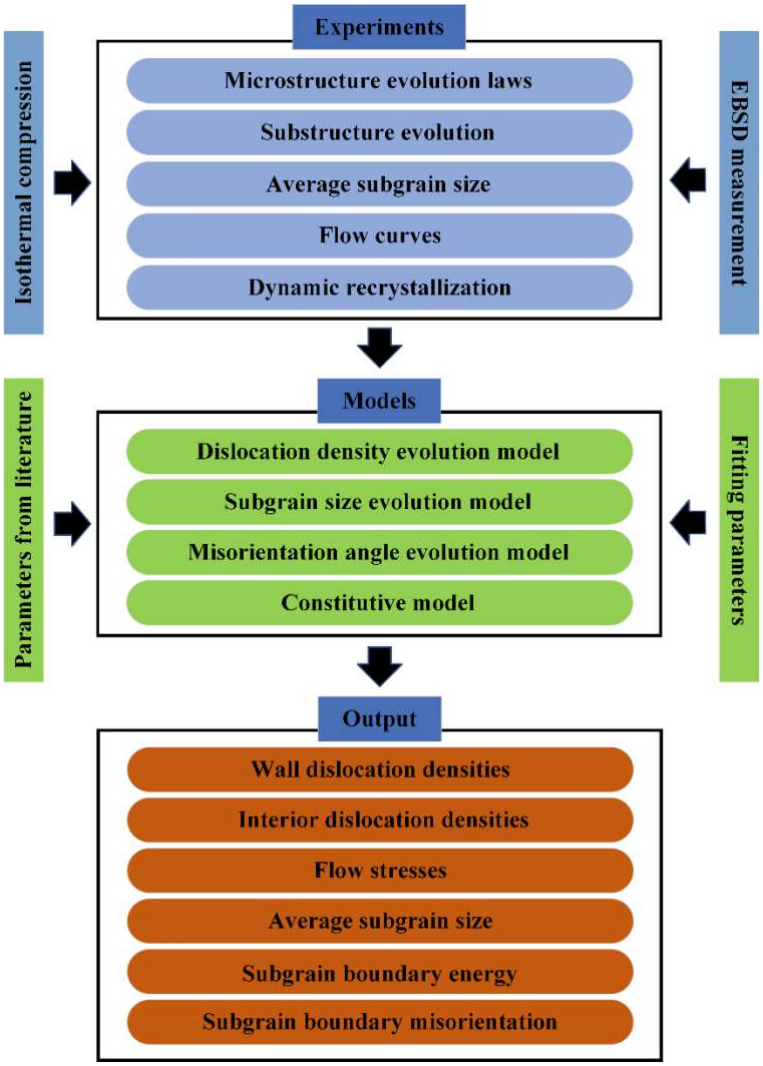

Fig. 1.1. Schematic representation of the research framework of this thesis.

2. Objectives

The main objective of this work is to characterize and model the evolution of microstructure and substructure in Al alloys, including establishing the relationship between processing parameters, microstructural and substructural changes, and experimental results throughout the high-temperature deformation process.

The specific objectives are:

- Investigate the microstructural features and their evolution during hot compression and establish their relationships with the measured flow stress.
- Investigate the potential DRX evolution and quantify its dependence on various deformation parameters.
- Investigate the evolution of substructure and measure the average subgrain size under different conditions.
- Describe and model the evolution of low-angle subgrain sizes.
- Establish the relationships between the primary microstructural evolution mechanisms observed in Al alloys and various deformation conditions.
- Develop a dislocation-based model that incorporates substructure evolution and flow stress.

The innovative technological aspects of this study include:

- The experimental results provide an indication that recrystallization can proceed under continued strain during high-temperature compression.
- The implementation of an automatic identification approach using EBSD data to accurately identify subgrains, and the corresponding average subgrain size is measured.
- The application of both an empirical model and an advanced substructure-based model to reproduce the average subgrain size incorporates several internal state variables.
- The development of a dislocation-based model for substructure evolution and flow stress.

3. State of the art

3.1 Aluminum and aluminum alloys

Aluminum is denoted by the chemical symbol Al and its atomic number is 13 [18]. Al is the most abundant metallic element in the Earth's crust and the third most abundant of all elements (after oxygen and silicon) [19].

Al exhibits a melting point of 660 °C and a boiling point of 2327 °C [18]. The density of pure Al at room temperature is 2.7 $g.cm^{-3}$, which is almost 1/3 of that of steel and much lower than that of other common metals [18]. Al alloys are widely used in aerospace, construction, automotive and other industries due to their light weight and low cost.

3.2 Microstructural evolution in hot forming of Al alloy

Microstructural evolution has a significant impact on the macroscopic properties of materials. During thermomechanical forming, many deformation behaviors are observed depending on the different metallurgical mechanisms [1-9]. The strain hardening, recovery and recrystallization mechanisms associated with microstructural evolution are as follows.

(1) Strain hardening

Strain hardening or work hardening (WH) is a standard metallurgical process associated with dislocation evolution during thermomechanical forming [1]. As deformation proceeds, dislocations accumulate within the metal crystal structure through pinning or entanglement interactions. These dislocations form at locations such as grain boundaries, free surfaces and grain-internal sources, such as, Frank-Read sources [7-9].

(2) Recovery

Recovery is a process during which defects (dislocations) are removed or rearranged to reduce the internal energy of the material [7]. Two main mechanisms occur during recovery: (i) dislocation annihilation and (ii) dislocation rearrangement into low-angle cell structures or subgrain boundaries [7-9]. Sliding, creep, and cross-slip motions of dislocations promote microstructural recovery.

Figure 3.1 shows a schematic diagram of a crystal containing edge dislocations. When two dislocations with antiparallel Burgers vectors (e.g., A and B) exist on the same slip plane and approach each other within a critical distance d_{crit}, annihilation can occur. Similarly,

configurations of screw dislocations can be annihilated by cross-slip [1].

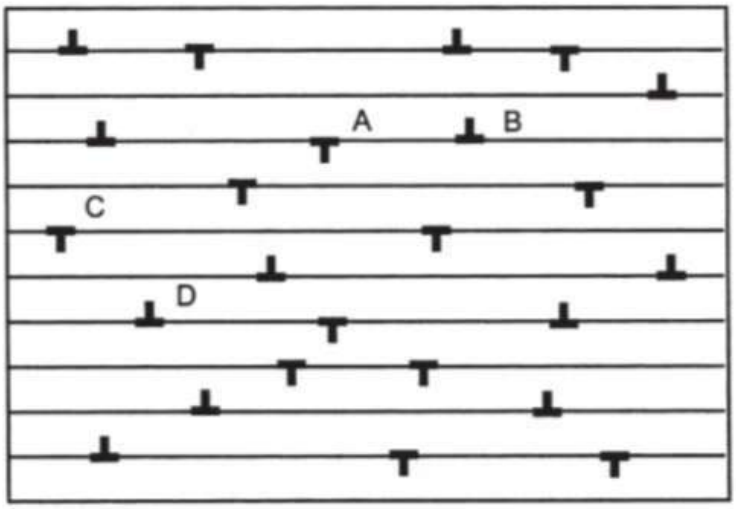

Fig. 3.1. Schematic of a crystal containing edge dislocations. [1]

Another primary recovery process produces a dislocation substructure hierarchy with dislocation accumulation and rearrangement [8]. Figure 3.2 shows a schematic diagram of dislocation wall formation during recovery. In the initial stage of deformation, as strain continues, a high density of dislocations is introduced into the cell substructure. This rearrangement causes the parent grains to be subdivided into smaller and more severely dislocated fragments [7-9].

Currently, low-angle boundaries and substructure evolution can be measured experimentally using electron backscatter diffraction (EBSD) and transmission electron microscopy (TEM), which allows for investigating its effects on material properties. The microstructure information such as microscopic subgrain/grain boundaries, dislocation movement, misorientation under complex conditions lays the foundation for the mathematical models and simulations.

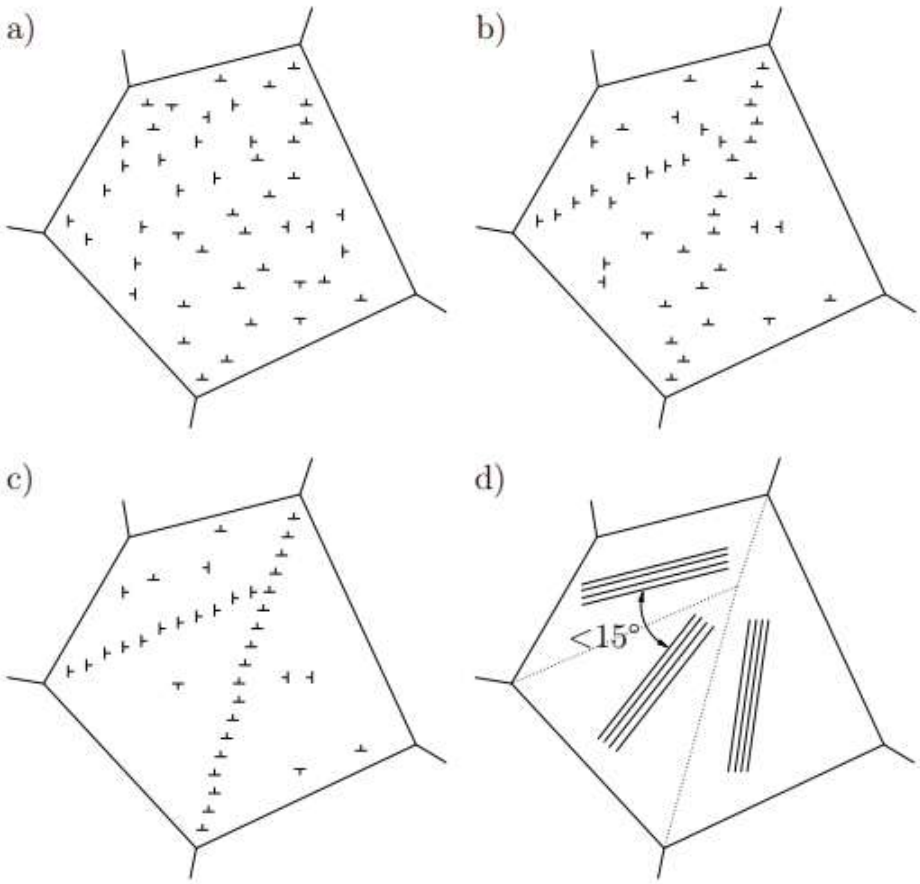

Fig. 3.2. Formation of dislocation walls during recovery. (a) randomly distributed dislocations, (b)-(c) the process of dislocation rearrangement to form subgrain walls, and (d) the misorientation of evolving cells does not exceed 15°. [20]

(3) Dynamic recrystallization

In addition, advancements in experimental techniques have increasingly observed the occurrence of DRX phenomena during the thermal forming processes, such as the hot deformation process and severe plastic deformation (SPD) [7-9]. The DRX mechanisms in Al alloys include discontinuous dynamic recrystallization (DDRX) [21-23], CDRX [24-27] and geometric dynamic recrystallization (GDRX) [28-29].

In recent years, CDRX has been observed to be the main DRX mechanism during deformation of Al alloys [7-17]. This phenomenon has been studied in different Al alloys, including Al-Li-Mg-Sc [10], AA7075 alloy [30], Al-Mg-Si [31], and 7055 alloy [32], etc. CDRX is a non-nucleation process characterized by the continuous rotation of low-angle subgrains. The misorientation gradually increases, absorbing mobile dislocations until they transform into HAGB [9,17].

3.3 Modeling microstructure evolution in Al alloy

Microstructural features consistent with these CDRX mechanisms in Al alloys have been experimentally observed in the literature [7-17]. Figure 3.3 shows a detailed view of the EBSD map to better understand the development of the microstructure and substructure. The formation of cell boundaries is characterized by a high density of dislocations, mainly composed of geometrically necessary dislocations (GNDs), which subdivide the parent grain into subgrains and maintain the deformation gradient within the grain as well as the rotation of the subgrains [7]. As deformation proceeds, the misorientation angles of the subgrain boundaries increase until they transform into HAGBs [7-9]. These microstructural features will be integrated into a dislocation-based model of Al alloys to simulate the microstructural evolution under different deformation conditions.

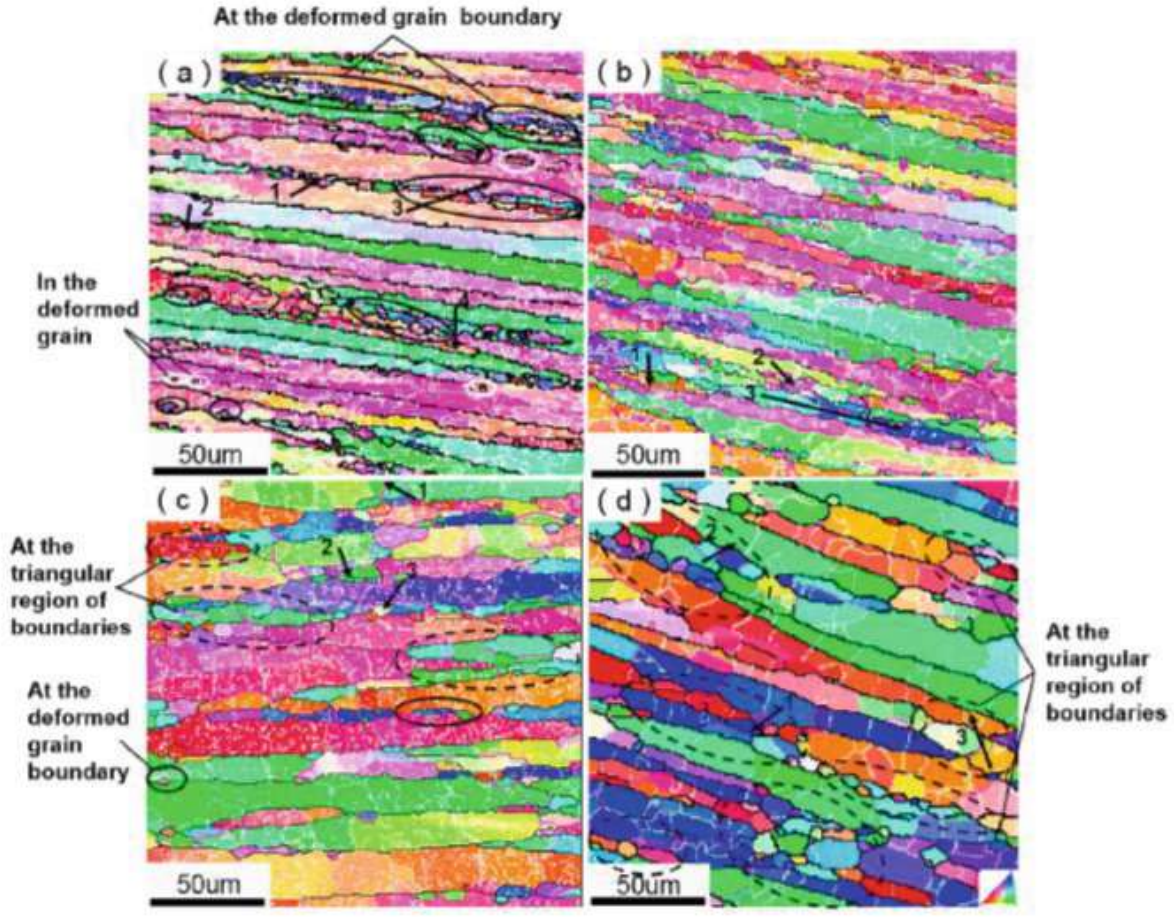

Fig. 3.3. EBSD images of 2195 Al alloy after hot compression at different temperatures, a strain rate of 0.01 s^{-1}, and a deformation degree of 60%: (a) 300 ℃, (b) 420 ℃, (c) 480 ℃, and (d) 520 ℃. [13]

Material models for microstructural evolution based on DDRX are well-established in the

literature [33-36], while models that capture physically meaningful substructural evolution and related CDRX processes are less prevalent. Gourdet and Montheillet [37] proposed a physically based CDRX model, the GM model, which incorporates the average dislocation density, average subgrain/grain size, flow stress, and subgrain boundary misorientation. The main principle of the GM model based on dislocation distribution is shown in Figure 3.4.

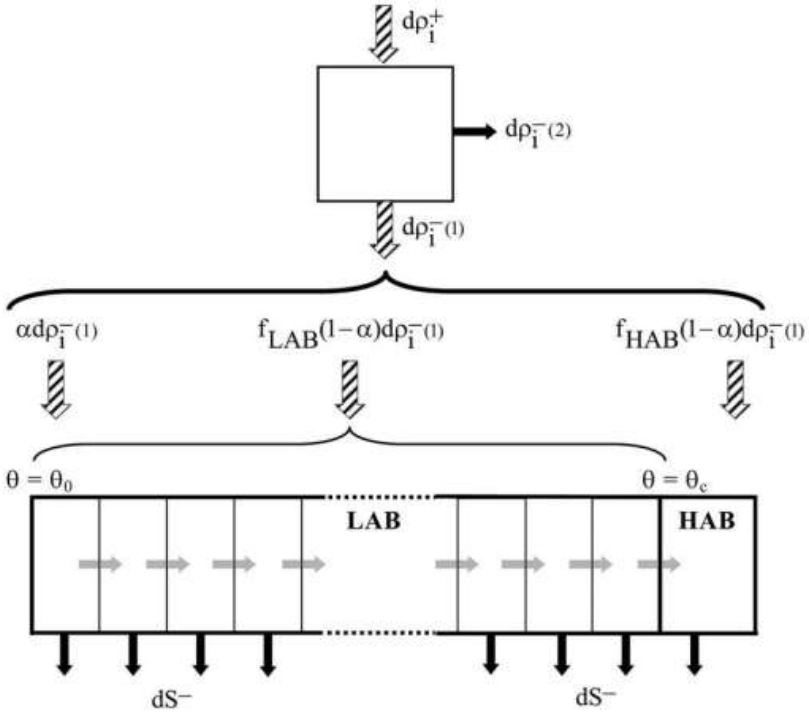

Fig. 3.4. A diagram illustrates the distribution of dislocations produced by strain hardening among the various microstructural elements in the GM model. [37]

Sun et al. [38] and Chen et al. [39] modified the GM model with more internal-state variables, enabling the calculation of low-angle subgrain size and DRX grain size by introducing subgrain boundary area and recrystallized grain boundary area, and different subgrain rotation models are also developed. In addition, Buzolin et al. [40], Li et al. [41] and Chen et al. [42] recently established physical microstructure models based on the GM model.

4. Material and experimental procedures

4.1 Material

The material investigated in this study is AA1050 aluminum alloy billets supplied by Neuman Aluminum Austria GmbH. The chemical composition is summarized in Table 4.1.

Table 4.1. Chemical composition of AA1050 aluminum alloy (wt%)

Si	Fe	Cu	Mn	Mg	Cr	Zn	Ti	Al
0.08	0.26	<0.01	<0.01	<0.01	<0.01	<0.01	<0.01	99.63

4.2 Hot compression tests

The hot compression procedures described in this study for analyzing the flow curve and microstructure have been previously published in [17], and the compression procedures for examining the substructure are detailed in [43]. Single-pass isothermal compression is performed on a high-speed quenching and deformation dilatometer DIL 805 A/D from Bähr. The compression parameters are as follows: a temperature range from 300 to 500 °C [8, 44], a strain rate range from 0.001 to 0.8 s^{-1}, and a deformation strain of 0.9. The melting temperature T_m of the alloy is 625 °C using MatCalc software version 6.04 [45] with the thermodynamic database mc_al.tdb (version 2.036) available on the MatCalc web site. For a detailed history of isothermal compression, see publication [17].

Different true strains are used to study the substructure evolution under high-temperature compression. In single-pass isothermal compression, four true strains (0.1, 0.3, 0.6, and 0.9) are applied at a temperature range of 300 °C to 500 °C and two strain rates of 0.01 s^{-1} and 0.1 s^{-1}.

4.3 Microstructure investigation

The micro/substructure evolution of this Al alloy is characterized by electron backscatter diffraction (EBSD). The measurements are performed using a Zeiss Sigma 500VP high-resolution scanning electron microscope with an EDAX detector. The detailed EBSD measurement procedures are reported in [17] and [43].

The conventional method for measuring subgrain size involves fitting an ellipse to each subgrain using the ImageJ software, where the size is calculated as the ratio of the major axis to the minor axis. However, accurately identifying subgrains is challenging, and manual measurements can result in substantial errors. Therefore, this study employs an automatic

identification approach using EBSD data. The procedures for measuring the subgrain size are shown in Figure. 4.1.

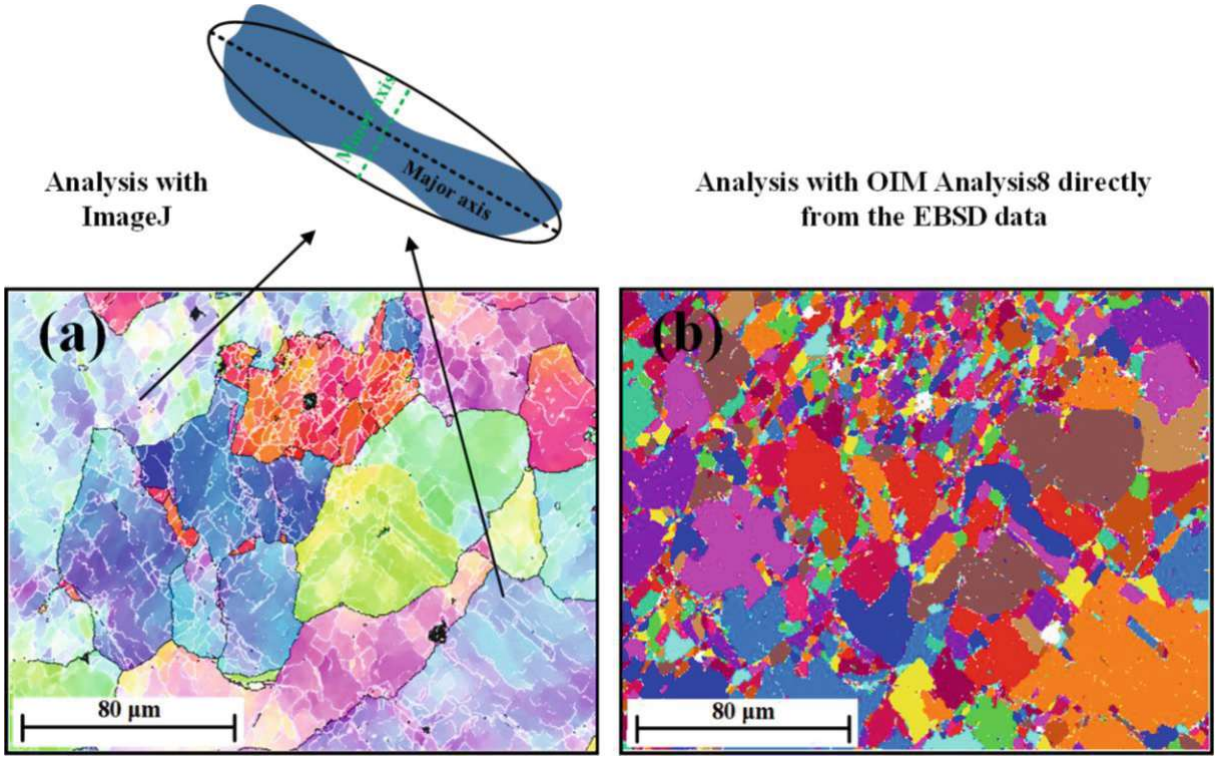

Fig. 4.1. Procedures for measuring the subgrain size: (a) analysis with ImageJ and (b) analysis with OIM Analysis8 directly from EBSD data.

The data processing of EBSD results is completed using EDAX OIM Analysis8 software. The post-processing procedures are employed to distinguish most of the subgrains directly from the EBSD data, including a "clean up" algorithm, setting up a confidence index, excluding errors or unresolved regions, etc.

5. Modeling of micro/substructure evolution

The developed hot deformation model framework comprises four key components: dislocation density evolution, subgrain size (diameter) evolution, subgrain misorientation angle, and flow stress. The main microstructural evolution mechanisms observed in Al alloys have been extensively summarized in the literature [1, 7-17, 37-42]. Figure. 5 .1 Illustrates the microstructure evolution laws during high-temperature compression in Al alloy. The modeling of micro/substructure evolution laws can be strongly influenced by the deformation conditions, and the essential evolution equations are presented in this chapter.

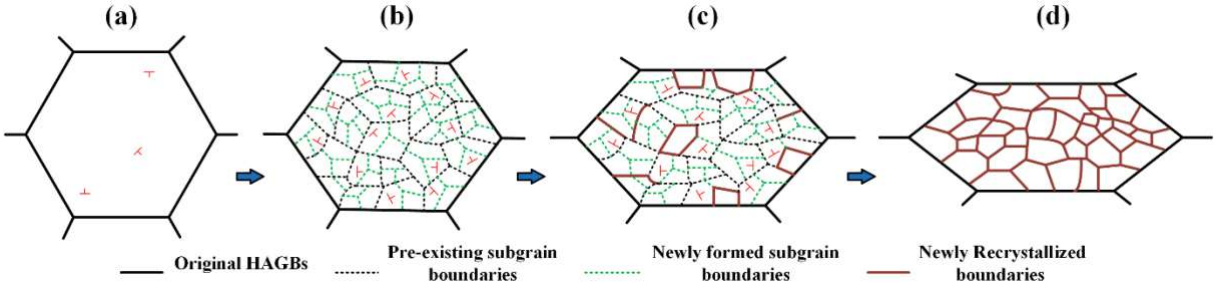

Evolution / Variables	Step (a)	Step (b)	Step (c)	Step (d)
Excess Dislocation density ρ	0	↑	↓	Constant
δ_{sub}	None	↓	δ_{DRX}	Constant
X_{DRX}	0	0	↑	=100%
Subgrain misorientation θ	0°	>2° ↑	Some>15° ↑	Constant
D	D0	D0	↓	δ_{DRX}

Fig. 5.1. Illustration of Al alloy's microstructure evolution laws during high-temperature compression.

5.1 Subgrain size evolution model

In the present work, two subgrain size (diameter) evolution models are applied and verified based on experimental data. The empirical model describes the subgrain evolution from an initial subgrain size δ_0 decreasing to a saturated subgrain size δ_s, as suggested by Hallberg et al. [46].

$$\begin{cases} \delta_w = \delta_0 - (\delta_0 - \delta_s)\left[1 - \exp\left(-\alpha_1(\varepsilon_d - \varepsilon_c)^{\beta_1}\right)\right], & \varepsilon_d < \varepsilon_s \\ \delta_w = \delta_s, & \varepsilon_d > \varepsilon_s \end{cases}, \tag{5.1}$$

The average subgrain size δ_w is mainly determined by the initial subgrain size δ_0, the saturated subgrain size δ_s, the strain during deformation ε_d, the critical strain up to which subgrains can be distinguished ε_c, and the material constants α_1 and β_1. The saturated subgrain size δ_s can be formulated as [47]

$$\delta_s = [\alpha_2 + \beta_2 \ln\left(\dot{\varepsilon}\exp(\tfrac{Q}{RT})\right)]^{-1}, \tag{5.2}$$

where α_2 and β_2 are material constants, $\dot{\varepsilon}$ is the strain rate, Q is the deformation activation energy, R is the gas constant, and T is the deformation temperature.

Another model for subgrain size evolution is the substructure-based model based on the work of Nes [48]. This model simulates the subgrain evolution process during deformation, such as subgrain refinement and coarsening, and is expressed as [48-49]

$$d\delta_w/dt = -f_r \frac{\sqrt{3}\dot{\varepsilon}b^{1/2}}{\bar{\theta}_s^{\,3/2}\bar{\delta}_s^{\,2}}\delta_w^{\,v_1} + f_c v_D b^2\sqrt{\rho_t}\left[\exp-\left(\frac{U_s - PV_a}{k_B T}\right)\right], \tag{5.3}$$

The substructure-based model is mainly determined by the average subgrain boundary misorientation in the steady-state stage $\bar{\theta}_s$, the average subgrain size of the steady-state stage $\bar{\delta}_s$, the Burger's vector b, the Debye frequency v_D, the Boltzmann constant k_B, the total dislocation density ρ_t, the driving force on the subgrain boundary P, the average activation volume of subgrain boundaries V_a, the activation energy for self-diffusion in Al U_s, the material coefficient that controls the subgrain refinement rate v_1, and the material coefficients f_r and f_c.

The driving force for subgrain boundary movement can be expressed in terms of the subgrain boundary energy γ and the average subgrain size, as described in the literature [48] and [50].

$$P = \frac{4\gamma}{\delta_w}, \text{ with } \gamma = \gamma_m \frac{\theta_w}{\theta_m}(1 - \ln(\frac{\theta_w}{\theta_m})), \tag{5.4}$$

where γ_m is the boundary energy of HAGBs, and θ_m is the critical misorientation angle, is taken as 15°.

The average activation volume of the subgrain boundary can be expressed as [48]

$$V_a = \frac{b^3}{\theta_w}, \tag{5.5}$$

where θ_w is the average subgrain boundary misorientation angle. The detailed model parameters and simulation processes are reported in [43].

5.2 Dislocation density evolution model

The total dislocation density (ρ_t) can be divided into two populations as suggested by the GM model [37] and the 3IVM model [51], as interior dislocation densities (ρ_i) and wall dislocation densities (ρ_w). Therefore, the total dislocation density (ρ_t) can be calculated by the linear mixture rule, and is expressed as

$$\rho_t = f_i\rho_i + f_w\rho_w, \tag{5.6}$$

The material coefficient f_i considers the fraction of interior dislocation densities, and the

material coefficient f_w relates to the fraction of wall dislocation densities, with $f_i + f_w = 1$.

The interior dislocation density model incorporates several vital mechanisms: work hardening (WH), DRV, static recovery (SRV), and migration of HAGBs. The model used in the present work is based on Sherstnev, Lang, and Kozeschnik [52].

$$d\rho_i/dt = \frac{M\sqrt{\rho_i}}{Ab}\dot{\varepsilon} - 2BM\rho_i\frac{d_{crit}}{b}\dot{\varepsilon} - 2CD_d\frac{Gb^3}{k_BT}\left({\rho_i}^2 - \rho_{eq}^2\right) - 2f_H v_H \rho_i \frac{1}{\delta_w}, \qquad (5.7)$$

The interior dislocation density is mainly determined by the Taylor factor M, the shear modulus G, the material-dependent coefficients A, B, and C, the critical distance of dislocation annihilation d_{crit}, the diffusion coefficient along dislocation pipes D_d, the equilibrium dislocation density ρ_{eq}, the average size of low-angle walls/subgrains δ_w, the fraction of HAGBs f_H, and the migration rate of HAGBs v_H.

The wall dislocation density model is represented as the total length of wall dislocation lines per unit volume, and the corresponding substructure variables are directly introduced. The formula is presented as [53]

$$\rho_w = \frac{\sum_1^i L_{wi}}{\sum_1^i V_{wi}} = f_s\frac{\theta_{wi}}{2b}r_i, \qquad (5.8)$$

where L_{wi} is the total length of wall dislocation lines of the i-th subgrain wall, V_{wi} is the total volume of the i-th subgrain wall, θ_{wi} is the average misorientation angle of the i-th subgrain walls, r_i is the ratio of subgrain surface to subgrain volume, and f_s is a materials coefficients, is taken as 1/8 in present work.

Subsequently, the substructure variables, including average subgrain size (diameter) δ_w and average misorientation angle of subgrain walls (cells) θ_w are introduced. The Equation. (5.8) can be rewritten as

$$\rho_w = f_s\frac{\theta_w}{2b}\pi{\delta_w}^2/(\frac{4}{3}\pi(\frac{\delta_w}{2})^3), \qquad (5.9)$$

where $\bar{V}_w$ is the average volume of subgrain walls.

5.3 Misorientation angle evolution model

Following the research of Gourdet and Montheillet [37], the evolution of dislocation density during the DRV process can be divided into two parts: (i) the annihilation of recovered dislocation density and (ii) the contribution to the formation of new low-angle subgrain boundaries.

Subsequently, an extended model considers the evolution of dislocation density, average subgrain size, and subgrain boundary energy is expressed as [37]:

$$d\theta_w/dt = f_\theta \frac{b\dot{\varepsilon}\delta_w}{2n}\frac{(1-\alpha_s)}{\alpha_s}(2BM\rho_i\frac{d_{crit}}{b}\dot{\varepsilon} - 2CD_d\frac{Gb^3}{k_bT}(\rho_i{}^2 - \rho_{eq}^2))\gamma^{c_1}, \quad (5.10)$$

The subgrain misorientation angle is mainly determined by the number of dislocations pairs within the boundary n, as the value of 3 suggested by Gourdet and Montheillet [37], the fraction of the recovered dislocation density is consumed to annihilate α_s, the material constant c_1, and the material coefficient related to the saturated misorientation angle f_θ.

Current research shows that the average misorientation of subgrain boundaries in Al alloys reaches a steady-state value of about 4° to 8° during deformation, as $d\theta_w/dt = 0$. The material coefficient f_θ is described with the saturated misorientation angle θ_{sat}, as Equation. (5.11).

$$f_\theta = c_2\left(1 - \frac{\theta_w}{\theta_{sat}}\right), \quad (5.11)$$

where c_2 is a material constant, and θ_{sat} is the saturated misorientation angle occurring with continuing deformation.

5.4 Constitutive model

The contributions of interior dislocation density ρ_i and wall dislocation density ρ_w to the flow stress are described using the Taylor equation with [54]. The constitutive model can be expressed as

$$\sigma = \sigma_0 + \alpha MGb(f_i\sqrt{\rho_i} + f_w\sqrt{\rho_w}), \quad (5.12)$$

where σ_0 is the basic yield strength, and α is the strengthening coefficient related to the dislocation strengthening.

6. Results and discussion

6.1 Methodology

The material and experimental procedures are described in Section 4. Several compressions and EBSD experiments describe results such as flow curves and microstructural information. Microstructural data are used to study and validate the evolution of the micro/substructure.

6.2 Microstructure and DRX

The microstructural evolution and the DRX mechanisms of the AA1050 aluminum alloy are characterized by EBSD measurements, as shown in Figure. 6.1. After deformation, a large number of low-angle subgrain boundaries can be identified within the elongated parent grains. In high SFE alloys, dislocation rearrangement and annihilation occur easily through DRV, forming subgrain boundaries within the parent grains [7-9]. In addition, some newly formed fine grains are observed within parent grains or near/on the parent grain boundaries, which are recrystallized grains generated by the transformation of low-angle subgrain boundaries into HAGBs.

According to the published research [17], different deformation conditions significantly influence the microstructure, DRX fraction, and misorientation. The effect of the temperatures on the microstructure is shown in Figure. 6.1. Increased temperature promotes the growth of subgrain and grain sizes due to enhanced boundary mobility at elevated temperatures [7-9]. Furthermore, fine subgrains and recrystallized grains form at low strain rates with the elongation of deformation time [17]. The observed microstructure evolution is consistent with the conclusions reported by Raabe [7], Sakai et al. [8], and Huang and Logé [9].

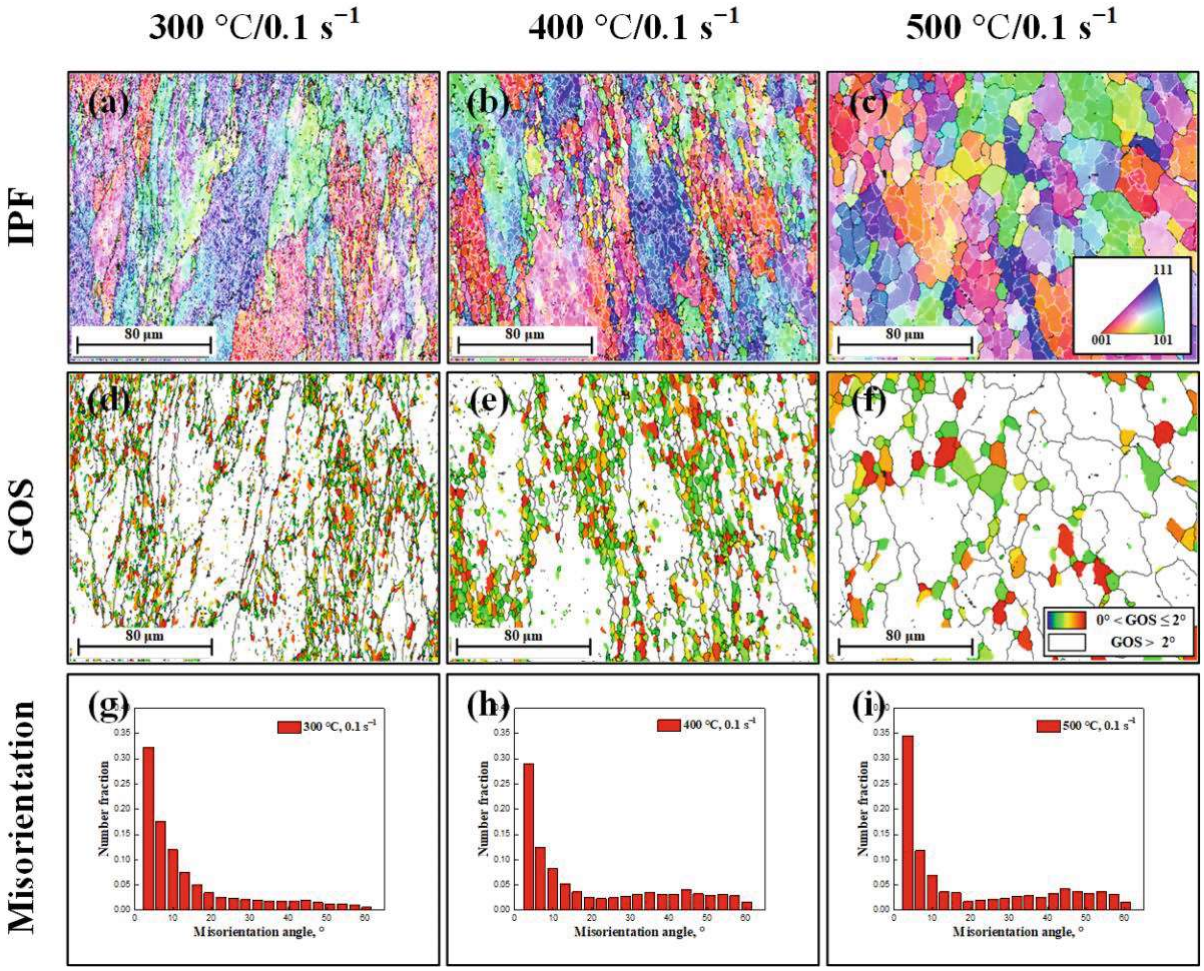

Fig. 6.1. EBSD images of AA1050 aluminum alloy deformed to a strain of 0.9 with a strain rate of 0.1 s^{-1}: (a)-(c) IPF maps of the specimens deformed at 300, 400, and 500 °C, (d)-(f) GOS maps with high angle grain boundaries, and (g)-(i) distribution histograms of misorientation angle. [17]

The microstructure experiment results show the generation of low-angle subgrain boundaries and their subsequent transformation into HAGBs in pure Al alloy. A well-defined substructure and subgrain rotation indicate that DRX can proceed with continued strain under hot deformation conditions.

6.3 Substructure evolution

The microstructure/substructure maps of the experiments after different strain levels are shown in Figure 6.2. At the beginning of deformation, irregular initial subgrain boundaries are observed within the parent grains, which is different from the behavior of the initial subgrains nucleated at the parent grain boundaries during the DDRX process. These observations indicate that the formation of subgrain boundaries is a non-nucleation process, which is consistent with the conclusions reported in the literature [7-17]. As the deformation progresses, the number of

low-angle subgrain boundaries begins to increase, accompanied by a significant decrease in the subgrain size. The corresponding unique grain color map describes the evolution and size of the subgrain boundaries. In addition, more newly formed equiaxed subgrains and the increase in boundary misorientation angles suggest the progression of subgrain rotation.

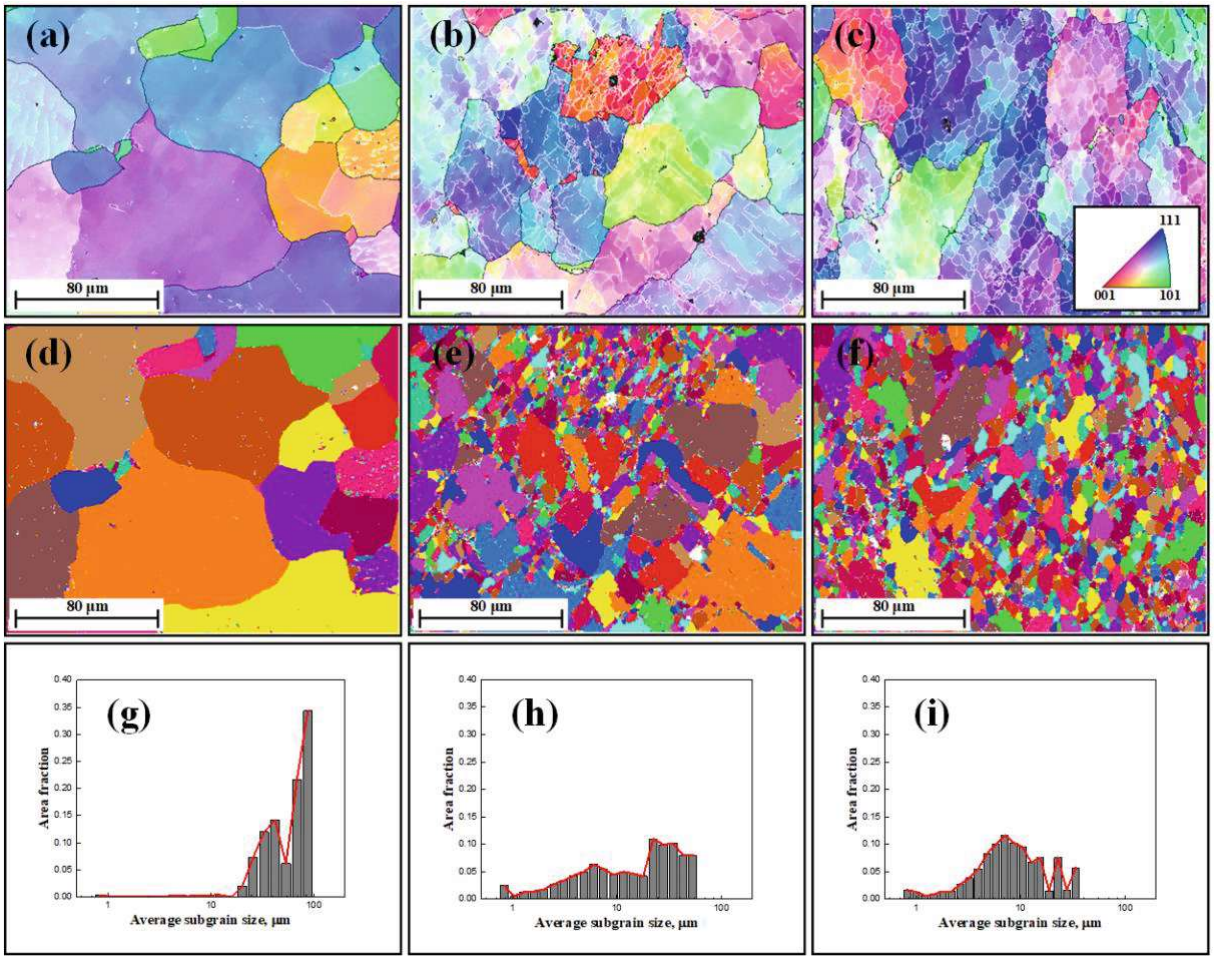

Fig. 6.2. EBSD images of 1050 Al alloy deformed to a different strain at a temperature of 300 °C and a strain rate of 0.1 s^{-1}: (a)-(c) inverse pole figure (IPF) maps of the specimens with strain 0.1, 0.3 and 0.6, (d)-(f) corresponding unique grain color maps, and (g)-(i) subgrain size distribution maps. [43]

According to the published study [43,47-48], the coexistence of subgrain refinement and thermal coarsening is influenced by variations in deformation conditions. Experimental results on the relevant substructure and measurements of average grain size are detailed in the published paper [43].

6.4 A dislocation-based model considering substructure evolution and flow stress

The input parameters employed in these models for all deformation conditions are detailed in Ref. [43]. The dislocation density evolution parameters can be found in the literature suggested by Sherstnev, Lang, and Kozeschnik [52] and Gourdet and Montheillet [37]. The saturated misorientation angle with continuing deformation θ_{sat} is taken as 5° in the present work. The material constants c_1 and c_2 are set to 0.75 and 25, respectively. The strengthening coefficient α is taken as 0.2. The list of input parameters for AA1050 Al alloy is shown in Table 6.1.

Table 6.1. List of input parameters for models for AA1050 Al alloy

Symbol	Name	Unit	Value	Ref.
Q_{vac}	Activation energy for vacancy formation	eV	0.67	[55]
Q_d	Activation energy for pipe diffusion	J.mol^{-1}	$83.2 \cdot 10^3$	[56]
D_{d0}	Pre-exponential factor for pipe diffusion	m^2.s^{-1}	$1.5 \cdot 10^{-6}$	[56]
A	A parameter	-	$1.8\exp(0.0066T)$	This work
B	B parameter	-	3	This work
C	C parameter	-	$1 \cdot 10^{-3}$	This work
σ_0	Basic yield strength	MPa	$\sigma_0 = 1.1[\dot{\varepsilon}\exp(Q/RT)]^{0.1}$	This work
f_i	Fraction of interior dislocation densities	-	0.95	This work
f_w	Fraction of wall dislocation densities	-	0.05	This work

This section compares the simulated results from the dislocation-based model against the experimental flow stress. The simulations are conducted using MATLAB software version R2016b employing the list of input parameters.

6.4.1 Evolution of dislocation density

Figure. 6.3 shows the simulation results of two populations of dislocation densities (in cell walls and cell interiors) and the total dislocation density. At the beginning of deformation, the interior dislocation density increases rapidly with increasing strain. The generation and

accumulation of dislocations caused by WH show such evolutionary characteristics, which is consistent with the expected evolution of the flow stress, subgrain size, and misorientation in experimental studies. As deformation progresses, the interior dislocation density reaches a plateau state, reflecting a balance between the generation and annihilation of interior dislocations, in agreement with the studies from Prasad et al. [57].

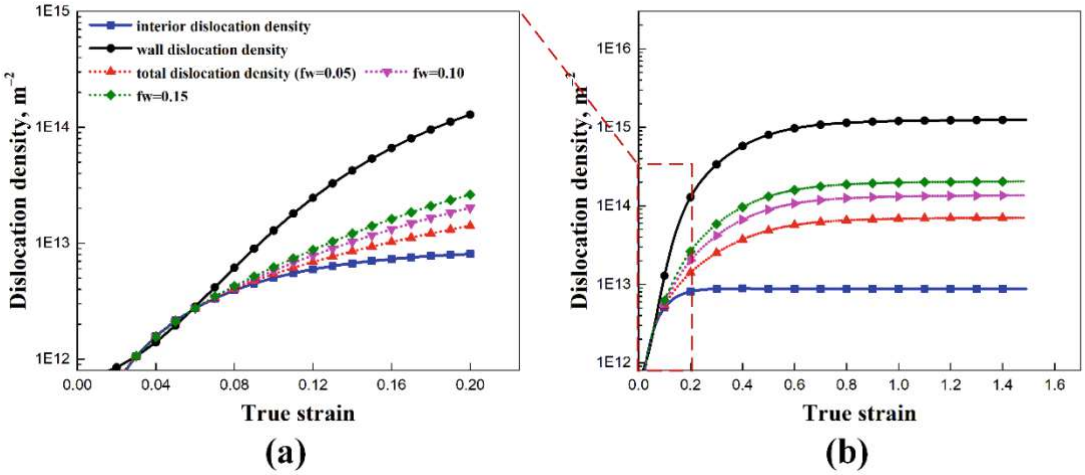

Fig. 6.3. Simulated total dislocation density (ρ_t), dislocation densities of cell walls (ρ_w) and cell interiors (ρ_i) at 400 °C/0.1 s^{-1} of (a) strain 0.2 (the initial stage), and (b) strain 1.5.

As illustrated in Fig. 6.3(a), wall dislocations also increase rapidly in the early stages of the hot deformation, closely associated with the formation of subgrains and the evolution of misorientation angles. Evidence supports the generation of low-angle subgrain boundaries due to the accumulation of interior dislocations, which are then transformed into wall dislocations. The simulation results are consistent with the 3IVM model [51,58], wherein the density of wall dislocations is calculated based on the evolution of dipole dislocations ρ_{dip}, as $d\rho_w/dt = (1/f_w)(d\rho_{dip}/dt)$.

The simulated total dislocation density for varying material coefficients f_w is presented in Fig. 6.3. As the number of dislocations participating in the formation of the subgrain wall increases, the total dislocation density will also increase. The increase in wall dislocation density and total dislocation density will also be reflected in an increase in flow stress [54], as indicated by the Equation. (5.12). The evolution mechanism of total dislocation density closely follows the behavior of both interior and wall dislocations. The simulated results of interior dislocation density and wall dislocation density under other deformation conditions are shown in Fig. 6.4 and Fig. 6.5.

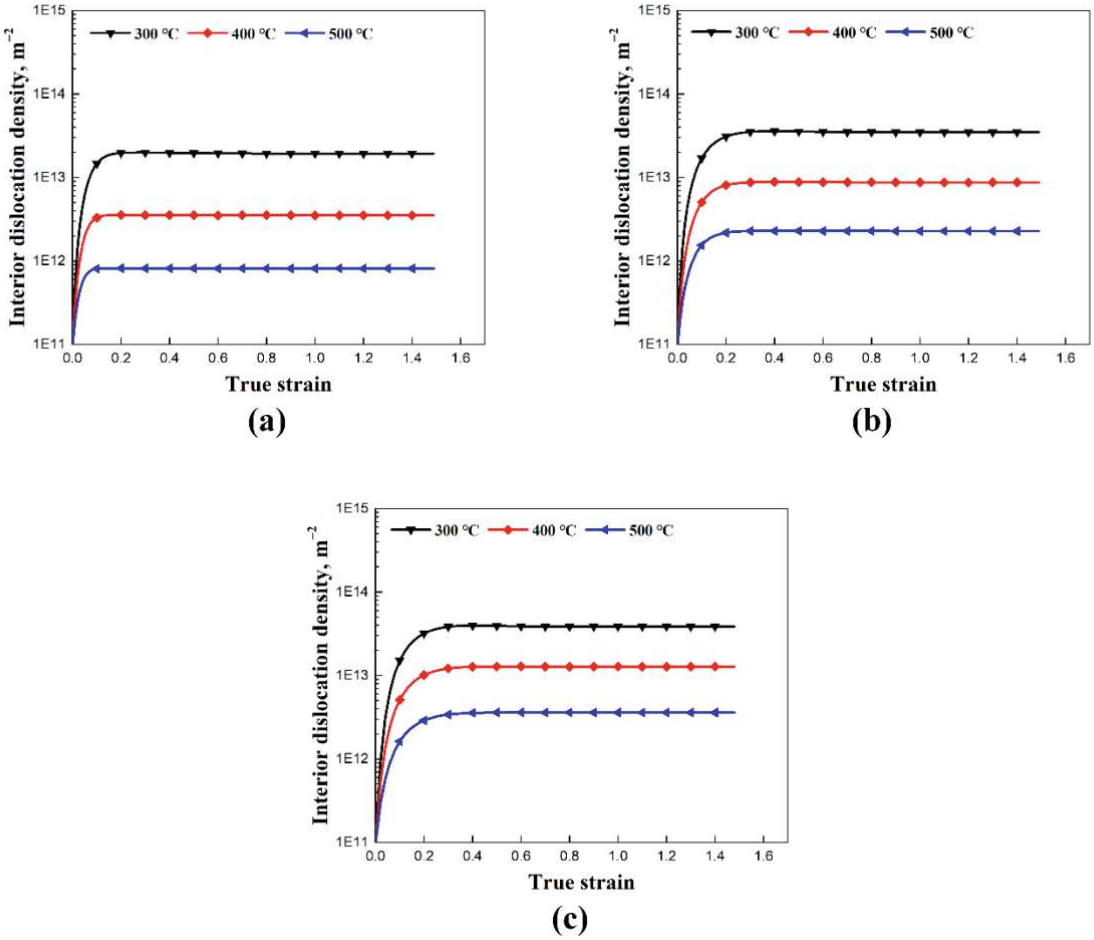

Fig. 6.4. Simulated interior dislocation density (ρ_i) under different deformation conditions: (a) 0.01 s^{-1}, (b) 0.1 s^{-1}, and (c) 0.8 s^{-1}.

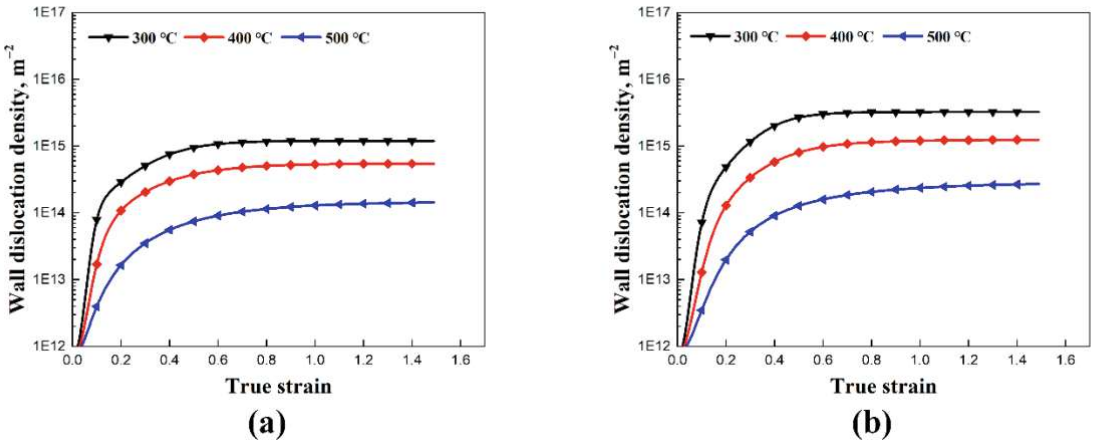

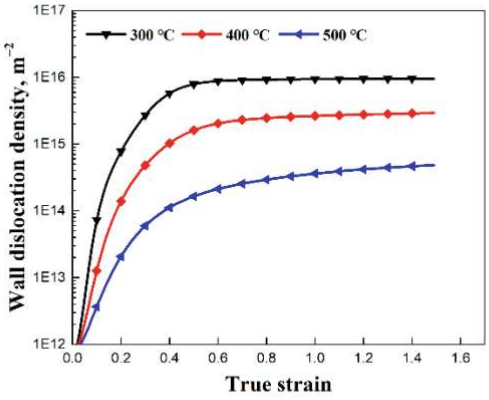

Fig. 6.5. Simulated wall dislocation density (ρ_w) under different deformation conditions: (a) 0.01 s^{-1}, (b) 0.1 s^{-1}, and (c) 0.8 s^{-1}.

6.4.2 Flow curve

Figure. 6.6 shows the experimental and simulated values of the flow stress at different temperatures and strain rates. In the early stage of deformation, the multiplication and tangling of dislocations by WH result in a rapid increase in flow stress. This is consistent with the phenomenon in Section 6.3, which states that subgrain boundaries are generated due to dislocation accumulation, resulting in a rapid decrease in the average subgrain size [7-9]. As deformation progresses, softening (recovery and DRX) eventually leads to a balanced deformation state, consistent with conclusions reported in the literature [37-42].

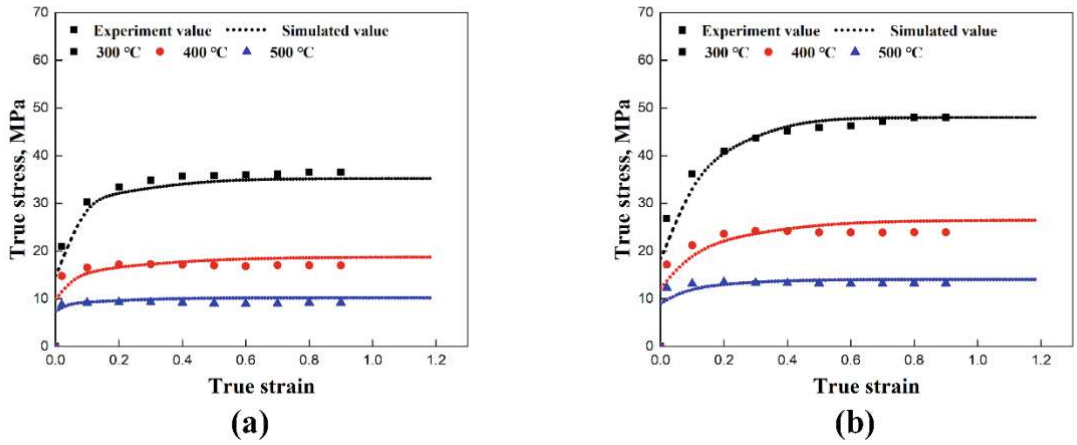

Fig. 6.6. The comparison between the experimental and simulated flow stress values under different deformation conditions (AA1050 Al alloy): (a) 0.01 s^{-1}, and (b) 0.1 s^{-1}.

Figure. 6.7 shows the corresponding error analysis under different experimental conditions. The correlation coefficient (R) and root mean square error ($RMSE$) [59] are calculated according

to Equation (6.1) and (6.2), respectively. The values of R and $RMSE$ are 0.98 and 2.0 MPa, respectively, which indicate good agreement between the experiment and the model.

$$R = \frac{\sum_{i=1}^{N}(\delta_{ei}-\bar{\delta}_{e})(\delta_{ci}-\bar{\delta}_{c})}{\sqrt{\sum_{i=1}^{N}(\delta_{ei}-\bar{\delta}_{e})^{2}\sum_{i=1}^{N}(\delta_{ci}-\bar{\delta}_{c})^{2}}}, \tag{6.1}$$

$$RMSE = \sqrt{\frac{1}{N}\sum_{i=1}^{N}(\delta_{ci}-\delta_{ei})^{2}}\cdot 100\%, \tag{6.2}$$

where δ_{ci} and δ_{ei} represent the calculated and experimental flow stress, respectively, $\bar{\delta}_{c}$ and $\bar{\delta}_{e}$ are the average calculated and experimental flow stress, respectively, and N is the total number of data points.

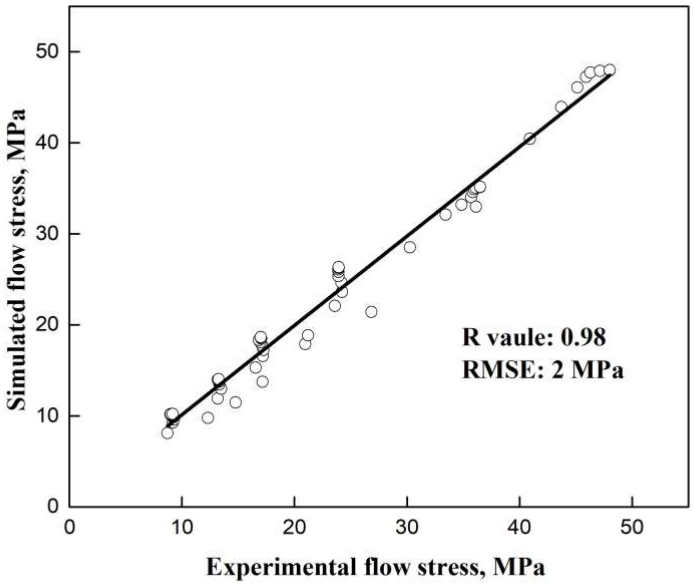

Fig. 6.7. Error analysis for the dislocation-based model

6.4.3 Model application for 5052 Al alloy

The proposed dislocation-based model can quantify both the substructure evolution and flow stress in high-SFE materials. To assess its applicability in various Al alloys, the proposed constitutive model is compared with the experimental data for AA5052 Al alloy reported by Gourdet [60]. Figure 6.8 compares the experimental flow curves and those simulated by the dislocation-based model, demonstrating good agreement between the experimental and simulated flow stress. The input parameters used in the constitutive model for the AA5052 alloy are selected in Table 6.2.

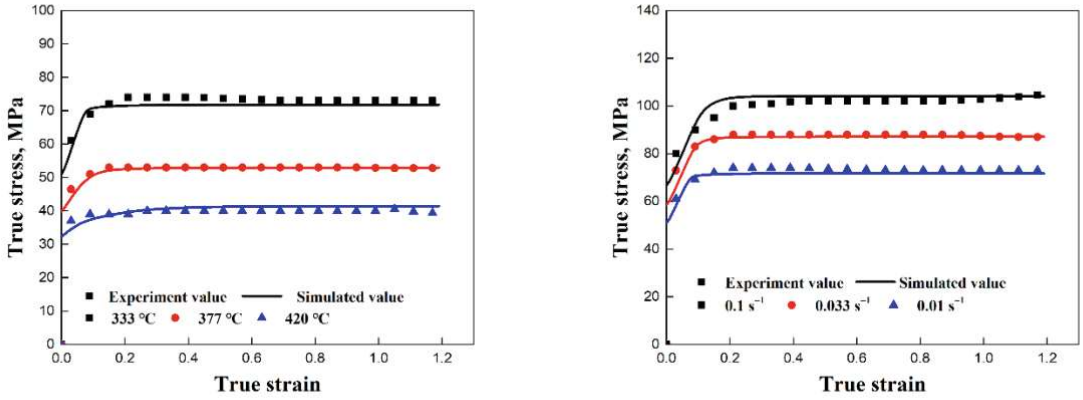

Fig. 6.8. The comparison between the experimental and simulated flow stress values under different deformation conditions (AA5052 Al alloy): (a) 0.01 s^{-1}, and (b) 333 °C.

Table 6.2. List of different input parameters for 5052 Al alloy

Symbol	Name	Unit	Value	Ref.
Q	Activation energy	$kJ.mol^{-1}$	156	[61]
A	A parameter	(-)	$0.005\exp(0.015T)$	This work
B	B parameter	(-)	2	This work
C	C parameter	(-)	1×10^{-3}	This work
σ_0	Basic yield strength	MPa	$2.1[\dot{\varepsilon}\exp(Q/RT)]^{0.12}$	This work
f_i	Fraction of interior dislocation densities	(-)	0.9	This work
f_w	Fraction of wall dislocation densities	(-)	0.1	This work

7. Summary and Conclusions

This study investigates the micro/substructure evolution of AA1050 aluminum alloy under different deformation conditions during high temperature compression. A dislocation-based physical model framework is proposed, which integrates the simultaneous effects of dislocation density, subgrain size, misorientation, subgrain boundary energy, and flow stress, etc. The conclusions are summarized as follows.

The main innovation conclusions of micro/substructure evolution are:

- The formation of a well-defined substructure and the subsequent transformation of LAGBs to HAGBs are of great significance, indicating that continuous dynamic recrystallization can proceed with continued strain under high-temperature compression.
- The dependence of the micro/substructure evolution on factors such as temperature, strain rate, and strain, and their unique role in the simulations are revealed.
- The microstructure evolution laws observed in Al alloys are described, including dislocation density, subgrain size, grain size, misorientation angle of subgrains, DRX fraction, and flow stress.

The main innovation conclusions of the models are:

- An empirical model and another advanced substructure-based model of average subgrain size are established with several internal state variables.
- The process of subgrain evolution is described by introducing saturated average subgrain size, dislocation density, misorientation angle, subgrain boundary energy, etc. The evolution of average subgrain size can be well reproduced across various temperatures and strain rates.
- A dislocation density model is proposed with two populations of interior dislocation densities and wall dislocation densities, which can obtain more realistic simulation results by introducing substructure evolution directly.
- The microstructure evolution law of dislocation and variables is individually simulated and compared, and their mechanisms are also discussed.
- The dislocation-based model framework is successfully applied and validated also in another Al alloy.

References

1. F.J. Humphreys, and M. Hatherly. Recrystallization and Related Annealing Phenomena. 2004, 2nd edn. Elsevier, Oxford.
2. R.D. Doherty, D.A. Hughes, F.J. Humphreys, J.J. Jonas, D. Juul Jensen, M.E. Kassner, T.R. McNelley, H.J. McQueen, and A.D. Rollet. Current issues in recrystallization: a review. Mater. Sci. Eng., A, 1997, vol. 238, pp. 219-274.
3. J.X. Lv, J.H. Zheng, V.A. Yardley, Z.S. Shi, and J.G. Lin. A review of microstructural evolution and modelling of aluminium alloys under hot forming conditions. Metals, 2020, vol. 10, pp. 1516.
4. H. Mirzadeh. Grain refinement of magnesium alloys by dynamic recrystallization (DRX): A review. J. Mater. Res. Technol., 2023, vol. 25, pp. 7050-7077.
5. H.K. Zhang, H. Xiao, X.W. Fang, Q. Zhang, R.E. Logé, and K. Huang. A critical assessment of experimental investigation of dynamic recrystallization of metallic materials. Mater. Des., 2020, vol. 193, pp. 108873.
6. T. Sakai, and J.J. Jonas. Dynamic recrystallization: Mechanical and microstructural considerations. Acta Metall., 1984, vol. 32, pp. 189-209.
7. D. Raabe, 23 - Recovery and Recrystallization: Phenomena, Physics, Models, Simulation, in: D.E. Laughlin, K. Hono (Eds.), Physical Metallurgy, Elsevier, Oxford, 2014, pp. 2291-2397.
8. T. Sakai, A. Belyakov, R. Kaibyshev, H. Miura, and J.J. Jonas. Dynamic and post-dynamic recrystallization under hot, cold and severe plastic deformation conditions. Prog. Mater. Sci., 2014, vol. 60, pp. 130-207.
9. K. Huang, and R.E. Logé. A review of dynamic recrystallization phenomena in metallic materials. Mater. Design, 2016, vol. 111, pp. 548-574.
10. R. Kaibyshev, K. Shipilova, F. Musin, and Y. Motohashi. Continuous dynamic recrystallization in an Al-Li-Mg-Sc alloy during equal-channel angular extrusion. Mater. Sci. Eng. A, 2005, vol. 396, pp. 341-351.
11. J.C. Li, X.D. Wu, L.F. Cao, B. Liao, Y.C. Wang, and Q. Liu. Hot deformation and dynamic recrystallization in Al-Mg-Si alloy. Mater. Charact., 2021, vol. 173, pp. 110976.
12. F.M.B. Ferraz, R.H. Buzolin, S. Ebenbauer, T. Leitner, A. Krumphals, and M.C. Poletti. A predictive mesoscale model for continuous dynamic recrystallization. Int. J. Plast., 2024, vol. 179, pp. 104022.

13. X.M. Feng, Y.T. Wang, Q.G. Huang, H.L. Liu, and Z.H. Zhang. The dynamic recrystallization microstructure characteristics and the effects on static recrystallization and mechanical properties of Al-Mg-Si alloy. Mater. Sci. Eng., A, 2024, vol. 899, pp. 146454.
14. J.J. Zhang, Y.P. Yi, S.Q. Huang, X.C. Mao, H.L. He, J.G. Tang, W.F. Guo, and F. Dong. Dynamic recrystallization mechanisms of 2195 aluminum alloy during medium/high temperature compression deformation. Mater. Sci. Eng., A, 2021, vol. 804, pp. 140650.
15. T. Sakai, H. Miura, A. Goloborodko, and O. Sitdikov. Continuous dynamic recrystallization during the transient severe deformation of aluminum alloy 7475. Acta Mater., 2009, vol. 57, pp. 153-162.
16. G. Maizza, R. Pero, M. Richetta, and R. Montanari. Continuous dynamic recrystallization (CDRX) model for aluminum alloys. J. Mater. Sci., 2018, vol. 53, pp. 4563-4573.
17. Q. Yang, T. Wojcik, and E. Kozeschnik. Continuous dynamic recrystallization and deformation behavior of an AA1050 aluminum alloy during high-temperature compression. Metals, 2024, vol. 14, pp. 889.
18. J.R. Davis. Aluminum and aluminum alloys[M]. ASM international, 1993.
19. N.N. Greenwood, and A. Earnshaw. Chemistry of the Elements[M]. Elsevier, 2012.
20. T. Kayser. Characterization of microstructure in aluminum alloys based on electron backscatter diffraction. Diss. Universitätsbibliothek Dortmund, 2011.
21. T. Sheppard, and M. G. Tutcher. Development of duplex deformation substructure during extrusion of a commercial Al-5Mg-0.8Mn alloy. Met. Sci., 1980, vol.14, pp. 579-590.
22. F. R. Castro-Fernández, and C. M. Sellars. Static recrystallisation and recrystallisation during hot deformation of Al-1Mg-1Mn alloy. Mater. Sci. Technol., 1988, vol.4, pp. 621-627.
23. D. Ponge, M. Bredehöft, and G. Gottstein. Dynamic recrystallization in high purity aluminum. Scr. Mater., 1997, vol.37, pp. 1769-1775.
24. S. Gourdet, and F. Montheillet. An experimental study of the recrystallization mechanism during hot deformation of aluminium. Mater. Sci. Eng., A, 2000, vol. 283, pp. 274-288.
25. H. Li, Y.C. Huang, and Y. Liu. Dynamic recrystallization mechanisms of as-forged Al-Zn-Mg-(Cu) aluminum alloy during hot compression deformation. Mater. Sci. Eng. A, 2023, vol. 878, pp. 145236.
26. R. Kaibyshev, and S. Malopheyev. Mechanisms of dynamic recrystallization in aluminum alloys. Mater. Sci. Forum, 2014, vol. 794, pp. 784-789.

27. Z.N. Cheng, C.S. Zhang, G.N. Chu, Z.Y. Liu, K.Z. Wang, Z.J. Meng, L. Chen, L. Sun, and G.Q. Zhao. Dynamic precipitation and recrystallization behavior during hot deformation of Al-Zn-Mg-Cu alloy: Experiment and modeling. Int. J. Plast., 2024, vol. 178, pp. 103995.
28. H.J. McQueen, O. Knustad, N. Ryum, and J.K. Solberg. Microstructural evolution in Al deformed to strains of 60 at 400°C. Scr. Mater., 1985, vol.19, pp. 73-78.
29. W. Blum, Q. Zhu, R. Merkel, and H.J. McQueen. Geometric dynamic recrystallization in hot torsion of Al-5Mg-0.6Mn (AA5083). Mater. Sci. Eng., A, 1996, vol. 205, pp. 23-30.
30. M.R. Rokni, A. Zarei-Hanzaki, A.A. Roostaei, and H.R. Abedi. An investigation into the hot deformation characteristics of 7075 aluminum alloy. Mater. Des., 2011, vol. 32, pp. 2339-2344.
31. J.W. Lee, K.T. Son, T.K. Jung, Y.O. Yoon, S.K. Kim, H.J. Choi, and S.K. Hyun. Continuous dynamic recrystallization behavior and kinetics of Al-Mg-Si alloy modified with CaO-added Mg. Mater. Sci. Eng., A, 2016, vol. 673, pp. 648-659.
32. B. Liao, X.D. Wu, L.F. Cao, G.J. Huang, Z.A. Wang, and Q. Liu. The microstructural evolution of aluminum alloy 7055 manufactured by hot thermo-mechanical process. J. Alloys Compd., 2019, vol. 796, pp. 103-110.
33. H.J McQueen, and N.D Ryan. Constitutive analysis in hot working. Mater. Sci. Eng., A, 2002, vol. 322, pp. 43-63.
34. Y.C. Lin, and X.M. Chen. A critical review of experimental results and constitutive descriptions for metals and alloys in hot working. Mater. Des., 2011, vol. 32, pp. 1733-1759.
35. F. Siciliano, Jr., K. Minami, T. M. Maccagno, and J. J. Jonas. Mathematical modeling of the mean flow stress, fractional softening and grain size during the hot strip rolling of C-Mn steels. ISIJ Int., 1996, vol. 36, pp. 1500-1506.
36. J. J. Jonas, X. Quelennec, L. Jiang, and É. Martin. The Avrami kinetics of dynamic recrystallization. Acta Mater., 2009, vol. 57, pp. 2748-2756.
37. S. Gourdet and F. Montheillet. A model of continuous dynamic recrystallization. Acta Metall., 2003, vol. 51, pp. 2685-2699.
38. Z.C. Sun, H.L. Wu, J. Cao, and Z.K. Yin. Modeling of continuous dynamic recrystallization of Al-Zn-Cu-Mg alloy during hot deformation based on the internal-state-variable (ISV) method. Int. J. Plast., 2018, vol. 106, pp. 73-87.
39. S.F. Chen, D.Y. Li, S.H. Zhang, H.N. Han, H.W. Lee and M.G. Lee. Modelling continuous dynamic recrystallization of aluminum alloys based on the polycrystal plasticity approach. Int. J. Plast., 2020, vol. 131, pp. 102710.

40. R.H. Buzolin, M. Lasnik, A. Krumphals, and M.C. Poletti. A dislocation-based model for the microstructure evolution and the flow stress of a Ti5553 alloy. Int. J. Plast., 2021, vol. 136, pp. 102862.
41. Y.B. Li, B. Gu, S. Jiang, Y.Q. Liu, Z.S. Shi, and J.G. Lin. A CDRX-based material model for hot deformation of aluminium alloys. Int. J. Plast., 2020, vol. 134, pp. 102844.
42. F. Chen, X. Tian, G.S. Wu, H.J. Zhu, H.A. O and Z.S. Cui. Coupled quantitative modeling of microstructural evolution and plastic flow during continuous dynamic recrystallization. Int. J. Plast., 2022, vol. 156, pp. 103372.
43. Q. Yang, T. Wojcik, and E. Kozeschnik. Subgrain size modeling and substructure evolution in an AA1050 aluminum alloy during high-temperature compression. Materials, 2024, vol. 17, pp. 4385.
44. J. Driver. The limitations of continuous dynamic recrystallization (CDRX) of aluminium alloys. Mater. Lett., 2018, vol. 222, pp. 135-137.
45. E. Kozeschnik. Encyclopedia of Materials: Metals and Alloys, 2022, vol. 4, Elsevier, Oxford, pp. 521-526.
46. H. Hallberg, M. Wallin, and M. Ristinmaa. Modeling of continuous dynamic recrystallization in commercial-purity aluminum. Mater. Sci. Eng. A, 2010, vol. 527, pp. 1126-1134.
47. C. Poletti, M. Rodriguez-Hortalá, M. Hauser, and C. Sommitsch. Microstructure development in hot deformed AA6082. Mater. Sci. Eng. A, 2011, vol. 528, pp. 2423-2430.
48. E. Nes. Modelling of work hardening and stress saturation in FCC metals. Prog. Mater. Sci., 1998, vol. 41, pp. 129-193.
49. K. Marthinsen, and E. Nes. Modelling strain hardening and steady state deformation of Al-Mg alloys. Mater. Sci. Technol., 2001, vol. 17, pp. 376-388.
50. Y. Huang, and F.J. Humphreys. Subgrain growth and low angle boundary mobility in aluminium crystals of orientation {110} 〈001〉 . Acta Mater., 2000, vol. 48, pp. 2017-2030.
51. F. Roters, D. Raabe, and G. Gottstein. Work hardening in heterogeneous alloys-a microstructural approach based on three internal state variables. Acta Metall., 2000, vol. 48, pp. 4181-4189.
52. P. Sherstnev, P. Lang, and E. Kozeschnik: in Eur. congr. comput. methods appl. sci. eng. (ECCOMAS 2012), 10.-14.9.2012, J. Eberhardsteiner et.al., ed., Vienna, Austria, 2012, pp. 1-8.

53. J. Peŝiĉka A. Dronhofer, and G. Eggeler. Free dislocations and boundary dislocations in tempered martensite ferritic steels. *Mater. Sci. Eng., A*, 2004, vol. 387, pp. 176-180.
54. G.I. Taylor. The Mechanism of Plastic Deformation of Crystals. Part I. Theoretical. Proc. R. Soc. Lond. A, 1934, vol. 145, pp. 362-387.
55. P. Tzanetakis, J. Hillairet, and G. Revel. The formation energy of vacancies in aluminium and magnesium. physica status solidi (b), 1976, vol. 75, pp. 433-439.
56. G Stechauner, and E Kozeschnik. Assessment of substitutional self-diffusion along short-circuit paths in Al, Fe and Ni. Calphad, 2014, vol. 47, pp. 92-99.
57. G.V.S.S. Prasad, M. Goerdeler, and G. Gottstein. Work hardening model based on multiple dislocation densities. Mater. Sci. Eng., 2005, vol. 400, pp. 231-233.
58. M. Goerdeler, and G. Gottstein. A microstructural work hardening model based on three internal state variables. Mater. Sci. Eng., A, 2001, vol. 309, pp. 377-381.
59. H. Mirzadeh, J.M. Cabrera, and A. Najafizadeh. Modeling and prediction of hot deformation flow curves. Metall. Mater. Trans. A, 2012, vol. 43, pp. 108-123.
60. S. Gourdet. Étude des mécanismes de recristallisation au cours de la déformation a chaud de l'aluminium. Matériaux. Doctoral dissertation, Ecole Nationale Supérieure des Mines de Saint-Etienne, 1997. Français.
61. B. Kowalski, A.J. Lacey, and C.M. Sellars. Correction of plane strain compression data for the effects of inhomogeneous deformation. Mater. Sci. Technol., 2003, vol. 19, pp. 1564-1570.

Section B

Scientific Papers

Paper I

Continuous Dynamic Recrystallization and Deformation Behavior of an AA1050 Aluminum Alloy during High-Temperature Compression

Qi Yang, Tomasz Wojcik and Ernst Kozeschnik

Metals
Volume 14, Year 2024, Pages 889.

Continuous Dynamic Recrystallization and Deformation Behavior of an AA1050 Aluminum Alloy during High-Temperature Compression

Qi Yang, Tomasz Wojcik, and Ernst Kozeschnik*

Institute of Materials Science and Technology, TU Wien, Getreidemarkt 9, 1060 Vienna, Austria
*Correspondence: ernst.kozeschnik@tuwien.ac.at

Abstract: Continuous dynamic recrystallization (CDRX) forms a new recrystallized microstructure through the progressive increase in low-angle boundary misorientations (LAGBs) during the hot forming of metallic materials with high stacking fault energy (SFE), such as aluminum alloys. The present work investigates the effect of deformation parameters on the evolution of the dynamic recrystallization microstructures of an AA1050 aluminum alloy during compression at elevated temperatures. The alloy microstructure is investigated at deformation temperatures and strain rates in the range of 300 °C to 500 °C and 0.001 to 0.8 s^{-1}. A well-defined substructure and subsequent DRX grains provide indication that recrystallization can proceed with continued strain under high-temperature compression. At a strain rate of 0.1 s^{-1}, the DRX fraction is observed to be 0.25 at a temperature of 300 °C. This fraction increases to 0.32 as the temperature rises to 400 °C. The recrystallization mechanism is identified by analyzing the flow stress, the evolution of the subgrain misorientation angle, and the distribution of recrystallized grains. The observations of discontinuous dynamic recrystallization (DDRX) and CDRX under various deformation parameters are discussed. Moreover, the main substructure evolution laws observed from the high-temperature compression of an AA1050 Al alloy are summarized.

Keywords: dynamic recrystallization; microstructure; flow curve; high-temperature compression; aluminum alloy

1. Introduction

Aluminum alloys are widely used in automotive, aerospace, and other industries due to their lightweight properties and mechanical performance. Hot forming of aluminum alloys is a rather complex metallurgical process, including work hardening (WH), dynamic recovery (DRV), static recovery (SRV), dynamic recrystallization (DRX), grain growth, etc. [1-3] Over the past few decades, many researchers [4-6] have studied the recrystallization behavior and

microstructure evolution of different materials. The recrystallization and related annealing phenomena largely determine the final microstructure and mechanical properties of the alloys.

For aluminum alloys, it is generally accepted that dynamic recovery is an essential softening mechanism during hot forming, which is attributed to their high-stacking fault energy. In addition, dynamic recrystallization may occur, as frequently observed with advanced experimental characterization techniques. The DRX mechanisms in Al alloys are classified into three types: discontinuous dynamic recrystallization (DDRX) [7-9], continuous dynamic recrystallization (CDRX) [10-13], and geometric dynamic recrystallization (GDRX) [14-15]. DDRX usually occurs in high-purity Al [16], in Al-Mg-Mn alloys with high Mg solute addition [17], and in aluminum alloys that contain large particles (>1 μm) [18]. DDRX is characterized by clearly distinguishable nucleation and growth stages. GDRX usually occurs when grains become highly elongated during large strain deformation, and the grain thickness approaches roughly one to two times the subgrain size. McQueen and co-workers [14] observed GDRX in the large strain hot forming of aluminum alloys. Also, GDRX was found in aluminum alloys [19] during severe strain and hot deformation of Al-Mg-Si alloys [20].

In the hot forming process, CDRX is the most commonly occurring mechanism observed in Al alloys, having been observed in equal-channel angular extrusion of Al-Li-Mg-Sc alloys [11], hot compression of AA7075 [21], hot torsion of Al-Mg-Si alloys [22], hot deformation of aluminum alloy 7055 with strain rates $\leq 0.1\ s^{-1}$ [23], hot deformation of the 2195 aluminum alloy at high temperatures (420-520 °C) [24], and others. In contrast to DDRX, CDRX is a non-nucleation process; the mechanism of CDRX is the continuous rotation of subgrains. [25-26] The permanent absorption of new mobile dislocations into low-angle subgrain boundaries (LAGBs) increases their misorientation until the LAGBs finally transform into high-angle grain boundaries (HAGBs).

The question of whether dynamic recrystallization proceeds as continuous, discontinuous, or geometric dynamic recrystallization is largely controlled by the particular hot deformation conditions [27]. It is interesting to note that the occurrence and transition of recrystallization will change by variations in temperature or initial grain size, among other factors, even for the same material. For example, DDRX and CDRX are reported for high-SFE high-purity Al [28-29]. Zhang et al. [24] reported that DDRX is the main DRX mechanism at 300-360 °C and CDRX is the main mechanism at 420-520 °C for the 2195 Al alloy. Thus, exploring the microstructural evolution of Al alloys would play a crucial role in understanding such a phenomenon. In this study, an AA1050 pure aluminum alloy is selected due to its minimal solute atoms and precipitated particles, which act as tangled locations for dislocation structure

generation in other aluminum series.

The present study investigates the effect of deformation parameters on the evolution of the dynamic recrystallization microstructures for an AA1050 aluminum alloy under thermal compression loading. The occurrence of a well-defined substructure and subsequent DRX grains can provide indications that recrystallization can proceed with continued strain under high-temperature compression. The microstructures are analyzed under different temperatures and strain rates, and different recrystallization mechanisms are evaluated by analyzing the flow stress, the variation in misorientation angles, and the distribution of recrystallized grains. The criteria for DDRX and CDRX under different deformation parameters are quantified using experimental data, leading to the determination of a maximum temperature window for recrystallization. In addition, the observations and mechanisms of DDRX and CDRX are discussed.

2. Materials and Methods

The material investigated in this research is an AA1050 aluminum alloy provided by Neuman Aluminium Austria GmbH (Neuman Aluminium, Marktl, AT). in the form of aluminum billets. The chemical composition is summarized in Table 1. The specimens were machined into cylinders from the center position of the billet, with a diameter of 5 mm and a height of 10 mm. To minimize friction between the specimen and the dies, the end faces of the specimens were polished. Graphite lubricant and a tantalum sheet were used between the surfaces of anvils and specimens.

Table 1. Chemical composition of AA1050 aluminum alloy (wt%).

Si	Fe	Cu	Mn	Mg	Cr	Zn	Ti	Al
0.08	0.26	<0.01	<0.01	<0.01	<0.01	<0.01	<0.01	99.63

Single-pass isothermal compression was performed on a high-speed quenching and deformation dilatometer, DIL 805 A/D, from Bähr. In the investigation, a temperature ranges from 300 °C to 500 °C and a strain rate range from 0.001 to 0.8 s^{-1} were used for thermo-mechanical processing and computer simulation. This corresponds to a deformation temperature range of $0.5T_m < T_{def} < 0.7T_m$, as recommended for CDRX by Sakai et al. [30] and Driver [31]. The melting temperature of the alloy is 625 °C, as calculated with MatCalc [32] software version 6.04 (http://matcalc.at) and the open mc_al.tdb database (version 2.036) available on the MatCalc web site.

As shown in Figure 1, the specimens were heated to the deformation temperature at a heating rate of 10 K/s and held for 180 s before compression, followed by compression under different conditions. The true strain ranged from 0 to 0.9. To preserve the subgrain/grain structure and the occurrence of the DRX, the specimens were high-speed quenched with almost 100 K/s cooling speed to room temperature immediately after compression.

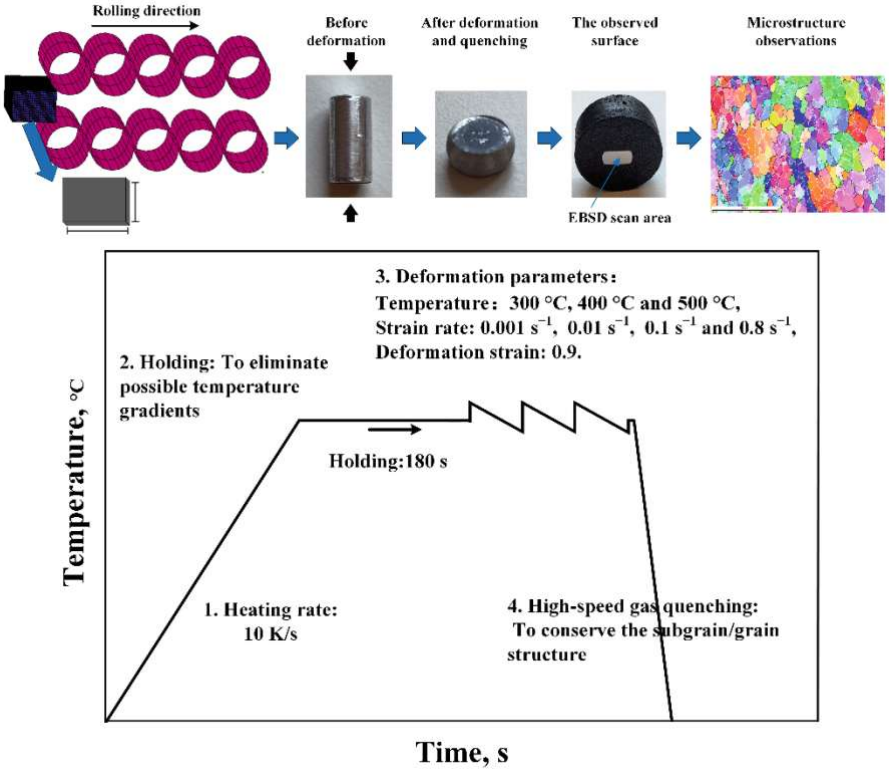

Figure 1. Schematic of the isothermal compression test procedures**.**

Electron backscatter diffraction (EBSD, EDAX Inc., Mahwah, NJ, USA) measurement was carried out using a Zeiss Sigma 500VP high-resolution scanning electron microscope with an EDAX detector (Zeiss, Oberkochen, DE). The sample preparation for EBSD consists of standard mechanical grinding and polishing, followed by OP-S polishing with an automatic polishing device (Struers Inc., Hovedstaden, DK). EBSD mappings were recorded at an accelerating voltage of 20 kV and a step size of 0.5 μm at the center of the deformed regions of the mid-width location. The data processing of EBSD results was completed by using EDAX OIM Analysis8 software (v8, EDAX Inc., Mahwah, NJ, USA).

3. Results

3.1. Microstructure Evolution

The microstructure evolution of the AA1050 aluminum alloy is characterized by electron

backscatter diffraction (EBSD). Figure 2a-c show the microstructure after compression at temperatures of 300 °C, 400 °C, and 500 °C. The true strain in the experiments is 0.9. Low-angle subgrain boundaries (LAGBs) with 2° < misorientation < 15° and high-angle grain boundaries (HAGBs) with misorientation > 15° are shown as white and black lines, respectively. From the inverse pole figure (IPF) maps, a duplex grain structure is observed stemming from (I) deformed parent grains with elongated shapes perpendicular to the direction of compression; (II) the recovered microstructure with a large number of equiaxed LAGBs within the elongated parent grains due to DRV; (III) the recrystallized microstructure with a large number of newly formed fine grains within parent grains or near/on the parent grain boundaries. A combination of (I), (II), and (III) leads to a typical microstructure comprising LAGBs and HAGBs.

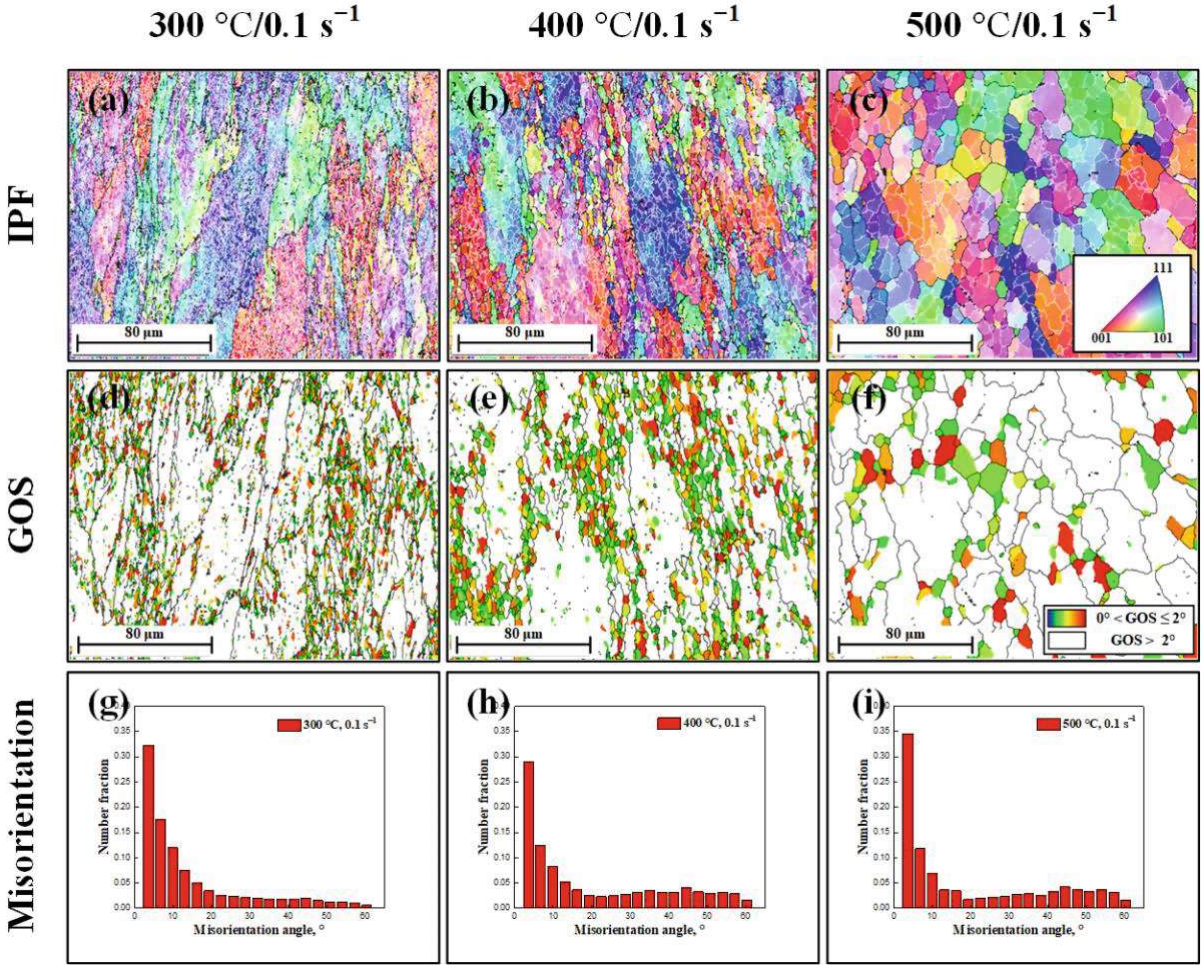

Figure 2. EBSD images of AA1050 aluminum alloy deformed to a strain of 0.9 with a strain rate of 0.1 s^{-1}: (a-c) inverse pole figure (IPF) maps of the specimens deformed at 300, 400, and 500 °C; (d-f) grain orientation spread (GOS) maps with high-angle grain boundaries; and (g-i) distribution histograms of misorientation angle.

Figure 2a shows the microstructure after deformation at 300 °C and a strain rate of 0.1 s^{-1}.

The interior of the elongated grains contains a high density of LAGBs, which is the typical substructure observed after DRV. In materials with high SFE (such as Al, Ti, etc.), and in contrast to those with low and medium SFE (deformation conditions under which DRV is not particularly rapid), the rearrangement and annihilation of dislocations readily take place through DRV, leading to the formation of LAGBs in the pancaked parent grains [30, 33]. Moreover, some fine recrystallized grains are visible within the deformed parent grains, although DRV (main softening type) reduces the driving force for the occurrence of DRX.

More recrystallized grains with equiaxed morphology are observed in Figure 2b, c. An increase in temperature promotes the generation of subgrain boundaries and their mobility, thus promoting the formation of DRX grains [30, 33]. Obviously, the average size of subgrains increases with temperature. The average subgrain size of the specimens deformed to strain 0.9 at different deformation conditions of 300 °C/0.1 s^{-1}, 400 °C/0.1 s^{-1}, and 500 °C/0.1 s^{-1} is obtained as 1.70 µm, 3.50 µm, 11.00 µm, respectively. The effect of the strain rate on the microstructure is shown in Figure 3. Fine subgrains and recrystallized grains are generated at low strain rates, which emphasizes that the low strain rate promotes DRX at this temperature. The lower strain rate corresponds to an elongation of the deformation time, which supports the transition from LAGBs to new DRX grain boundaries and, thus, the formation of DRX grains [34].

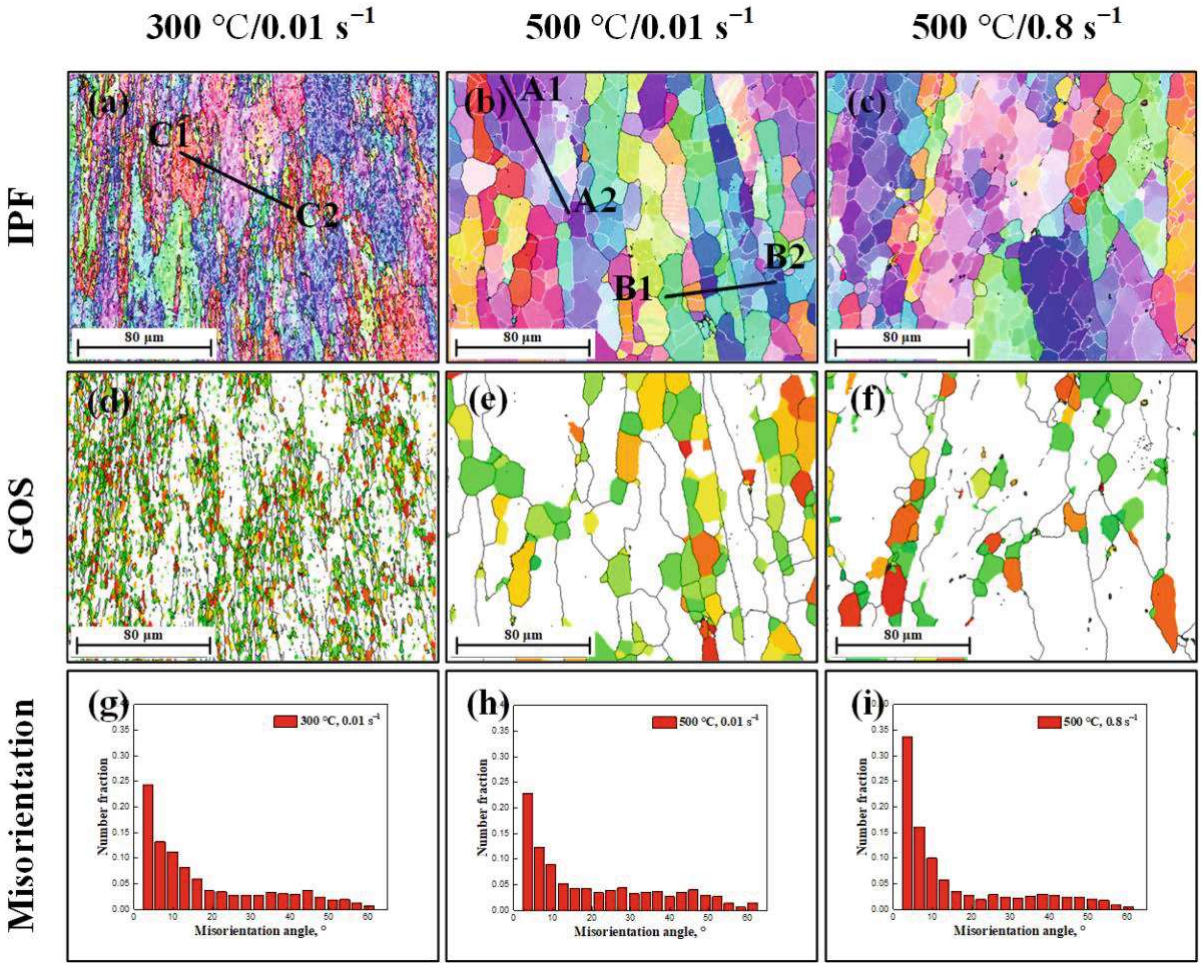

Figure 3. EBSD images of AA1050 aluminum alloy deformed to strain of 0.9: (a-c) IPF maps of specimens deformed at 300 °C/0.01 s^{-1}, 500 °C/0.01 s^{-1}, and 500 °C/0.8 s^{-1}; (d-f) GOS maps with high-angle grain boundaries; and (g-i) distribution histograms of misorientation angle.

The corresponding distribution histograms of misorientation angles are shown in Figures 2 and 3. It was clear that the misorientation angle exhibited a relatively random distribution. The average misorientation angle of the specimens gradually increased with increasing deformation temperature or decreasing strain rate. Accordingly, low-angle subgrain boundaries absorbing dislocations and transforming into HAGBs were responsible for an increase in the misorientation angle, which is also considered a typical identification of DRX phenomena [1, 30, 33].

The misorientation profiles along the black lines A1 to A2, B1 to B2, and C1 to C2 in Figure 3a and 3b are displayed in Figure 4, which represents the distribution of local point-to-point and cumulative (point-to-origin) misorientations developed in grain interiors along the lines. In the misorientation profile, several low misorientation fluctuations can be observed, which confirms the formation of new subgrains. More misorientation angles greater than 15°

indicate the occurrence of subgrain rotation, accompanied by the formation of new recrystallized grains.

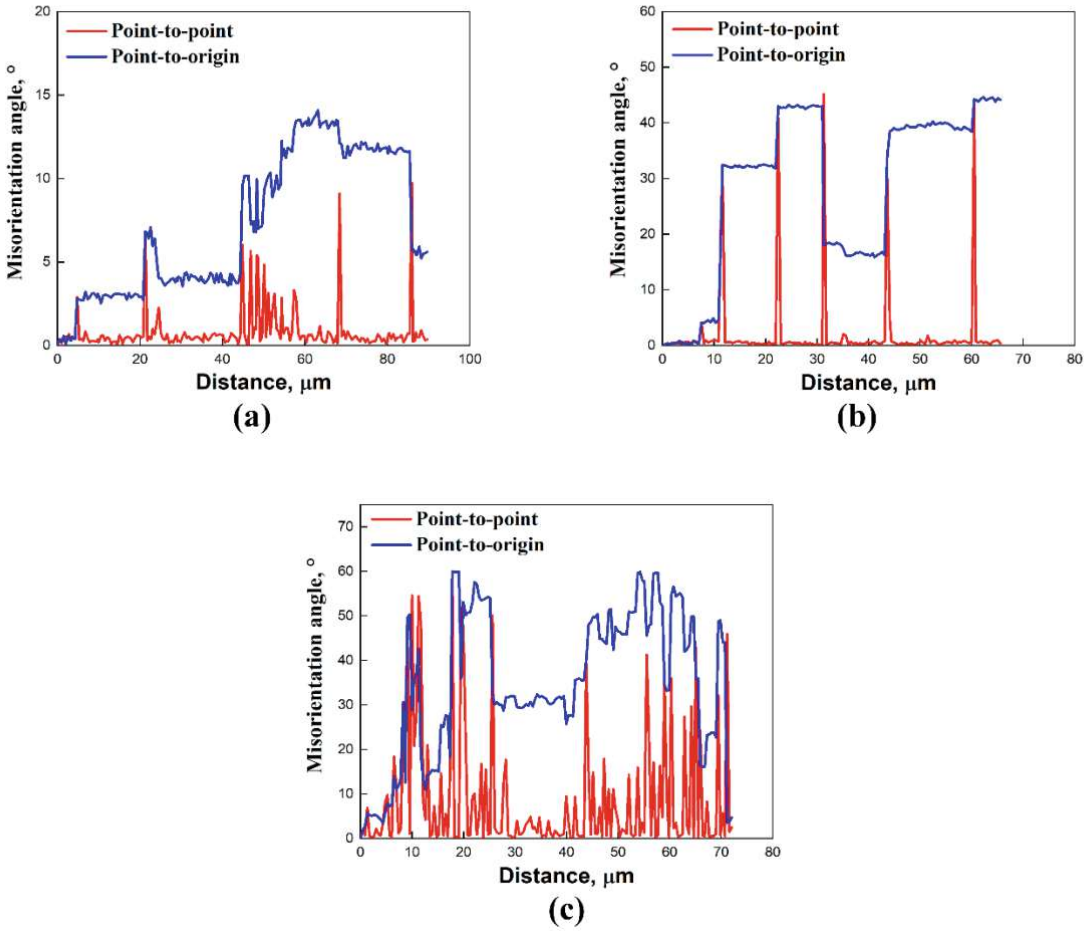

Figure 4. Cumulative misorientation profiles along the lines of recrystallized grains: (a) A1-A2, (b) B1-B2, and (c) C1-C2.

3.2. DRX at Medium or High Temperatures

The grain orientation spread (GOS) is used to assist in observing the characteristics of DRX, which denotes the deviation in the misorientation angles of every pixel of a grain with respect to the mean grain orientation. The grains with a GOS less than 2° are regarded as DRX grains.

Figures 2d and 3d show the GOS maps of the specimens deformed at 300 °C, in which two characteristics of DRX are observed. Partially recrystallized grains are mainly located along the grain boundary with a necklace structure, which is consistent with the result that DDRX can occur at medium temperatures [24]. The corresponding grain boundary map of the specimens deformed at a medium temperature (300 °C) is shown in Figure 5a. Recrystallized grains that are nucleated directly inside the parent grains can also be found, demonstrating the

existence of CDRX. Therefore, two types of recrystallizations coexist at this temperature.

Through the GOS maps of Figure 2, an obtained conclusion is that the DRX fraction in the microstructure gradually increases with a decrease in the strain rate or an increase in temperature. When the strain rate is 0.1 s^{-1}, the DRX fraction at a temperature of 300 °C is observed to be 0.25. This fraction increases to 0.32 as the temperature rises to 400 °C, confirming the occurrence of recrystallization during deformation. Concurrently, the size of DRX grains shows visible increases with the elevation of the deformation temperature. At a deformation temperature of 500 °C, the DRX fraction at a strain rate of 0.01 s^{-1} is 0.34, representing a significant increase from 0.20 at a strain rate of 0.8 s^{-1} (see Figure 3).

When subjected to deformation at high temperatures, the presence of coarse subgrains becomes evident, as seen in Figure 5b. There is no obvious necklace structure, and the DRX process is constituted in the transformation from LAGBs to HAGBs.

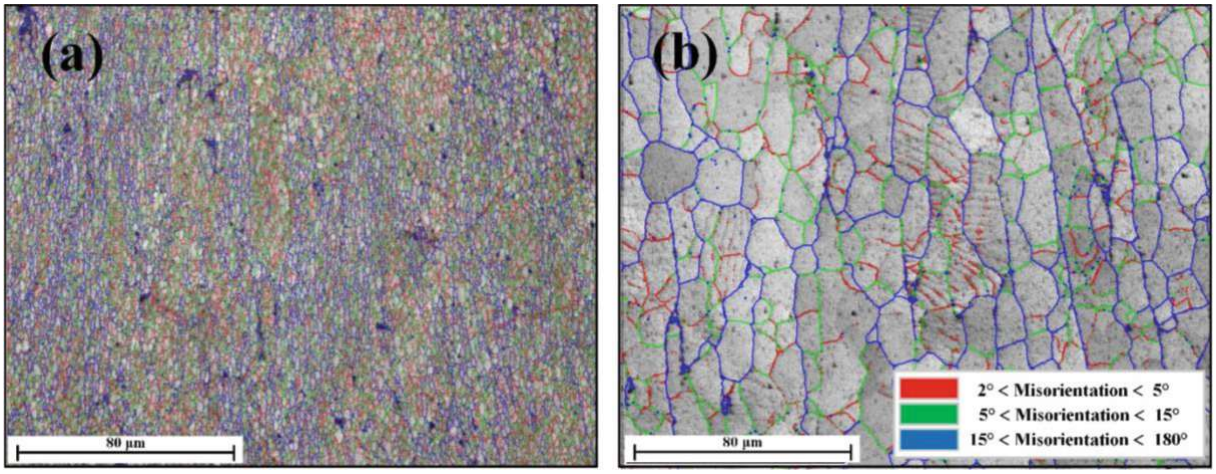

Figure 5. Grain boundary maps of the specimens deformed at (a) 300 °C/0.01 s^{-1} and (b) 500 °C/0.01 s^{-1} (red, green, and blue lines represent boundaries with misorientation angles in the 2-5°, 5-15°, and > 15° ranges, respectively).

3.3. Flow Stress Behavior

The flow curves measured for various deformation parameters are shown in Figure 6. The true strain of deformation is between 0 and 0.9. At the early stage of deformation, work hardening plays the dominant role, leading to dislocation multiplication and tangling, resulting in a continuous increase in the flow stress. With continuing deformation, the dynamic softening mechanisms become increasingly prominent and eventually balance the continuous generation of dislocations. The dynamic softening effect can be exhibited by either dynamic recrystallization (DRX) and/or dynamic recovery (DRV), with both processes leading to either a plateau in the flow stress curve or even a reduction in stress. In the latter case, the flow stress curve is characterized by a peak. For Al alloys, both types of softening are observed [33]. As

expected, the flow stress is sensitive to deformation temperature and strain rate, i.e., the flow stress decreases with an increasing deformation temperature or a decreasing strain rate.

The critical strain associated with the initiation of DRX is a pivotal quantity in studies of material behavior with continuous deformation. According to Poliak and Jonas [35] and Ryan and McQueen [36], the characteristic strains of dynamic softening can be identified by analyzing the transition points on the $\theta - \sigma$ curve ($\theta = \mathrm{d}\sigma/\mathrm{d}\varepsilon$), where θ is the rate of work hardening (WH), σ is the true stress, and ε is the strain. The characteristic point curve in the flow curves is shown in Figure 7.

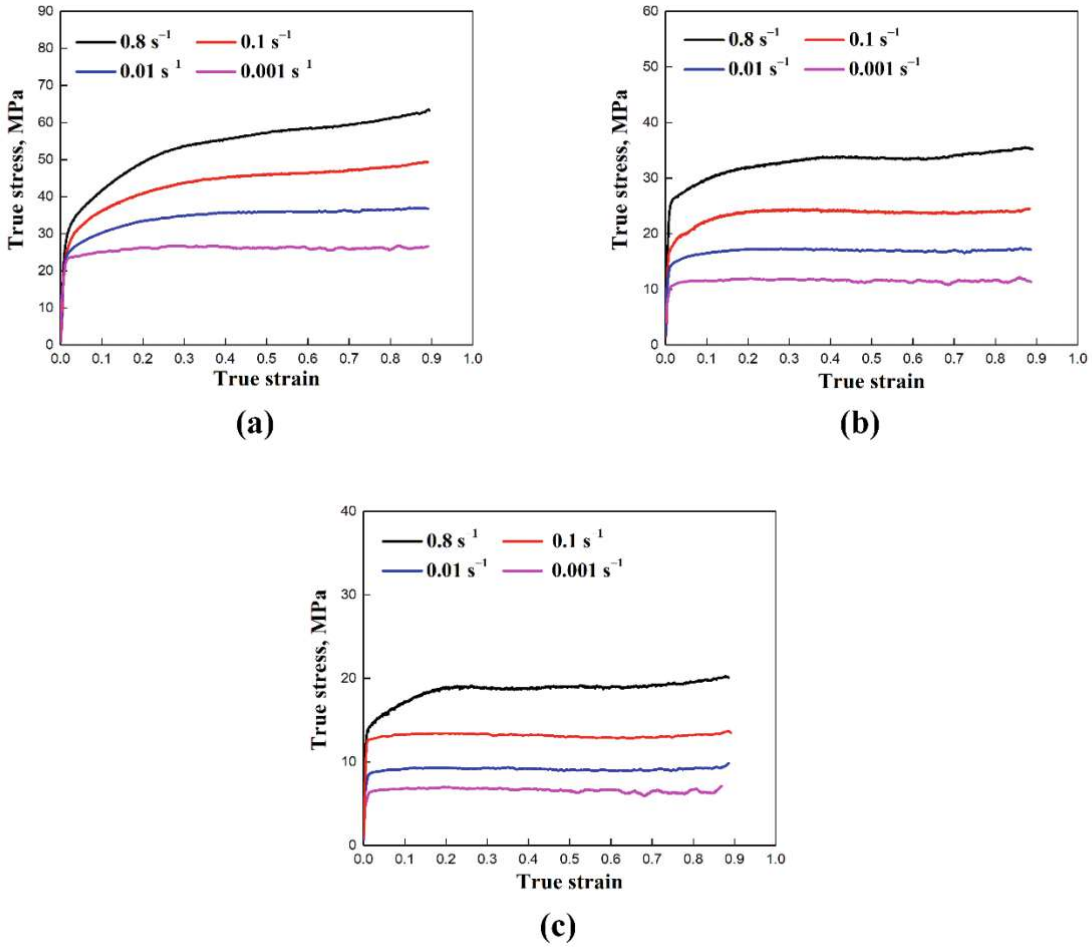

Figure 6. The stress-strain curves for various compression parameters: (a) 300 °C, (b) 400 °C, and (c) 500 °C.

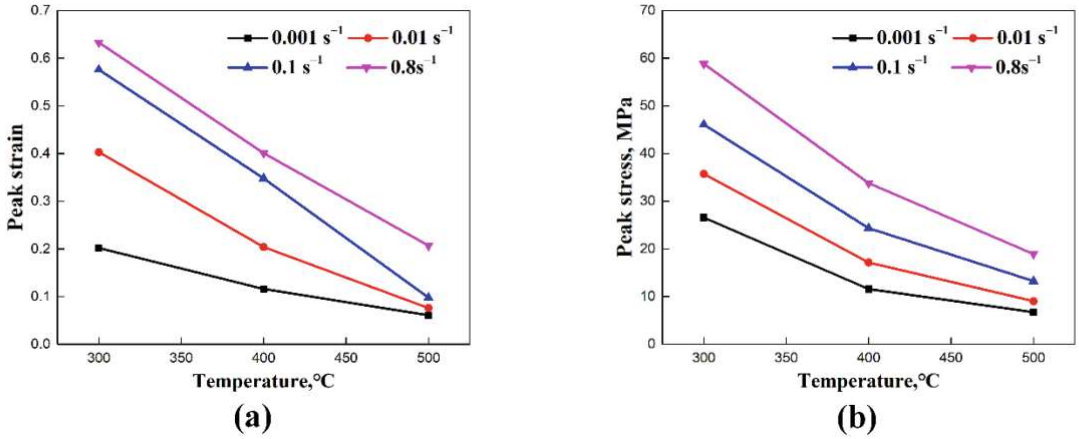

Figure 7. Characteristic point curves in the flow curves: (a) peak strain and (b) peak stress.

First, the peak strain ε_p under different deformation conditions is evaluated from the experimental data of the AA1050 alloy and fitted with an Arrhenius-type equation as

$$\varepsilon_p = 0.00408\dot{\varepsilon}^{0.179}(\exp\left(\frac{142000}{RT}\right))^{0.179}, \quad (1)$$

where $\dot{\varepsilon}$ is the strain rate, R is the gas constant, and T is the absolute deformation temperature. The value of deformation activation energy Q is 142 KJ.mol^{-1} for pure aluminum [37]. The relationship of $\ln \varepsilon_p$ and $\ln(\dot{\varepsilon}\exp(Q/RT))$ is plotted in Figure 8.

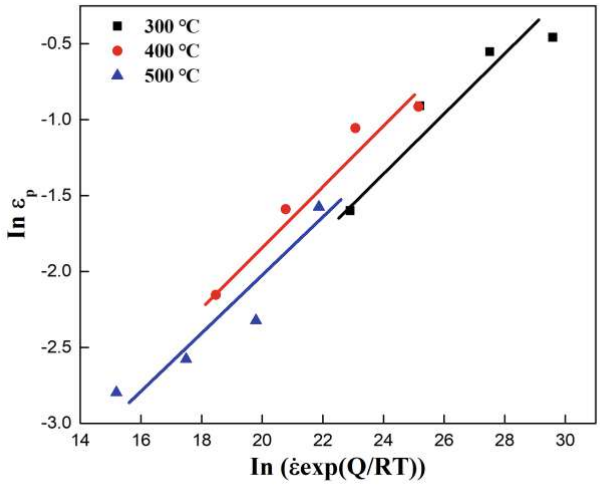

Figure 8. The relationship between $\ln \varepsilon_p$ and $\ln(\dot{\varepsilon}\exp(Q/RT))$.

In previous reports [35,38], the easiest way to determine the critical strain ε_c for a given material is through the assumption of a critical strain ratio, which represents a fixed proportion between ε_c and ε_p. Accordingly, the calculation of the critical strain at which recrystallization

initiates can be written as

$$\varepsilon_c = f_\varepsilon \, \varepsilon_p, \tag{2}$$

where f_ε is the critical strain ratio between critical strain and peak strain. For the determination of f_ε, the work of Cingara and McQueen [39] is utilized, where the value of f_ε is suggested to be in the order of 0.5.

4. Discussion

4.1. High-Temperature Deformation Behavior

It is well known that the complete thermal deformation process of most metals can be divided into four stages [1,40,41]: stage I (WH stage), stage II (transition stage), stage III (softening stage), and stage IV (steady-state stage). There have been many studies [1,30,33] describing these four stages in detail and the corresponding three typical behaviors of WH, DRV, and DRX.

Figure 9 illustrates the typical flow curves associated with various modes of dynamic softening, which result in different flow curve behaviors and their corresponding characteristics. For Al alloys (high SFE), two distinct forms of flow curves are typically observed, as illustrated in Figure 6. In the case of CDRX, competition between WH and dynamic softening (DRV and DRX) takes place, which slows down the increase rate of the flow stress. The microstructures displayed in Figures 2 and 3 clearly show that the softening is caused by DRV and DRX, resulting in the occurrence of a well-defined substructure and new fine recrystallized grains. The second type of high-temperature behavior is characterized by a continuous increase in flow stresses (mainly WH+DRV). The rate of strain hardening slowly decreases with deformation and approaches zero at high strains.

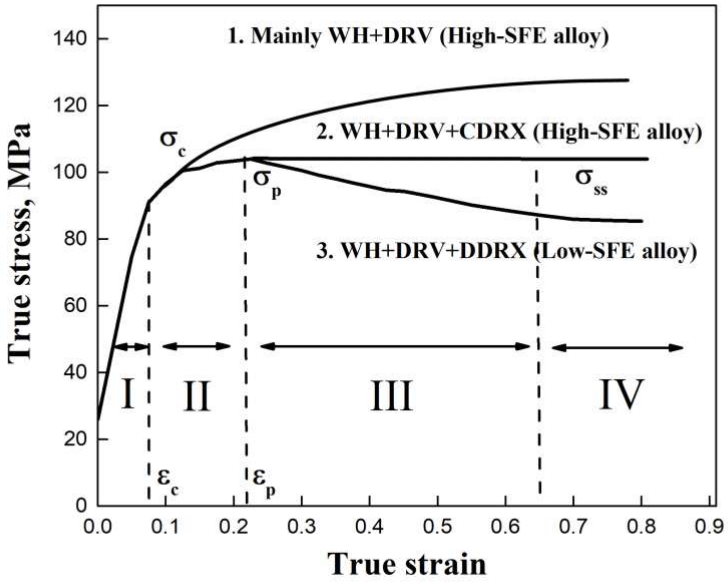

Figure 9. Typical flow curves for different modes of dynamic softening [1,30,33].

For Al alloys, the flow curves typically exhibit rapid stress saturation at high temperatures (case 2 in Figure 9), compared with the flow curve of DDRX. In addition, a continuously increasing flow curve (case 1 in Figure 9) can be found at a medium temperature (300 °C) and high strain rate. Figure 10 illustrates the microstructure obtained at 300 °C, a strain rate of 0.8 s^{-1}, and a strain of 0.9. Due to the high SFE, the operation of multiple slip systems leads to the formation of dense dislocation walls (DDWs) on the slip planes. [42] A substantial increase in fine substructures results in a higher dislocation density of geometrically necessary boundaries (GNBs), thereby resulting in a continued increase in flow stress. The microstructures presented in Figures 2 and 3 demonstrate a significant influence of temperature and strain rate on the substructure. The formation of finer subgrains is observed at a temperature of 300 °C (almost $0.5T_m$) and a high strain rate, in accordance with the conclusions reported by Yang et al. [43]. The formation of a cell-like substructure and dislocation strengthening contribute to a sustained upward trend in the flow curve of hot deformation.

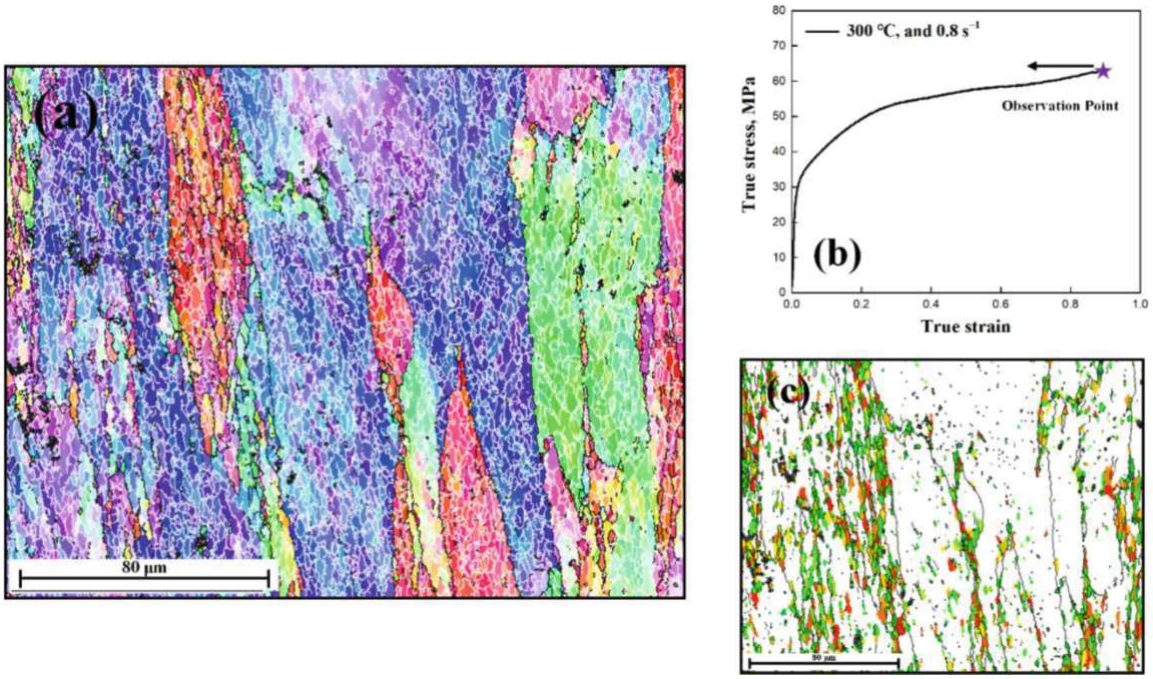

Figure 10. (a) Microstructure obtained at 300 °C/0.8 s^{-1}, with strain of 0.9; (b) corresponding flow curve; and (c) corresponding GOS map.

4.2. DDRX to CDRX Accompanied by Temperature and Strain Rate Changes

The detailed recrystallization grain boundary characteristics are shown in Figure 11. A more detailed EBSD observation is employed to investigate the evolution of subgrain and DRX boundaries (the scale is 20 microns in maps). As shown in Figure 11a, the substructure is formed with insufficient thermal energy to exhibit strong DRV [44], thus making it difficult to form a polygonal structure. Therefore, DDRX leads to the formation of a necklace microstructure along the grain boundaries. Simultaneously, some already formed subgrains can still transform their LAGBs into HAGBs and form fine continuously recrystallized grains. So, two recrystallization modes persist simultaneously at this temperature.

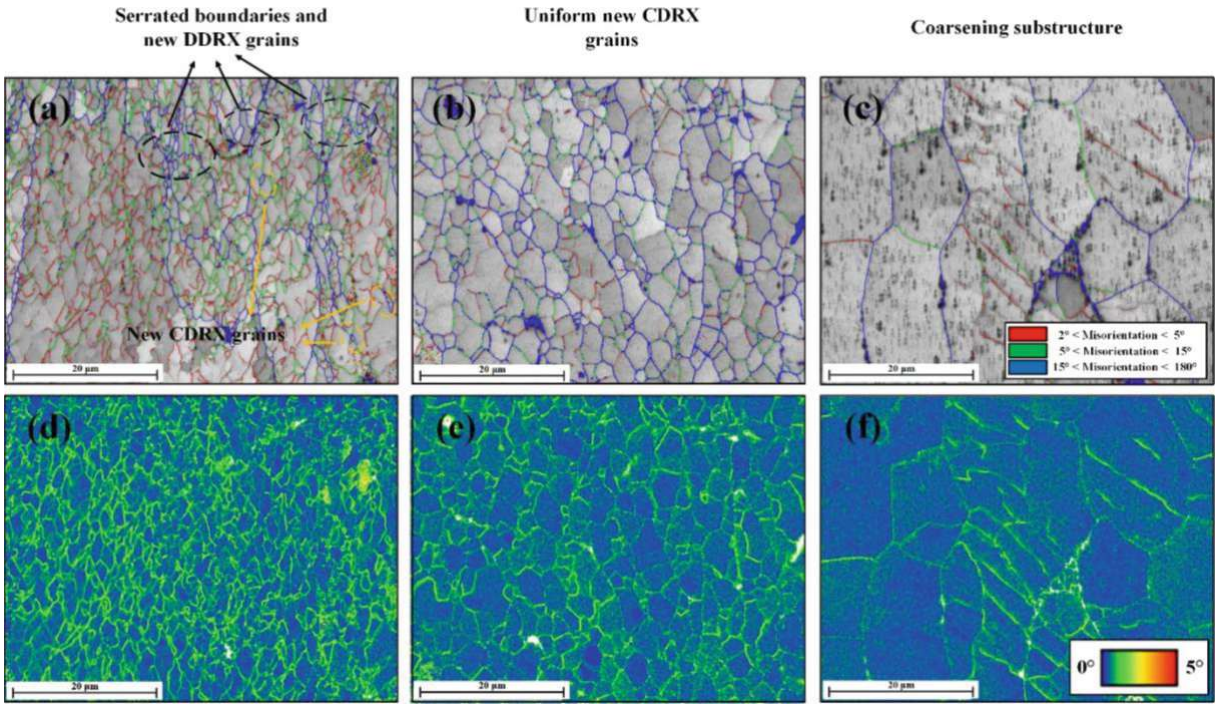

Figure 11. EBSD images of an AA1050 aluminum alloy deformed at different temperatures to a strain of 0.9: (a-c) grain boundary maps of the specimens deformed at (a) 300 °C/0.1 s^{-1}, (b) 400 °C/0.1 s^{-1}, and (c) 500 °C/0.1 s^{-1}; (d-f) corresponding KAM (Kernel Average Misorientation) maps.

Different from Figure 11a, more recrystallized grain boundaries are observed with increasing temperature, indicating more completed DRX (Figure 11b, c). Typical structures of DDRX, such as necklace structures and grain boundary bulging, do not appear. Instead, an equiaxed morphology is observed. This indicates that the nucleation mode of CDRX is mainly the formation of LAGBs by DRV, first, and the following transformation of LAGBs into HAGBs by subgrain rotation. It is also obvious from Figure 11b that the new recrystallized grains are uniformly distributed. As the temperature continues to increase, a coarser substructure is formed by the new grains, making the formation of new LAGBs difficult.

The KAM (Kernel Average Misorientation) maps support further discussion of results. Figure 11d shows the KAM map after deformation at 300 °C. The KAM adopts a higher value at LAGBs/grain boundaries, while a low KAM is observed in the grain interior. Higher KAM values refer to larger dislocation density and also higher stored deformation energy. Since dislocation generation continues while deformation proceeds, more and more dislocations are piled up to form new subgrains/LAGBs. Similarly, clear substructures visualized by high KAM stripes are also observed at higher temperatures (see Figure 11e, f). Gao et al. [45] report that the density of geometrically necessary dislocations (GNDs) is related to the local misorientation angle (KAM value) with $\rho_{GND} = 2\theta/\mu b$. If the average KAM increases sharply, the density of

GNDs formed locally increases continuously.

Figure 12 shows the EBSD images after deformation at 300 °C and a low strain rate of 0.001 s^{-1}. It is worth noticing that the operation of various DRX modes is contingent upon the different strain rates. At a low strain rate of 0.001 s^{-1}, typical structures of DDRX, such as necklace structures and grain boundary bulging, are notably absent. The appearance of a well-defined substructure and incomplete HAGBs confirms the progressive transformation of subgrain boundaries towards recrystallized grain boundaries. This provides an indication for the operation of CDRX under these conditions. DDRX may occur but is not dominant. In contrast to the low strain rate, there is an acceleration in the migration of grain boundaries (HAGBs) at a higher strain rate, thus forming wavy shapes with different curvatures [46]. The extra driving force exerted along the parent grain boundaries leads to the bulging of these boundaries, thereby facilitating DDRX.

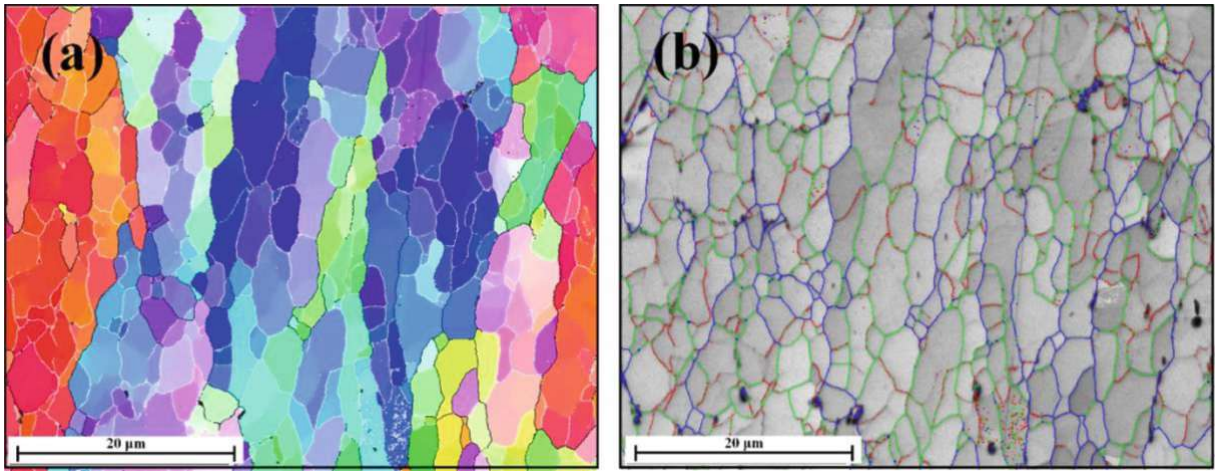

Figure 12. EBSD images of AA1050 aluminum alloy deformed (strain of 0.9) at 500 °C/0.001 s^{-1}: (a) IPF map and (b) corresponding grain boundary map.

4.3. Illustration of DRX Mechanisms

Figure 13 illustrates a sketch of the observed DRX mechanisms. Before deformation, the parent grains exhibit an initial microstructure with a relatively low excess dislocation density. Figure 13b describes the early stage of deformation, where dislocation accumulation through DRV leads to the formation of new subgrain boundaries, thereby inducing a significant reduction in the mean subgrain size. Subsequently, as deformation progresses, DRX starts to occur with the generation of new recrystallized grains and a concurrent decrease in overall dislocation density. Then, DRX and recovery processes persist until a steady state is eventually reached. On comparing Figures 2, 3, and 11, it is obvious that an increase in temperature results in the formation of coarsening substructures. Additionally, there are notable changes in the

types of DRX observed.

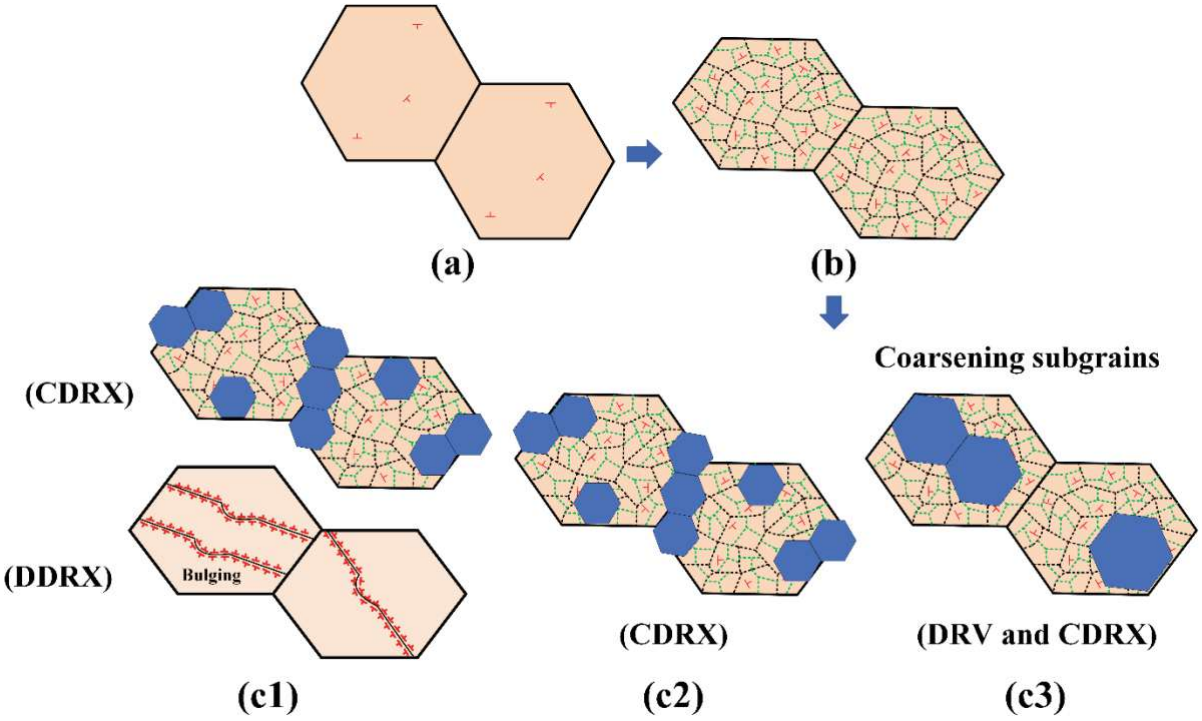

Figure 13. Schematic diagram of DRX mechanism: (a) initial microstructure before deformation, (b) generation of cells and subgrains, (c1) generation of recrystallized grains when the deformation temperature is almost $0.5T_m$, (c2) $0.5T_m$ < deformation temperature < $0.7T_m$, and (c3) deformation temperature > $0.7T_m$.

Figure 13(c1) represents the coexistence of DDRX and CDRX at a deformation temperature of almost $0.5T_m$. For DDRX, the newly formed recrystallized grains exhibit a necklace-like structure as they nucleate and grow into areas characterized by a high dislocation density. This process is facilitated by the mechanism of grain boundary bulging when the stored energy is sufficient to start recrystallization [30, 33]. The microstructures presented in Section 3 clearly demonstrate the transformation of LAGBs into HAGBs at high temperatures, which is characterized by a homogeneous increase in misorientation. New CDRX recrystallized grains are generated when the misorientation angles reach a critical value, in accordance with the conclusions reported by Huang et al. [33]. Figure 13(c2, c3) describe the recrystallization mechanism at high-temperature deformation with temperatures > $0.5T_m$, where CDRX is the main DRX mode.

The microstructure evolution and related discussion describe the formation of a well-defined substructure and subsequent DRX. The main substructure evolution laws observed from the high-temperature deformation of an AA1050 Al alloy can be summarized as follows: (i) The flow stress increases with strain, showing two different curve types for an AA1050 Al

alloy. Similarly, the density of geometrically necessary dislocations (GNDs) increases with strain, accompanied by the formation of subgrain boundaries. The density of GNDs is greatly related to the subgrain size. (ii) The average subgrain size decreases with deformation. Additionally, the subgrain size is notably influenced by variations in deformation conditions. The present results show that the average subgrain size eventually reaches a "saturation value" at large strains, which is no longer sensitive to the strain [33, 47, 48]. (iii) DRX can occur during medium- or high-temperature compression of an AA1050 Al alloy, appearing as DDRX and/or CDRX, which is influenced by the deformation temperature, strain rate, strain, etc.

5. Conclusions

The hot deformation behavior, microstructure evolution, and the DRX mechanisms of an AA1050 aluminum alloy are investigated by high-temperature compression at various deformation parameters. The main conclusions are as follows:

(1) The typical effects of deformation conditions on the flow behavior of an AA1050 aluminum alloy are observed, revealing distinct variations in the flow curves associated with recrystallization and recovery processes. The peak strain and critical strain under different deformation conditions are evaluated from the experimental data.

(2) A detailed DRX analysis is provided with subgrain/grain boundary characteristics. The formation of a well-defined substructure and the subsequent transformation of LAGBs to HAGBs are significant, which provides indication that recrystallization can proceed with continued strain under high-temperature compression. The DRX fraction at a condition of 300 °C/0.1 s^{-1} is observed to be 0.25. This fraction increases to 0.32 as the temperature rises to 400 °C. These deformation conditions have a clear effect on the microstructure, DRX fraction, and misorientation.

(3) The DRX process of the AA1050 aluminum alloy consists of DDRX and CDRX. The nucleation of DDRX grains occurs at the initial grain boundaries and is characterized by bulging of the initial high-angle grain boundaries. The second observed recrystallization type is the formation of fine recrystallized grains that occur inside the grains, which are considered to stem from CDRX. The mechanism and deformation parameters, in which recrystallization occurs, are discussed in detail in light of the experimental results.

(4) The occurrence of DDRX or CDRX varies with changes in deformation conditions, such as the temperature and strain rate. The coexistence of DDRX and CDRX at almost $0.5T_m$ and a low strain rate has been observed, while CDRX is the main recrystallization mode when

the deformation temperature is increased (>0.5T_m). These variations determine the evolution of the substructure.

Author Contributions: Conceptualization, Q.Y. and E.K.; methodology, Q.Y., T.W., and E.K.; validation, Q.Y. and E.K.; formal analysis, Q.Y.; investigation, Q.Y. and T.W.; resources, E.K. and T.W.; data curation, Q.Y. and T.W.; writing—original draft preparation, Q.Y. and E.K.; writing—review and editing, E.K.; visualization, Q.Y., T.W., and E.K.; supervision, E.K.; project administration, E.K.; funding acquisition, Q.Y. and E.K. All authors have read and agreed to the published version of the manuscript.

Funding: This research received no external funding.

Data Availability Statement: The raw data supporting the conclusions of this article will be made available by the authors on request.

Acknowledgments: Open Access Funding by TU Wien. Qi Yang appreciates the financial support from the State Scholarship Fund of China (No. 202107710006) during his PhD at TU Wien.

Conflicts of Interest: The authors declare no conflicts of interest.

References

1. F.J. Humphreys, and M. Hatherly, Recrystallization and Related Annealing Phenomena, 2nd ed.; Elsevier: Oxford, UK, 2004.
2. R.D. Doherty, D.A. Hughes, F.J. Humphreys, J.J. Jonas, D.J. Jensen, M.E. Kassner, T.R. McNelley, H.J. McQueen, and A.D. Rollet, Current issues in recrystallization: A review. Mater. Sci. Eng. A, 1997, vol. 238, pp. 219-274.
3. J.X. Lv, J.H. Zheng, V.A. Yardley, Z.S. Shi, and J.G. Lin, A Review of Microstructural Evolution and Modelling of Aluminium Alloys under Hot Forming Conditions. Metals, 2020, vol. 10, pp. 1516.
4. H. Mirzadeh, Grain refinement of magnesium alloys by dynamic recrystallization (DRX): A review. J. Mater. Res. Technol., 2023, vol. 25, pp. 7050-7077.
5. H.K. Zhang, H. Xiao, X.W. Fang, Q. Zhang, R.E. Logé, and K. Huang, A critical assessment of experimental investigation of dynamic recrystallization of metallic materials. Mater. Des., 2020, vol. 193, pp. 108873.

6. T. Sakai, and J.J. Jonas, Dynamic recrystallization: Mechanical and microstructural considerations. Acta Metall., 1984, vol. 32, pp. 189-209.
7. H.W. Son, J.C. Lee, C.H. Cho, and S.K. Hyun, Effect of Mg content on the dislocation characteristics and discontinuous dynamic recrystallization during the hot deformation of Al-Mg alloy. J. Alloys Compd., 2021, vol. 887, pp. 161397.
8. H. Li, Y.C. Huang, and Y. Liu, Dynamic recrystallization mechanisms of as-forged Al-Zn-Mg-(Cu) aluminum alloy during hot compression deformation. Mater. Sci. Eng. A, 2023, vol. 878, pp. 145236.
9. D. Ponge, M. Bredehöft, and G. Gottstein, Dynamic recrystallization in high purity aluminum. Scr. Mater., 1997, vol. 37, pp. 1769-1775.
10. S. Gourdet, and F. Montheillet, An experimental study of the recrystallization mechanism during hot deformation of aluminium. Mater. Sci. Eng. A, 2000, vol. 283, pp. 274-288.
11. R. Kaibyshev, K. Shipilova, F. Musin, and Y. Motohashi, Continuous dynamic recrystallization in an Al-Li-Mg-Sc alloy during equal-channel angular extrusion. Mater. Sci. Eng. A, 2005, vol. 396, pp. 341-351.
12. T. Sakai, H. Miura, A. Goloborodko, and O. Sitdikov, Continuous dynamic recrystallization during the transient severe deformation of aluminum alloy 7475. Acta Mater., 2009, vol. 57, pp. 153-162.
13. J.S. Miao, S. Sutton, and A.A. Luo. Deformation microstructure and thermomechanical processing maps of homogenized AA2070 aluminum alloy. Mater. Sci. Eng. A, 2022, vol. 834, pp. 142619.
14. H.J. McQueen, O. Knustad, N. Ryum, and J.K. Solberg. Microstructural evolution in Al deformed to strains of 60 at 400°C. Scr. Mater., 1985, vol.19, pp. 73-78.
15. W. Blum, Q. Zhu, R. Merkel, and H.J. McQueen. Geometric dynamic recrystallization in hot torsion of Al-5Mg-0.6Mn (AA5083). Mater. Sci. Eng., A, 1996, vol. 205, pp. 23-30.
16. C. Chovet, S. Gourdet, and F. Montheillet. Modelling the transition from discontinuous to continuous dynamic recrystallization with decreasing purity in aluminium. Mater. Trans., JIM, 2000, vol.41, pp. 109-112.
17. B. Yang, M. Gao, Y. Wang, and R. Guan. Dynamic recrystallization behavior and mechanical properties response of rheo-extruded Al-Mg alloys with various Mg contents. Mater. Sci. Eng., A, 2022, vol. 849, pp. 143450.
18. H. Jazaeri, and F.J. Humphreys. The transition from discontinuous to continuous recrystallization in some aluminium alloys: I-the deformed state. Acta Mater., 2004, vol. 52, pp. 3239-3250.

19. G.A. Henshall, M.E. Kassner, and H.J. McQueen. Dynamic restoration mechanisms in Al-5.8 At. Pct Mg deformed to large strains in the solute drag regime. Metall. Trans. A, 1992, vol. 23, pp. 881-889.
20. J.C. Li, X.D. Wu, L.F. Cao, B. Liao, Y.C. Wang, and Q. Liu. Hot deformation and dynamic recrystallization in Al-Mg-Si alloy. Mater. Charact., 2021, vol. 173, pp. 110976.
21. M.R. Rokni, A. Zarei-Hanzaki, A.A. Roostaei, and H.R. Abedi. An investigation into the hot deformation characteristics of 7075 aluminum alloy. Mater. Des., 2011, vol. 32, pp. 2339-2344.
22. J.W. Lee, K.T. Son, T.K. Jung, Y.O. Yoon, S.K. Kim, H.J. Choi, and S.K. Hyun. Continuous dynamic recrystallization behavior and kinetics of Al-Mg-Si alloy modified with CaO-added Mg. Mater. Sci. Eng., A, 2016, vol. 673, pp. 648-659.
23. B. Liao, X.D. Wu, L.F. Cao, G.J. Huang, Z.A. Wang, and Q. Liu. The microstructural evolution of aluminum alloy 7055 manufactured by hot thermo-mechanical process. J. Alloys Compd., 2019, vol. 796, pp. 103-110.
24. J.J. Zhang, Y.P. Yi, S.Q. Huang, X.C. Mao, H.L. He, J.G. Tang, W.F. Guo, and F. Dong. Dynamic recrystallization mechanisms of 2195 aluminum alloy during medium/high temperature compression deformation. Mater. Sci. Eng., A, 2021, vol. 804, pp. 140650.
25. R. Kaibyshev, and S. Malopheyev. Mechanisms of dynamic recrystallization in aluminum alloys. Mater. Sci. Forum, 2014, vol. 794, pp. 784-789.
26. D. Canelo-Yubero, Z. Kovács, J.F. Thierry Simonet Fotso, D. Tolnai, N. Schell, I. Groma, and C. Poletti. In-situ characterization of continuous dynamic recrystallization during hot torsion of an Al-Si-Mg alloy. J. Alloys Compd., 2020, vol. 822, pp. 153282.
27. Q. Li, J. Ning, L. Chen, J. Hu, and Y. Liu. The mechanical response and microstructural evolution of 2195 Al–Li alloy during hot tensile deformation. J. Alloys Compd., 2020, vol. 848, pp. 156515.
28. H. Yamagata, Y. Ohuchida, N. Saito, and M. Otsuka. Nucleation of new grains during discontinuous dynamic recrystallization of 99.998 mass% Aluminum at 453K. Scr. Mater., 2001, vol. 45, pp. 1055-1061.
29. T. Sheppard, and M.G. Tutcher. Development of duplex deformation substructure during extrusion of a commercial Al-5Mg-0.8Mn alloy. Met. Sci., 1980, vol. 14, pp. 579-590.
30. T. Sakai, A. Belyakov, R. Kaibyshev, H. Miura, and J.J. Jonas. Dynamic and post-dynamic recrystallization under hot, cold and severe plastic deformation conditions. Prog. Mater. Sci., 2014, vol. 60, pp. 130-207.

31. J. Driver. The limitations of continuous dynamic recrystallization (CDRX) of aluminium alloys. Mater. Lett., 2018, vol. 222, pp. 135-137.
32. E. Kozeschnik. Encyclopedia of Materials: Metals and Alloys, 2022, vol. 4, Elsevier, Oxford, pp. 521-526.
33. K. Huang, and R.E. Logé. A review of dynamic recrystallization phenomena in metallic materials. Mater. Design, 2016, vol. 111, pp. 548-574.
34. H. Zhang, K. Zhang, H. Zhou, Z. Lu, C. Zhao, and X. Yang. Effect of strain rate on microstructure evolution of a nickel-based superalloy during hot deformation. Mater. Des., 2015, vol. 80, pp. 51-62.
35. E.I. Poliak, and J.J. Jonas. Critical strain for dynamic recrystallization in variable strain rate hot deformation. ISIJ Int., 2003, vol. 43, pp. 692-700.
36. N.D. Ryan, and H.J. McQueen. Dynamic softening mechanisms in 304 austenitic stainless steel. Can. Metall. Q., 1990, vol. 29, pp.147-162.
37. O.D. Sherby, R.H. Klundt, and A.K. Miller. Flow stress, subgrain size, and subgrain stability at elevated temperature. Metall. Trans. A, 1977, vol. 8, pp. 843-850.
38. E.I. Poliak, and J.J. Jonas. A one-parameter approach to determining the critical conditions for the initiation of dynamic recrystallization. Acta Mater., 1996, vol. 44, pp. 127-136.
39. A. Cingara, and H.J. McQueen. New formula for calculating flow curves from high temperature constitutive data for 300 austenitic steels. J. Mater. Process. Technol., 1992, vol. 36, pp. 31-42.
40. R.E. Smallman, and R.J. Bishop. Modern physical metallurgy and materials engineering, 1999, Butterworth-Heinemann.
41. Y.C. Lin, M.S. Chen, and J. Zhong. Prediction of 42CrMo steel flow stress at high temperature and strain rate. Mech. Res. Commun., 2008, vol. 35, pp. 142-150.
42. S. Zaefferer, T. Baudin, and R. Penelle. A study on the formation mechanisms of the cube recrystallization texture in cold rolled Fe-36% Ni alloys. Acta Mater., 2001, vol. 49, pp. 1105-1122.
43. Q.Y. Yang, Z.H. Deng, Z.Q. Zhang, Q. Liu, Z.H. Jia and G.J. Huang. Effects of strain rate on flow stress behavior and dynamic recrystallization mechanism of Al-Zn-Mg-Cu aluminum alloy during hot deformation. Mater. Sci. Eng., A, 2016, vol. 662, pp. 204-213.
44. C.S. Zhang, M.F. Liu, Z.J. Meng, Q.Y. Zhang, G.Q. Zhao, L. Chen, H. Zhang, and J. Wang. Microstructure evolution and precipitation characteristics of spray-formed and subsequently extruded 2195 Al-Li alloy plate during solution and aging process. J. Mater. Process. Technol., 2020, vol. 283, pp. 116718.

45. H. Gao, Y. Huang, W.D. Nix, and J.W. Hutchinson. Mechanism based strain gradient plasticity I. Theory. J. Mech. Phys. Solids, 1999, vol. 47, pp. 1239-1263.
46. Y. Zhang, A. Godfrey, and D.J. Jensen. Local boundary migration during recrystallization in pure aluminium. Scr. Mater., 2011, vol.64, pp. 331-334.
47. C. Poletti, M. Rodriguez-Hortalá, M. Hauser, and C. Sommitsch. Microstructure development in hot deformed AA6082. Mater. Sci. Eng., A, 2011, vol. 528, pp. 2423-2430.
48. C. Sellars, and Q. Zhu. Microstructural modelling of aluminium alloys during thermomechanical processing. Mater. Sci. Eng. A, 2000, vol. 280, pp. 1-7.

Paper II

Subgrain Size Modeling and Substructure Evolution in an AA1050 Aluminum Alloy during High-Temperature Compression

Qi Yang, Tomasz Wojcik and Ernst Kozeschnik

Materials
Volume 17, Year 2024, Pages 4385.

Subgrain Size Modeling and Substructure Evolution in an AA1050 Aluminum Alloy during High-Temperature Compression

Qi Yang, Tomasz Wojcik, and Ernst Kozeschnik*

Institute of Materials Science and Technology, TU Wien, Getreidemarkt 9, 1060 Vienna, Austria
*Correspondence: ernst.kozeschnik@tuwien.ac.at

Abstract: For materials with high stacking fault energy (SFE), such as aluminum alloys, dynamic recovery (DRV) and dynamic recrystallization (DRX) are essential softening mechanisms during plastic deformation, which lead to the continuous generation and refinement of newborn subgrains (2° < misorientation angle < 15°). The present work investigates the influence of compression parameters on the evolution of the substructures for a 1050 aluminum alloy at elevated temperatures. The alloy microstructure was investigated under deformation temperatures ranging from 300 °C to 500 °C and strain rates from 0.01 to 0.1 s^{-1}, respectively. A well-defined substructure and subsequent subgrain refinement provided indication of the evolution laws of the substructure under high-temperature compression. Corresponding experimental data on the average subgrain size under various compression conditions were obtained. Two different independent average subgrain size evolution models (empirical and substructure-based) were used and applied with several internal state variables. The substructure model employed physical variables to simulate subgrain refinement and thermal coarsening during deformation, incorporating a corresponding dislocation density evolution model. The correlation coefficient (R) and root mean square error ($RMSE$) of the substructure-based model were calculated to be 0.98 and 5.7%, respectively. These models can provide good estimates of the average subgrain size, with both predictions and experiments reproducing the expected subgrain size evolution using physically meaningful variables during continuous deformation.

Keywords: substructure evolution; subgrain size model; high-temperature compression; aluminum alloy

1. Introduction

Aluminum alloys are widely used in automotive, aerospace, and other branches of industry due to their low mass and mechanical features. The hot forming of Al alloys is a complex

metallurgical process that involves work hardening (WH), dynamic recovery (DRV), static recovery (SRV), dynamic recrystallization (DRX), grain growth, and other phenomena [1-3].

For materials with high stacking fault energy (SFE), such as Al alloys, DRV and continuous dynamic recrystallization (CDRX) [4-8] are the prominent softening mechanisms during hot forming, and they are observed in different series of Al alloys. Recent research [9-11] has indicated that low-angle subgrains (2° < misorientation angle < 15°) develop through the absorption of new mobile dislocations, subsequently transforming into high-angle grain boundaries (HAGBs) with misorientation angles > 15°. This process results in a well-defined substructure and subsequent DRX during high-temperature deformation.

The understanding and modeling of low-angle subgrain evolution are recognized as the key for describing the mechanisms of DRV and DRX during plastic deformation. Huang et al. [12] and Sakai et al. [13] reviewed the microstructural evolution and mechanism of Al alloy during deformation. Zhang et al. [14], Ding et al. [15], and Li et al. [16] studied the deformation behavior and DRX of various Al alloys, such as 2195 Al alloy and 5083 Al alloy. Current research has focused more on the CDRX process for Al alloy, which has been observed in the hot deformation or severe plastic deformation (SPD) processes of Al-Mg [17], Al-Li [18], Al-Cu [19], and other Al alloys. There are only a few studies that have analyzed and investigated substructural changes under varying compression conditions.

The majority of existing models [20-23] rely on empirical relationships to quantify parameters such as flow stress and steady-state subgrain size with the Zener-Hollomon parameter (Z). Material models of the subgrain size evolution of high-SFE alloy are scarcer. Nes et al. [24, 25] as well as Duan and Sheppard [26-28] have developed mathematical models to describe the substructure evolution and the recrystallization kinetics during aluminum rolling and extrusion, respectively. In subsequent work, Marthinsen and Nes [29] considered the influence of grains, particles, and dispersoids on the subgrain size model. Gourdet and Montheillet [30] (GM) introduced a subgrain size evolution model as part of the CDRX model framework, which considers the misorientation evolution caused by subgrain rotation and the migration of HAGBs. Furthermore, some extended subgrain models [31-33] have also been developed recently on the basis of the GM model within the CDRX framework.

Most of the subgrain models developed in recent years rely on translating subgrain size δ_{sub} into volumetric boundary density S_{sub}, defined as $\delta_{\mathrm{sub}} = 2/S_{\mathrm{sub}}$. [30-33]. This approach lacks physical interpretability and is challenging to verify experimentally. Currently, subgrain size can be measured experimentally using electron backscatter diffraction (EBSD), allowing for the investigation of its effects on material properties. An independent model of average

subgrain size, incorporating physically meaningful variables, is applied based on experimental values. In this study, an AA1050 pure Al alloy was selected to minimize the influence of solute atoms and precipitated particles as defects/pinning position on the evolution of low-angle subgrain boundaries (or dislocation cells).

In this study, the influence of deformation parameters on the evolution of the substructures for an AA1050 Al alloy was investigated under high-temperature compression, experimentally obtaining the average grain size under various conditions. The occurrence of a well-defined substructure and subsequent low-angle subgrain refinement were analyzed under different strains, temperatures, and strain rates. The mechanisms driving substructure evolution were evaluated by analyzing the average subgrain size, misorientation angles, and the distribution of subgrains. Subsequently, an empirical model and an advanced substructure-based model of average subgrain size were established with several internal state variables. These models were validated using a detailed substructural investigation, and model input parameters are herein described in detail as well as their dependencies.

2. Model Description

2.1. Empirical Average Subgrain Size Model

During the hot forming of Al alloys, DRV serves as the main recovery process, resulting in the formation of well-defined substructures. Recent studies have indicated that the average subgrain size gradually attains a "saturation value" δ_s, which becomes invariant with respect to strain during deformation [1,21-24,34]. This saturated subgrain size is balanced during DRV after the alloy microstructure reaches steady state, and it depends on the temperature and strain rate, as in [21].

$$\delta_s = [\alpha_1 + \beta_1 \ln\left(\dot{\varepsilon}\exp(\frac{Q}{RT})\right)]^{-1}, \quad (1)$$

where δ_s is the saturated average subgrain size, α_1 and β_1 are material constants, $\dot{\varepsilon}$ is the strain rate, Q is the deformation activation energy, R is the gas constant, and T is the absolute deformation temperature. In the present work, the values of α_1 and β_1 are derived from the EBSD experimental data, with the average value of the coefficients being $\alpha_1 = 0.015$ and $\beta_1 = -0.15$.

The activation energy Q is a key material parameter that indicates the resistance of the deformation. In the present work, the activation energy Q is 142 kJ.mol^{-1}, close to that for pure Al alloy [35].

The empirical model describes the process of subgrain evolution under deformation based

on the initial subgrain size δ_0, which gradually decreases until a steady-state microstructure is achieved. The relationship between the average subgrain size and the saturated subgrain size is represented by the following empirical formulation [36]:

$$\begin{cases} \delta_{\mathrm{sub}} = \delta_0 - (\delta_0 - \delta_{\mathrm{s}})\left[1 - \exp\left(-\alpha_2(\varepsilon_{\mathrm{d}} - \varepsilon_{\mathrm{c}})^{\beta_2}\right)\right], & \varepsilon_{\mathrm{d}} < \varepsilon_{\mathrm{s}} \\ \delta_{\mathrm{sub}} = \delta_{\mathrm{s}}, & \varepsilon_{\mathrm{d}} > \varepsilon_{\mathrm{s}} \end{cases}, \tag{2}$$

where δ_{sub} is the average subgrain size, δ_0 is the initial average subgrain size, α_2 and β_2 are material constants, ε_{d} is the strain during deformation, ε_{c} is the critical strain up to which subgrains can be distinguished, and ε_{s} is the strain where the subgrain size starts to become saturated.

To determine the values of α_2 and β_2, Equation (2) can be rewritten in double natural logarithm form:

$$\ln\left(-\ln\left(1 - \frac{\delta_0 - \delta_{\mathrm{sub}}}{\delta_0 - \delta_{\mathrm{s}}}\right)\right) = \ln\alpha_2 + \beta_2 \ln\left((\varepsilon_{\mathrm{d}} - \varepsilon_{\mathrm{c}})\right), \tag{3}$$

In the present work, the material constants α_2 and β_2 are derived from the mean values of the slopes and intercepts as α_1 = 5.00 and β_1 = 1.15.

2.2. Substructure-Based Model

The plastic deformation of Al alloys generally occurs in three key stages [1,12,13,25]: (1) initial stage: increasing dislocation activity, whereby cells/subgrain boundaries are formed; (2) subgrain refinement: subgrains continue to form and refine; and (3) thermal coarsening of subgrain: involves the thermally induced coarsening of subgrains during deformation, resulting in an increase in subgrain size.

The substructure-based model of average subgrain size describes the evolution of subgrains using physical internal state variables. The first part of the model is to simulate the subgrain refinement as the deformation progresses, incorporating the effects of various deformation parameters. To better represent the subgrain refinement process during high-temperature compression, a substructure-based model was developed as follows [25, 29]:

$$\mathrm{d}\delta_{\mathrm{sub}}^{-} = -f_{\mathrm{r}} \frac{\sqrt{3}\dot{\varepsilon} b^{1/2}}{\bar{\theta}_{\mathrm{s}}^{\,3/2} \bar{\delta}_{\mathrm{s}}^{\,2}} \delta_{\mathrm{sub}}^{\,v_1} dt, \tag{4}$$

where δ_{sub} is the average subgrain size during deformation, b is the Burger's vector, $\bar{\theta}_{\mathrm{s}}$ is the average subgrain boundary misorientation in the steady-state stage, v_1 is a material coefficient that controls the subgrain refinement rate and is set to 1 in this work, f_{r} is a material coefficient related to subgrain refinement, and $\bar{\delta}_{\mathrm{s}}$ is the average subgrain size of steady-state stage, expressed as follows:

$$\bar{\delta}_{\mathrm{s}} = \frac{1}{3}\left(\frac{\bar{\sigma}_{\mathrm{s}}}{c_1 G b}\right)^{-1}, \text{ with } \bar{\sigma}_{\mathrm{s}} = f_1\left[\dot{\varepsilon}\exp\left(\frac{Q}{RT}\right)\right]^{f_2} \tag{5}$$

where $\bar{\sigma}_s$ is the steady-state flow stress, G is the shear modulus, f_1 and f_2 are material constants, and c_1 is a material coefficient related to the flow stress.

In the process of high-temperature compression, the occurrence of subgrain refinement is dynamically counteracted by thermally induced coarsening. This coarsening occurs by mechanisms such as subgrain boundary migration, subgrain rotation, and the evolution of dislocation density, resulting in the movement of subgrain boundaries. In the present work, a coarsening model was applied, where the subgrain size is related to the evolution of subgrain migration and dislocation density, as follows [25]:

$$d\delta_{sub}^{+} = f_c \nu_D b^2 \sqrt{\rho} \left[\exp\left(-\frac{U_s + PV_a}{k_B T}\right)\right] dt, \tag{6}$$

where ν_D is the Debye frequency, ρ is the dislocation density, P is the driving force on the subgrain boundary, V_a is the average activation volume of subgrain boundaries, k_B is the Boltzmann constant, U_s is the activation energy for self-diffusion in Al with unit J.atom^{-1}, and f_c is a material coefficient related to subgrain coarsening.

For the two material coefficients, the coefficient f_r exhibits sensitivity to both deformation temperature and strain rate, making it a critical factor in controlling the trend and rate of subgrain refinement under various deformation conditions. Similarly, the material coefficient f_c is also dependent on temperature and strain rate. Therefore, the coefficients can be formulated as given below:

$$f_r = f_3[\dot{\varepsilon}\exp(\frac{Q}{RT})]^{f_4}, \text{ and } f_c = f_5[\dot{\varepsilon}\exp(\frac{Q}{RT})]^{f_6}, \tag{7}$$

where f_3, f_4, f_5, and f_6 are material constants.

The driving force for subgrain boundary migration [37] is taken as $P = 4\gamma/\delta_{sub}$, where γ is the subgrain boundary energy. The average activation volume of subgrain boundary [25] can be expressed as $V_a = b^3/\theta_{sub}$, where θ_{sub} is the average subgrain boundary misorientation angle.

The dislocation density model incorporates several key mechanisms affecting the dislocation evolution, including dislocation generation due to work hardening (WH) and reduction in dislocation density through DRV and static recovery (SRV) with dislocation climbing and gliding, as follows [38-40]:

$$d\rho/dt = \frac{M\sqrt{\rho}}{Ab}\dot{\varepsilon} - 2BM\rho\frac{d_{crit}}{b}\dot{\varepsilon} - 2CD_d\frac{Gb^3}{k_B T}\left(\rho^2 - {\rho_{eq}}^2\right) - 2f_H\nu_H\rho\frac{1}{\delta_{sub}}, \tag{8}$$

where A, B, and C are material-dependent coefficients; M is the Taylor factor; d_{crit} is the critical distance of dislocation annihilation; D_d is the diffusion coefficient along dislocation pipes; ρ_{eq} is the equilibrium dislocation density; f_H is the fraction of HAGBs; and ν_H is the

migration rate of HAGBs.

The last term in Equation (8) accounts for the reduction in the average internal dislocation density accompanying the migration of HAGBs. The migration rate of HAGBs is adopted from Gourdet and Montheillet [30] as follows:

$$v_{\mathrm{H}} = v_0(\frac{\dot{\varepsilon}}{\dot{\varepsilon}_0})^m, \tag{9}$$

where $\dot{\varepsilon}_0$ is the initial strain rate, v_0 is the initial migration rate of HAGBs, and m is a material constant related to the migration rate.

3. Experimental Results

3.1. Material and Experiments

In this study, AA1050 Al alloy billets provided by Neuman Aluminium Austria GmbH (Marktl, Austria) were investigated and subsequently machined into cylinders with a diameter of 5 mm and a height of 10 mm. Single-pass isothermal compression was conducted using a deformation dilatometer DIL 805 A/D from Bähr (Hüllhorst, Germany). The procedures of the compression experiments are shown in Figure 1. Three different forming temperatures within the range of $0.5T_{\mathrm{m}} < T_{\mathrm{def}} < 0.7T_{\mathrm{m}}$ [11] (300 °C, 400 °C, and 500 °C), two different strain rates (0.01 s^{-1} and 0.1 s^{-1}), and four true strains (0.1, 0.3, 0.6, and 0.9) were applied. The true strain values were set within the deformation dilatometer using a built-in calculation formula, defined as $\text{true strain} = \mathrm{Ln}(L/L_0)$, where L_0 is the original length of samples, and L is the current length after deformation. The specimens were quenched with over 100 K/s cooling speed to room temperature immediately after compression.

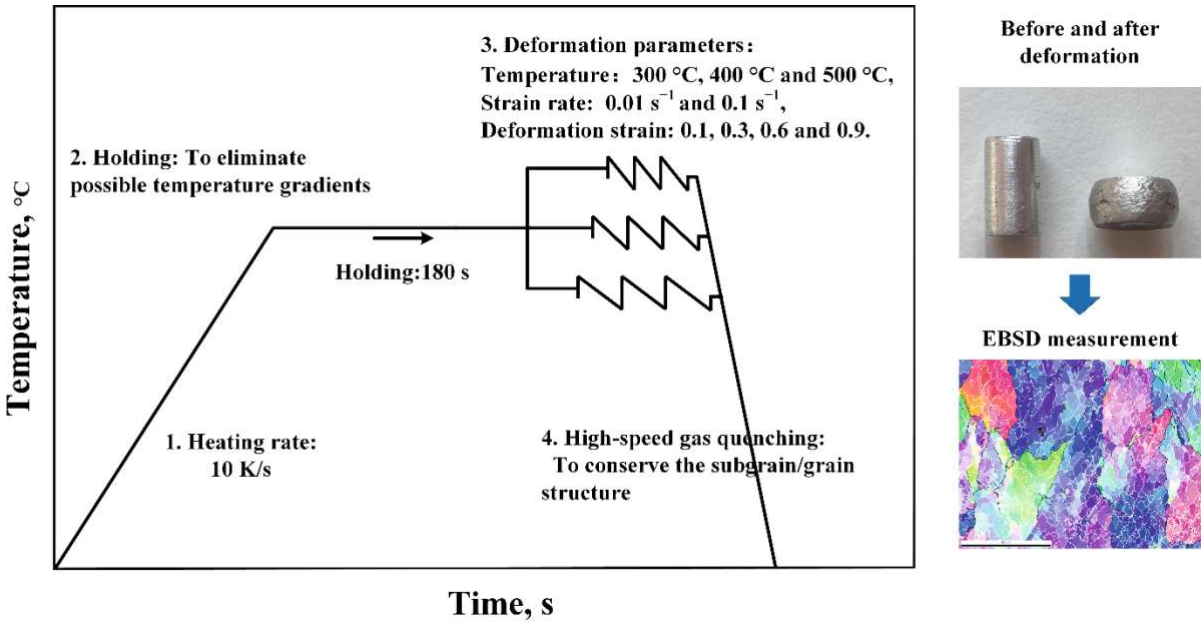

Figure 1. Schematic of the isothermal compression experiments history.

EBSD tests were carried out in a Zeiss Sigma 500 VP (Oberkochen, DE) high-resolution scanning electron microscope with an EDAX detector with an accelerating voltage of 20 kV and a step size of 0.5 μm. The data processing of EBSD results was carried out with the EDAX OIM Analysis8 software ((v8, EDAX Inc., Mahwah, NJ, USA). The post-processing procedure to distinguish most of the subgrains consisted of the following: (1) the standard "clean up" algorithm; (2) construction of the grains with grain tolerance angle 1.0, which enabled the software to identify most subgrains; (3) setting up a confidence index > 0.1 filter in the partition properties dialog to hide all mis-indexed points; (4) performing a confidence index standardization (CIS) to allow points from overlapping patterns at grain boundaries to be maintained in the map; (5) acquiring distinct grain color maps and subgrain size distributions, and areas containing significant errors or unresolved regions were excluded from the analysis.

3.2. Substructure Evolution

Figure 2a-c show the microstructure maps after compression at temperatures of 300 °C. Low-angle subgrain boundaries and HAGBs are shown as white and black lines, respectively. Under conditions of low strain (Figure 2a), the generation of initial subgrains was observed within the parent grains, characterized by an irregular morphology. In materials with high SFE, dislocations rearrangement and annihilation occurred through DRV, resulting in the formation of subgrain boundaries within the pancaked parent grains [12-13, 21-22]. It is noteworthy that the initial subgrain boundaries were formed without a nucleation process, consistent with the conclusions reported by Huang et al. [12] and Sakai et al. [13].

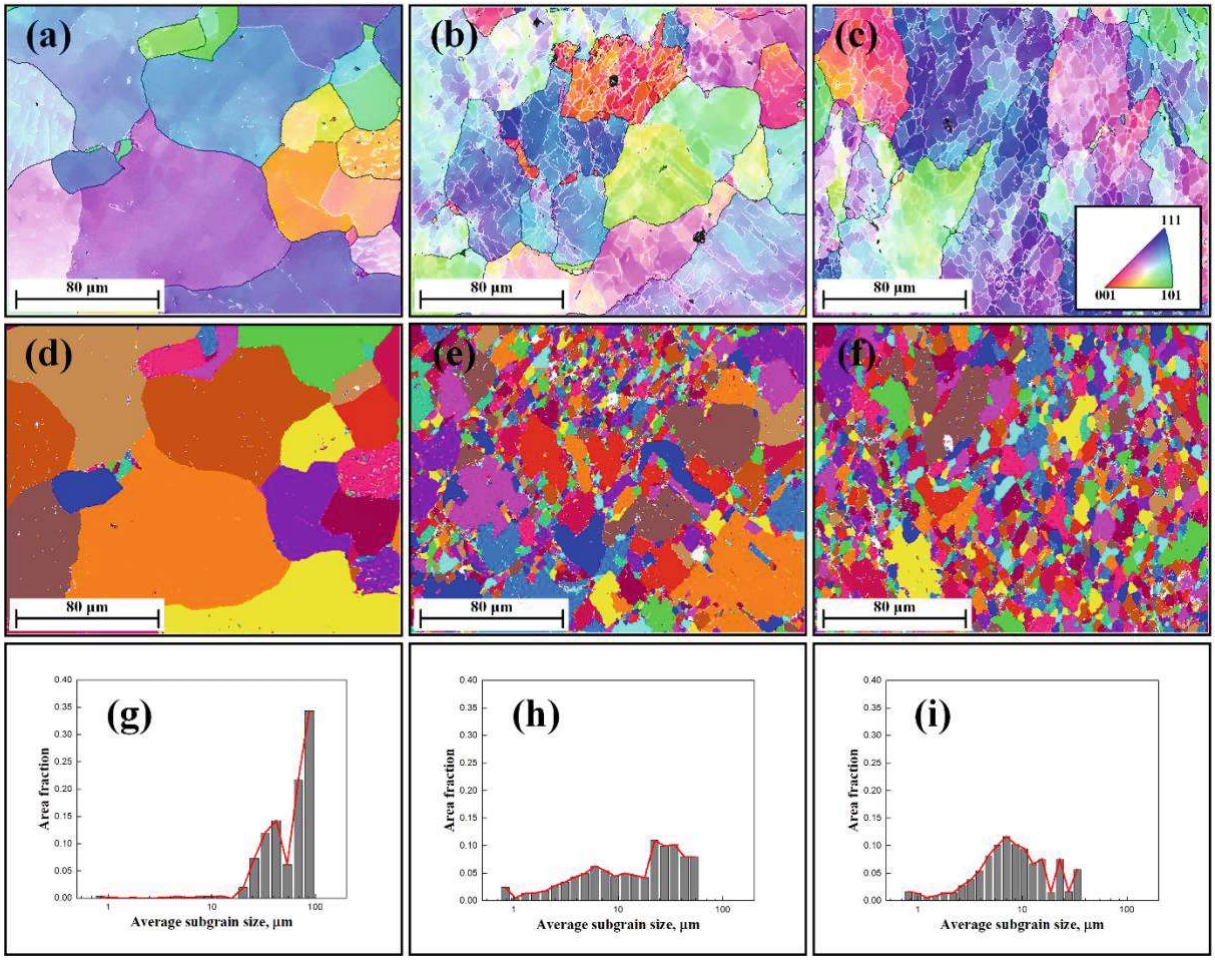

Figure 2. EBSD images of 1050 Al alloy deformed to a different strain at a temperature of 300 °C and a strain rate of 0.1 s^{-1}: (a-c) inverse pole figure (IPF) maps of the specimens with strain 0.1, 0.3, and 0.6; (d-f) corresponding unique grain color maps; and (g-i) subgrain size distribution maps.

As deformation progressed (Figure 2b), an increased formation of subgrain boundaries was observed due to the continued accumulation of dislocations. Concurrently, the generation of some unclosed subgrains within the original grains was observed, which is also shown by the corresponding unique grain color maps depicted in Figure 2e. Additionally, Figure 2c reveals the presence of more newborn subgrains with an equiaxed morphology, suggesting subgrain rotation and an increase in the misorientation angle of boundaries. This continuous formation of new subgrain boundaries resulted in a substantial decrease in the average subgrain size.

The corresponding unique grain color maps and subgrain size distribution maps at 300 °C are presented in Figure 2d-i. It is clear that the average subgrain size (area fraction) exhibits a relatively random distribution. The average subgrain size of the specimens progressively decreased with increasing strain, decreasing deformation temperature, and increasing strain rate. Consequently, the continuous formation of subgrain boundaries was responsible for the

decrease in the subgrain size, which was also accompanied by an increase in wall dislocation density and misorientation angle, serving as a typical identification of DRV and, subsequently, the CDRX phenomenon. [1, 12-13] The average subgrain size, calculated from the EBSD data under different conditions, is summarized in Table 1.

Table I. Measured average subgrain size under different deformation conditions

Average subgrain size (μm)	**Temperature (°C)**	**Strain rate (s^{-1})**	**strain 0.1**	**strain 0.3**	**strain 0.6**	**strain 0.9**
Average subgrain size	300	0.1	63	21	11	1.7
	400	0.1	71	33	21	3.5
	500	0.1	65	37	25	11
	500	0.01	83	43	28	19

Different from Figure 2, the presence of subgrain coarsening became evident when subjected to deformation at high temperatures, as shown in Figure 3b,c. During the DRV process, elevated temperatures enhanced their mobility, facilitating the migration of subgrain boundaries and thereby leading to an increase in subgrain size. [25, 29] As deformation proceeded, the primary mechanism remained the continued generation and refinement of finer subgrains, which was manifested in a significant reduction in subgrain size, as shown in Figure 3d-i and Table 1. This demonstrates that some low-angle sub-boundaries disappeared, while others expanded due to the continuous growth of subgrains (cells) during hot deformation [41]. Consequently, the increasing of mean subgrain misorientation remained constant even under high strain conditions, in agreement with results from McQueen and Kassner [42].

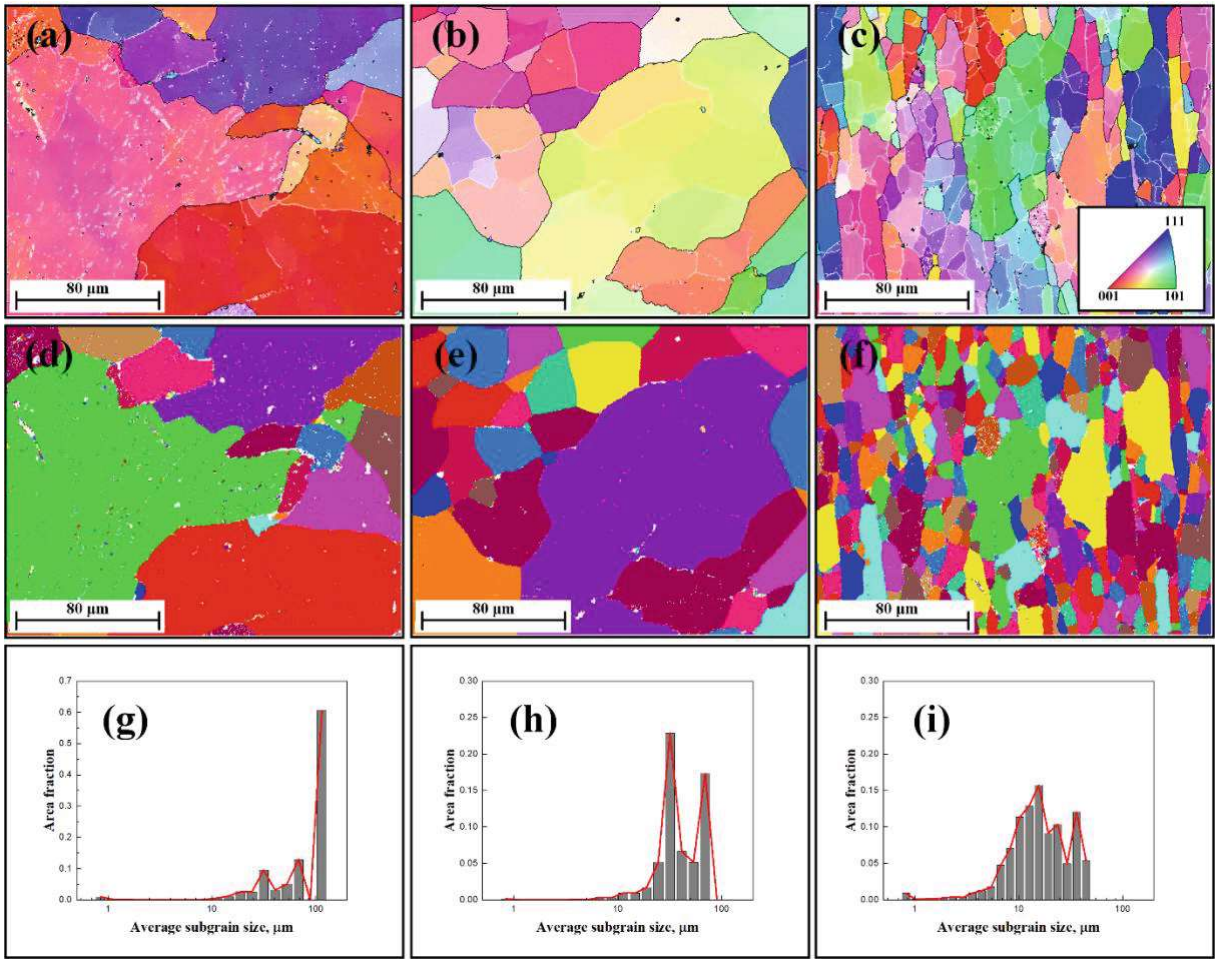

Figure 3. EBSD images of 1050 Al alloy deformed to a different strain with a temperature of 500 °C and a strain rate of 0.1 s^{-1}: (a-c) IPF maps of the specimens deformed with strain 0.1, 0.3, and 0.6; (d-f) corresponding unique grain color maps; and (g-i) subgrain size distribution maps.

The unique grain color maps of specimens deformed to strain 0.9 are illustrated in Figure 4. As expected, the average subgrain size was sensitive to both deformation temperature and strain rate, i.e., the subgrain size increased with increasing temperature or decreasing strain rate.

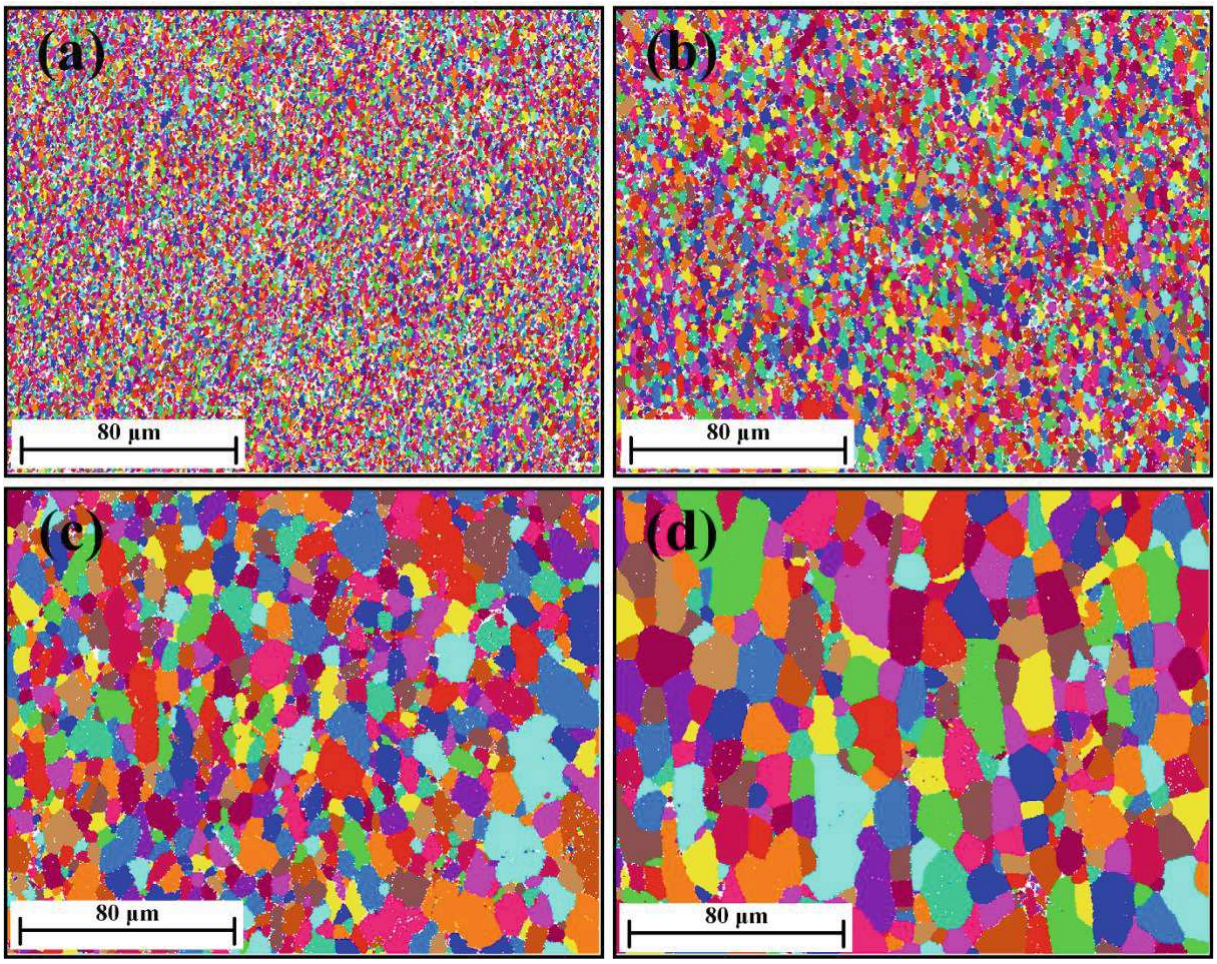

Figure 4. Unique grain color maps of 1050 Al alloy deformed to strain 0.9 at different deformation conditions: (a) 300 °C/0.1 s^{-1}, (b) 400 °C/0.1 s^{-1}, (c) 500 °C/0.1 s^{-1}, and (d) 500 °C/0.01 s^{-1}.

4. Model Application and Discussion

4.1. Model Input Parameters

The initial parameters for the variables are defined as follows: The initial average subgrain size δ_0 was 100 µm. Furthermore, the critical strain ε_c, at which subgrain boundaries become distinguishable within the deformed microstructure, was simplified to zero.

The average subgrain boundary misorientation $\bar{\theta}_s$ of the steady-state stage can be found in the literature as 3°, as suggested by Nes [25]. The value of the material coefficient c_1 was 60, and the calculation of $\bar{\sigma}_s$ was temperature- and strain rate-dependent, such as $\bar{\sigma}_s = 0.6[\dot{\varepsilon}\exp(Q/RT)]^{0.16}$ MPa. The value of subgrain boundary energy γ was selected to be 0.3 $J.m^{-2}$ in this work [37], and the activation energy for self-diffusion in Al [43] was $2 \cdot 10^{-19}$ $J.atom^{-1}$. The list of input parameters for the substructure-based model is summarized in Table 2.

Table II. List of input parameters for substructure-based model

Symbol	Name	Unit	Value	Ref.
ν	Poisson's ratio	-	0.347	[41]
G	Shear modulus	MPa	$29438.4-15.052T$	[42, 43]
b	Burgers vector	m	$2.86\cdot10^{-10}$	[44]
M	Taylor factor	-	3.06	[45]
ν_{D}	Debye frequency	s^{-1}	$1\cdot10^{13}$	[46]
θ_{sub}	Subgrain boundary misorientation	°	5	This work
f_{r}	Material coefficient for subgrain refinement	-	$3.5\cdot10^{9}[\dot{\varepsilon}\exp(Q/RT)]^{-0.23}$	This work
f_{c}	Material coefficient for subgrain coarsening	-	$6000[\dot{\varepsilon}\exp(Q/RT)]^{0.53}$	This work
A	A parameter	-	$2.76\exp(0.0046T)$	This work
B	B parameter	-	2.5	This work
C	C parameter	-	$1\cdot10^{-3}$	This work

The dislocation density evolution parameters A, B, and C were adjusted to the experimental flow curve with the empirical coefficient a in the Taylor relationship, taken as 0.2. The calculation of the critical distance for dislocation annihilation d_{crit} and diffusion coefficient along dislocation pipes D_{d} can be found in the literature as suggested by Sherstnev, Lang, and Kozeschnik [38] and Kreyca and Kozeschnik [39]. The parameters of the HAGBs migration rate were selected for Al alloy as suggested by Gourdet and Montheillet [30].

4.2. Model Validation

This section presents a comparative analysis of the simulated results from the substructure-based model against the experimental data on the evolution of average subgrain size. The experimental measurements of average subgrain size were obtained by EBSD and are detailed in Table 1. The simulations were conducted using MATLAB software version R2016b with given true strain values, employing one single set of input parameters (refer to Section 4.1) applied across all deformation conditions.

Figure 5 presents a comparison between the substructure-based model and the experimental values. At the onset of deformation, a substantial formation of new subgrain boundaries occurred with the progression of compression, resulting in a rapid reduction in the average subgrain size. As the compression progressed, the rate of subgrain size reduction decreased. It is suggested that the subgrain size eventually reaches a “saturation value” at higher strain [1, 21-24, 34]. The analysis indicated that the substructure-based model clearly

reproduced the evolution of the subgrain size. Both the model and the experimental data exhibited the anticipated behavior of the average subgrain size evolution during continuous deformation. Furthermore, this model's ability to simulate subgrain size evolution from different initial average subgrain sizes (50 μm) demonstrates its applicability under various initial subgrain sizes.

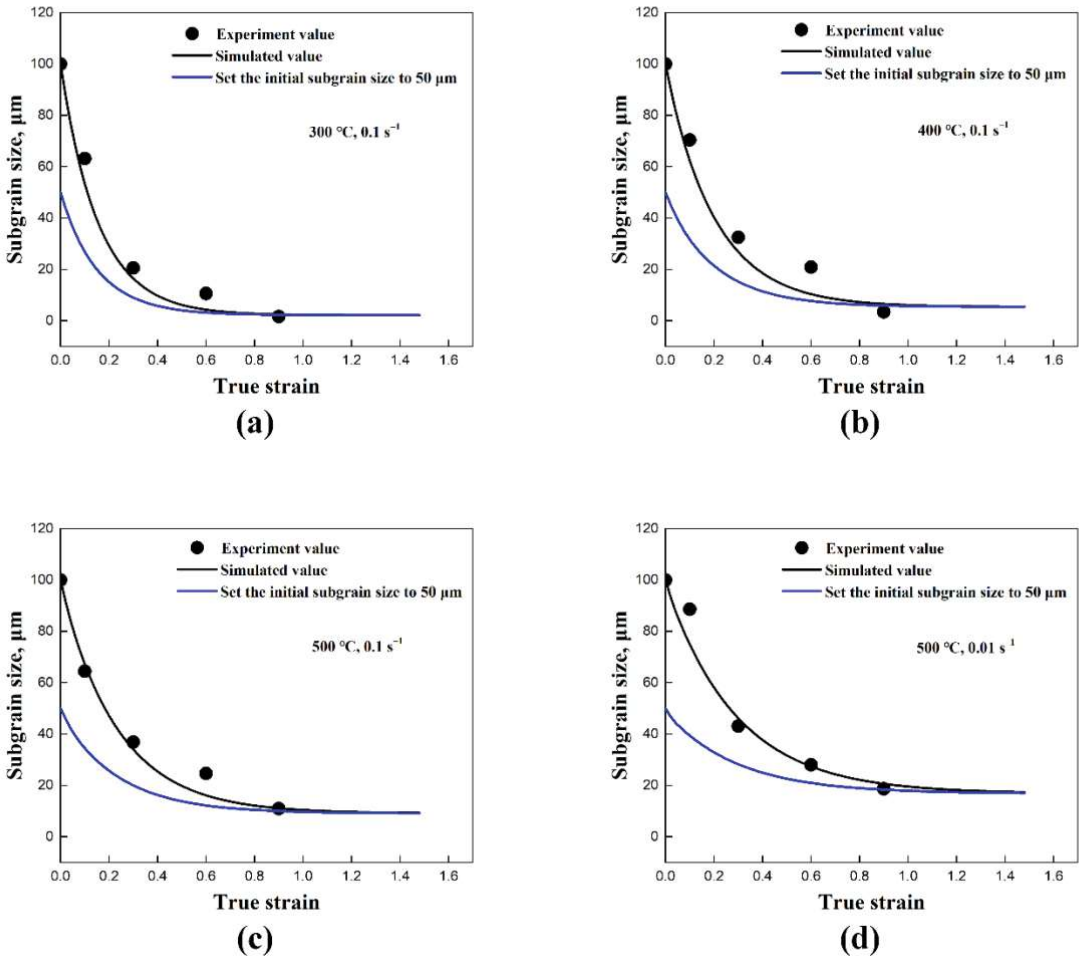

Figure 5. The comparison between the experimental and simulated values of the substructure-based model with different deformation conditions of (a) 300 °C/0.1 s^{-1}, (b) 400 °C/0.1 s^{-1}, (c) 500 °C/0.1 s^{-1}, and (d) 500 °C/0.01 s^{-1}.

To further evaluate the performance of the substructure-based model in the present study, the correlation coefficient (R) and root mean square error ($RMSE$) [50] were evaluated as follows:

$$R = \frac{\sum_{i=1}^{N}(\delta_{ei}-\bar{\delta}_e)(\delta_{ci}-\bar{\delta}_c)}{\sqrt{\sum_{i=1}^{N}(\delta_{ei}-\bar{\delta}_e)^2 \sum_{i=1}^{N}(\delta_{ci}-\bar{\delta}_c)^2}} \tag{10}$$

$$RMSE = \sqrt{\frac{1}{N}\sum_{i=1}^{N}(\delta_{ci}-\delta_{ei})^2} \cdot 100\%, \tag{11}$$

where δ_{ci} represents the calculated subgrain size, δ_{ei} represents the experimental subgrain size,

$\bar{\delta}_c$ is the average calculated subgrain size, $\bar{\delta}_e$ is the average experimental subgrain size, and N is the total number of data points used in this study.

The corresponding error analysis for different deformation conditions is illustrated in Figure 6. The values of R and $RMSE$ are 0.98 and 5.68%, respectively, indicating a good agreement between the experiment and the model.

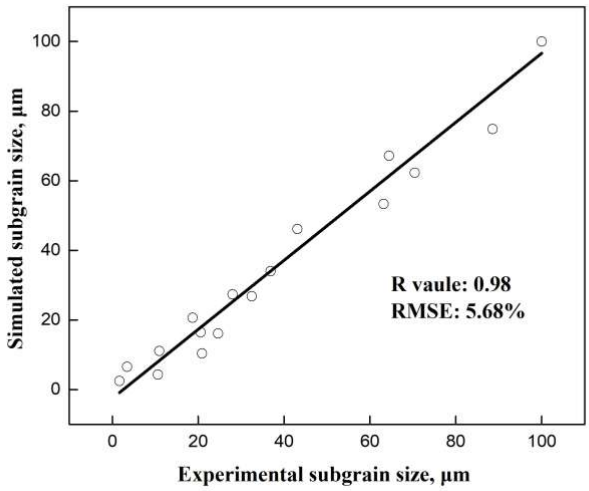

Figure 6. Error analysis for the substructure-based model.

In the substructure-based model, the material coefficients f_r and f_c directly affect the subgrain refinement and coarsening, as illustrated in Figure 7. By accounting for the coarsening term, the refinement of the initial subgrain size is clearly observed, as demonstrated in the microstructures shown in Figures 2 and 3. The subgrain size decreased and gradually reached a steady-state value at larger strains, in agreement with studies from Sellars et al. [22] and Furu et al. [23]. In contrast, when subgrain coarsening was not considered (with the coefficient f_c set to 0), a steady state trend was not achieved, and the subgrain size continued to decrease until it reached zero. Correspondingly, the continuous generation of new subgrain boundaries through dislocation accumulations and rearrangements was observed, in agreement with the results of subgrain/grain boundary migration from Gourdet and Montheillet [30]. In addition, the comparison between the simulated average subgrain size δ_{sub} and experimental δ_{sub} of the traditional empirical model is also shown in Figure 8.

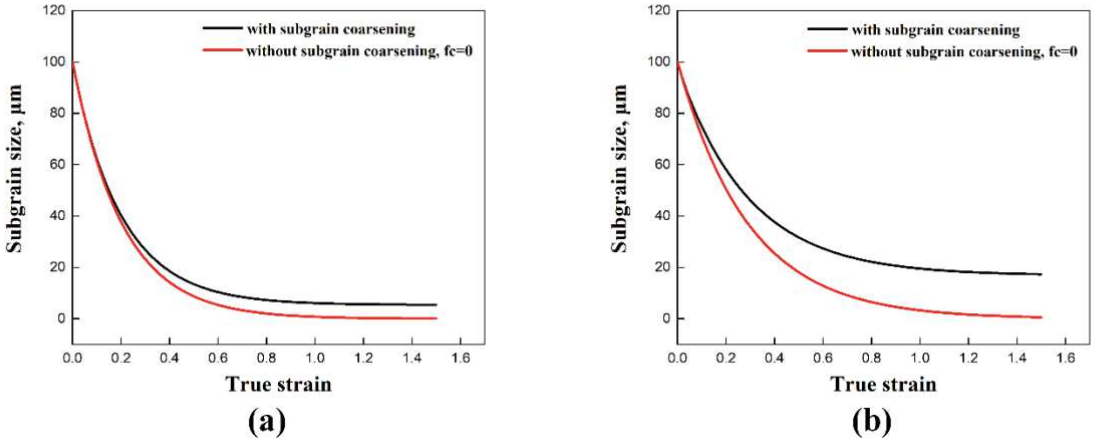

Figure 7. Illustration of the subgrain size evolution with material coefficients related to subgrain refinement and coarsening: (**a**) 400 °C/0.1 s^{-1} and (**b**) 500 °C/0.01 s^{-1}.

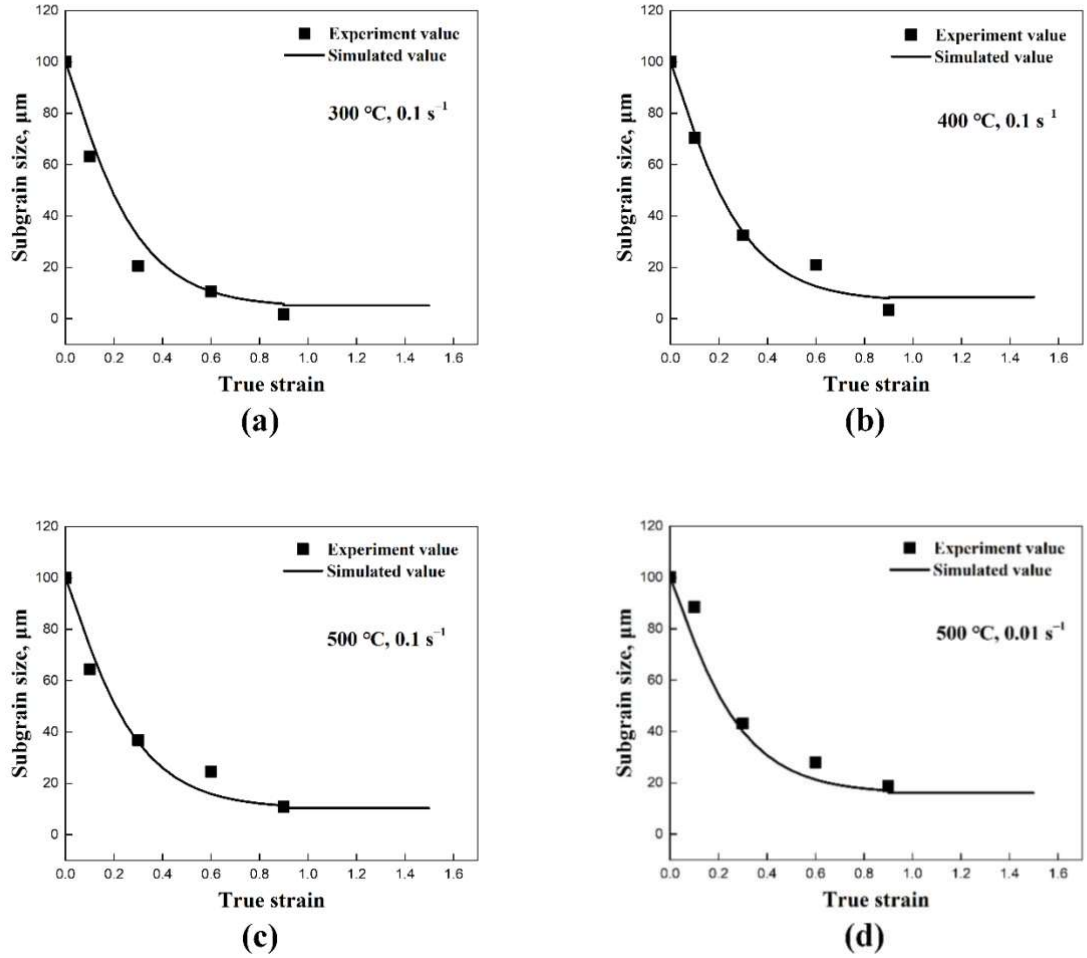

Figure 8. The comparison between the simulated average subgrain size δ_{sub} and experimental δ_{sub} of the empirical model: (a) 300 °C/0.1 s^{-1}, (b) 400 °C/0.1 s^{-1}, (c) 500 °C/0.1 s^{-1}, and (d) 500 °C/0.01 s^{-1}.

4.3. Discussion

The analysis of the deformation structure from the EBSD results confirms that hot deformation leads to the formation of a substructure, where the density of low-angle subgrain boundaries continuously increases (see Figures 2 and 3). Figure 9 represents a detailed grain boundary maps to facilitate a better understanding of substructure generation and development. The formation of cell boundaries, characterized by a high density of dislocations, is constituted by geometrically necessary dislocations (GNDs) that serve to divide the parent grains into subgrains and to maintain the deformation gradients inside the grain as well as the rotation of subgrains. In the deformed microstructure at the interrupted strain of 0.3 (Figure 9a), a high fraction of incomplete sub-boundaries (2° < misorientation < 15°) indicates the formation of a dislocation cell structure. Due to DRV, these incomplete low-angle subgrains (cell walls) continue to form fine and polygonized substructures with ongoing deformation. This mechanism is observed in Al alloys [4,8,19,51], 304-type austenitic stainless steel [52], Ti alloy [53], etc.

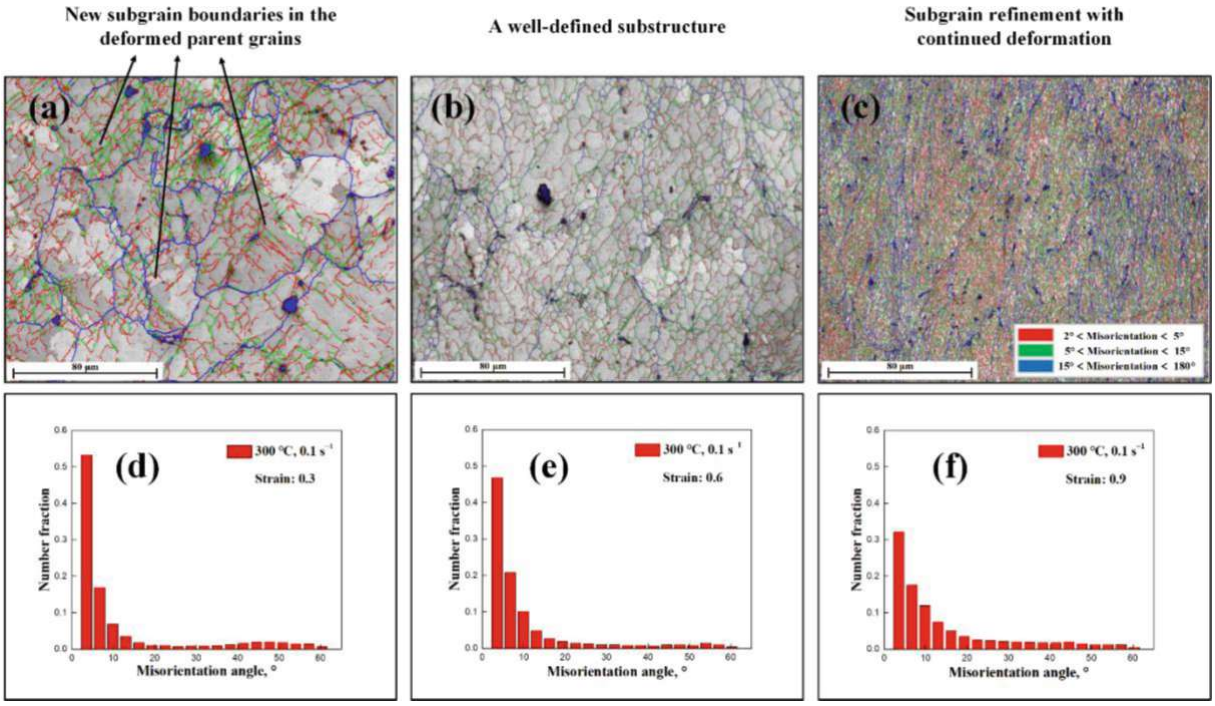

Figure 9. EBSD images of 1050 Al alloy deformed to a different strain at a temperature of 300 °C and a strain rate of 0.1 s^{-1}: (a-c) grain boundary maps of the specimens deformed with strain 0.3, 0.6, and 0.9 and (d-f) corresponding distribution histograms of misorientation angle.

In addition, some researchers [8, 12-13] have introduced other mechanisms for subgrain boundary formation, including micro-shear band assistance and progressive lattice rotation near grain boundaries. At elevated deformation temperatures (see Figure 3), a homogeneous microstructure generally forms, and deformation/micro-shear bands become less prominent

compared to their presence at lower temperatures or cold deformation. The formation of subgrain boundaries facilitated by micro-shear bands is typically observed during the SPD process [13].

Figure 9d-f display the misorientation angle histograms with different strains at 300 °C/0.1 s^{-1}, which indicate a relatively random distribution of misorientation angle. Notably, the average misorientation angle of the specimens increases progressively with strain. This increase is attributed to the transformation of low-angle subgrain boundaries into HAGBs with absorbing mobile dislocations. Such transformations are a feature of the CDRX mechanism, in accordance with the conclusions of other researchers [1, 7-14].

In the substructure-based model, the objective is to correlate the subgrain size evolution with deformation thermo-mechanics, utilizing several internal state variables. Suitable parameters are selected under different strain, strain rate, and temperature to reproduce the observed evolution of average subgrain sizes across the spectrum of conditions (see Section 4.1). The effect of deformation conditions (temperature and strain rate) on the microstructure is shown in Figures 2-4. During deformation at high temperatures, coarse subgrains become evident. Figure 10 shows the simulated average subgrain size predicted by the substructure-based model under different temperatures at a strain rate of 0.1 s^{-1}. An increase in temperature promotes the generation of subgrain boundaries and their mobility, thus promoting the formation of DRX grains [12-13]. A similar observation was reported for the GM model in a 1200-grade aluminum alloy from Gourdet and Montheillet [30], with the differences compared to our present results most likely being due to the differences in the alloy composition. Qualitatively, the results are in reasonable agreement.

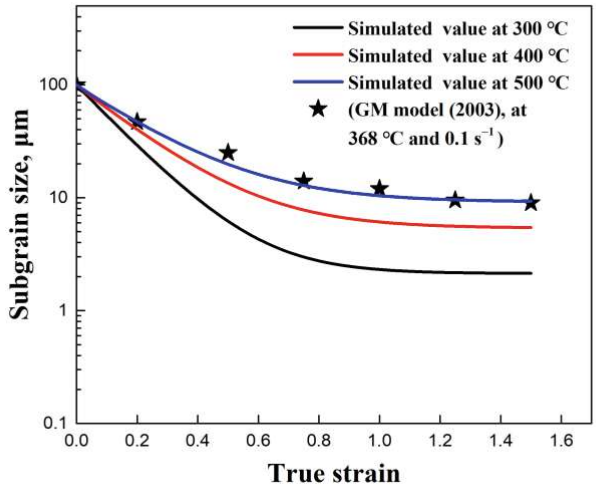

Figure 10. Simulated average subgrain size (δ_{sub}) by substructure-based model with different temperatures at a strain rate 0.1 s^{-1} and comparing the simulated value with the result from Gourdet and Montheillet (GM model) [27].

The simulated results of average subgrain size at other deformation conditions are shown in Figure 11. An increase in strain rate increases the dislocation density, promoting the formation of subgrain boundaries [54-55]. Additionally, the deformation time is elongated at a lower strain rate, facilitating the migration of subgrain boundaries, which in turn increases the subgrain size [11-13]. The results from the experimental subgrain size curves show that the refinement rate is initially high during the early stages of compression but subsequently decelerates. This phenomenon is well simulated by the applied models after the incorporation of thermal subgrain coarsening, in agreement with the results from Nes [25], Gourdet and Montheillet [30], Maizza et al. [10], Sun et al. [31], and Chen et al. [32].

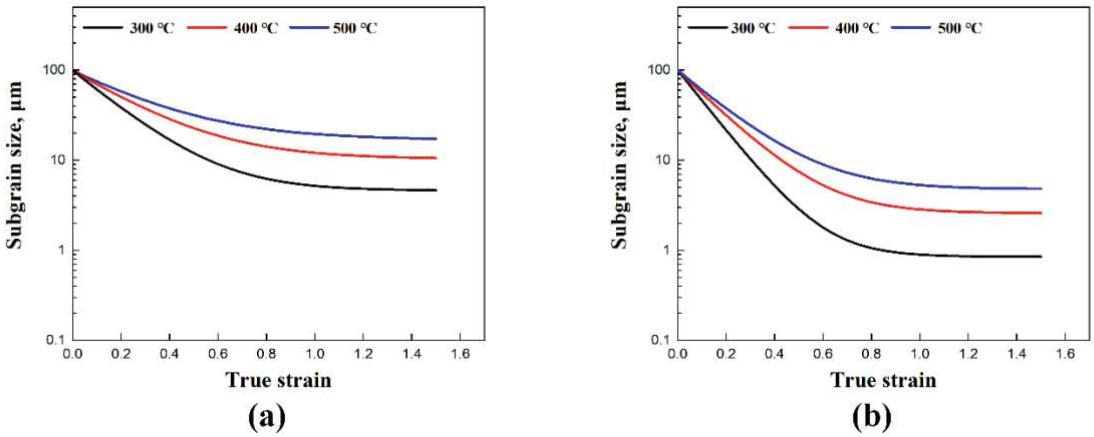

Figure 11. Simulated average subgrain size (δ_{sub}) by the substructure-based model with different temperatures at a strain rate of (a) 0.01 s^{-1} and (b) 0.8 s^{-1}.

The substantial generation of new subgrains significantly influences the mechanical properties of the material. The correlation between mechanical properties and microstructure is discussed in the context of subgrain strengthening. Typically, subgrain boundary strengthening is considered to be inversely proportional to the square of the average subgrain size, as described by the Hall-Petch relationship (case 1) [56],

$$\sigma_{sub} = k_{sub}\delta_{sub}^{-1/2}, \quad (12)$$

where σ_{sub} is the strengthening contribution coming from subgrain boundaries, and k_{sub} is a material constant for subgrain boundary strengthening, set as 10 MPa·μm$^{1/2}$. In this work, the value of δ_{sub} was calculated using the substructure-based model.

Another subgrain strengthening model (case 2) was used to compare with the empirical Hall-Petch relationship, as suggested by Marthinsen and Nes [29]. The formula can be written as follows:

$$\sigma_{\text{sub}} = \alpha_{\text{sub}} MGb / \frac{b}{\delta_{\text{sub}}}, \tag{13}$$

where α_{sub} is a material constant and was selected to be 0.83 for Al alloy, as suggested by Duan and Sheppard [27].

Figure 12 illustrates the subgrain strengthening calculations of the Hall-Petch relationship (case 1) and Marthinsen and Nes model (case 2) under different deformation conditions. The refinement of subgrain results in strength improvements and their corresponding characteristics. During the initial stage of deformation, the subgrain size is relatively large, leading to minimal subgrain boundary strengthening. As deformation progresses, the generation of a significant number of fine subgrains contributes to an increase in stress. Once the subgrain size exceeds the critical threshold for refinement, the steady-state subgrain size results in a balanced rate of increase in subgrain strengthening, in agreement with studies from Hansen [56] and Summers et al. [57].

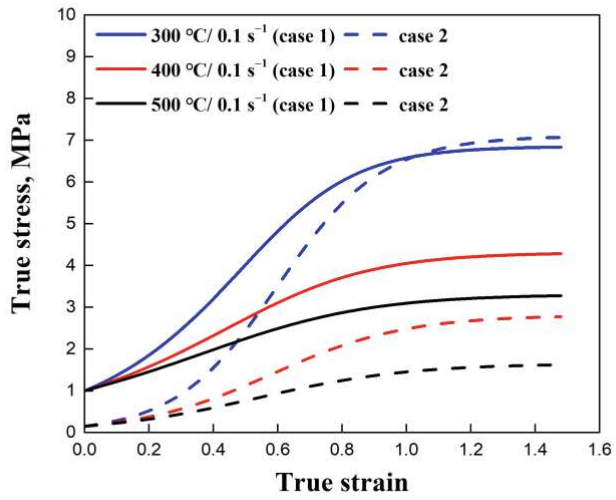

Figure 12. Subgrain strengthening calculations of Hall-Petch relationship (case 1) and Marthinsen and Nes model (case 2) under different deformation conditions.

5. Conclusions

The paper reflects the substructure evolution of an AA1050 Al alloy under various deformation conditions during high-temperature compression. Subsequently, two subgrain size evolution models were applied based on EBSD experiments. The main conclusions are as

follows:

(1) A detailed substructure is provided with subgrain/grain boundary characteristics. The results revealed the dependence of the average subgrain size on factors such as temperature, strain rate, and strain, and their special roles on subgrain refinement and thermal coarsening were captured;

(2) The mechanism and deformation variables, including subgrain formation and refinement, were discussed in detail, considering the average subgrain size, misorientations angles, and the distribution of subgrains. The coexistence of subgrain refinement and thermal coarsening varies with changes in deformation conditions and the corresponding average subgrain size was also measured directly from EBSD experiments;

(3) An empirical model and an advanced substructure-based model of average subgrain size were established with several internal state variables. In the established models, the process of subgrain evolution is described by introducing saturated average subgrain size, dislocation density, misorientation angle, subgrain boundary energy, etc. The evolution of average subgrain size can be effectively well reproduced across a range of temperatures and strain rates;

(4) In the substructure-based model, various factors such as the material coefficients, initial subgrain size, temperature, and strain rate were analyzed. The correlation coefficient (R) and root mean square error ($RMSE$) of the substructure-based model were calculated to be 0.98 and 5.7%, respectively, which indicate good agreement between the experiment and the model;

(5) The mechanism of subgrain boundary formation and refinement were discussed in detail, and subgrain strengthening was also studied with the Hall-Petch relationship.

Author Contributions: Conceptualization, Q.Y. and E.K.; methodology, Q.Y., T.W., and E.K.; validation, Q.Y. and E.K.; formal analysis, Q.Y.; investigation, Q.Y. and T.W.; resources, E.K. and T.W.; data curation, Q.Y. and T.W.; writing—original draft preparation, Q.Y. and E.K.; writing—review and editing, E.K.; visualization, Q.Y., T.W., and E.K.; supervision, E.K.; project administration, E.K.; funding acquisition, Q.Y. and E.K. All authors have read and agreed to the published version of the manuscript.

Funding: Open access funding provided by TU Wien (TUW).

Data Availability Statement: The raw data supporting the conclusions of this article will be made available by the authors on request.

Acknowledgments: Qi Yang appreciates the financial support from the State Scholarship Fund of China (No. 202107710006) during his PhD at TU Wien.

Conflicts of Interest: The authors declare no conflicts of interest.

References

1. F.J. Humphreys, and M. Hatherly. Recrystallization and related annealing phenomena. 2004, 2nd edn. Elsevier, Oxford.
2. R.D. Doherty, D.A. Hughes, F.J. Humphreys, J.J. Jonas, D. Juul Jensen, M.E. Kassner, T.R. McNelley, H.J. McQueen, and A.D. Rollet. Current issues in recrystallization: a review. Mater. Sci. Eng., A, 1997, vol. 238, pp. 219-274.
3. J.X. Lv, J.H. Zheng, V.A. Yardley, Z.S. Shi, and J.G. Lin. A review of microstructural evolution and modelling of aluminium alloys under hot forming conditions. Metals, 2020, vol. 10, pp. 1516.
4. R. Kaibyshev, K. Shipilova, F. Musin, and Y. Motohashi. Continuous dynamic recrystallization in an Al-Li-Mg-Sc alloy during equal-channel angular extrusion. Mater. Sci. Eng. A, 2005, vol. 396, pp. 341-351.
5. J.C. Li, X.D. Wu, L.F. Cao, B. Liao, Y.C. Wang, and Q. Liu. Hot deformation and dynamic recrystallization in Al-Mg-Si alloy. Mater. Charact., 2021, vol. 173, pp. 110976.
6. J.W. Lee, K.T. Son, T.K. Jung, Y.O. Yoon, S.K. Kim, H.J. Choi, and S.K. Hyun. Continuous dynamic recrystallization behavior and kinetics of Al-Mg-Si alloy modified with CaO-added Mg. Mater. Sci. Eng., A, 2016, vol. 673, pp. 648-659.
7. X.M. Feng, Y.T. Wang, Q.G. Huang, H.L. Liu, and Z.H. Zhang. The dynamic recrystallization microstructure characteristics and the effects on static recrystallization and mechanical properties of Al-Mg-Si alloy. Mater. Sci. Eng. A, 2024, vol. 899, pp. 146454.
8. J.J. Zhang, Y.P. Yi, S.Q. Huang, X.C. Mao, H.L. He, J.G. Tang, W.F. Guo, and F. Dong. Dynamic recrystallization mechanisms of 2195 aluminum alloy during medium/high temperature compression deformation. Mater. Sci. Eng., A, 2021, vol. 804, pp. 140650.
9. T. Sakai, H. Miura, A. Goloborodko, and O. Sitdikov. Continuous dynamic recrystallization during the transient severe deformation of aluminum alloy 7475. Acta Mater., 2009, vol. 57, pp. 153-162.
10. G. Maizza, R. Pero, M. Richetta, and R. Montanari. Continuous dynamic recrystallization (CDRX) model for aluminum alloys. J. Mater. Sci., 2018, vol. 53, pp. 4563-4573.
11. Q. Yang, T. Wojcik, and E. Kozeschnik. Continuous dynamic recrystallization and deformation behavior of an AA1050 aluminum alloy during high-temperature compression. Metals, 2024, vol. 14, pp. 889.

12. K. Huang, and R.E. Logé. A review of dynamic recrystallization phenomena in metallic materials. Mater. Design, 2016, vol. 111, pp. 548-574.
13. T. Sakai, A. Belyakov, R. Kaibyshev, H. Miura, and J.J. Jonas. Dynamic and post-dynamic recrystallization under hot, cold and severe plastic deformation conditions. Prog. Mater. Sci., 2014, vol. 60, pp. 130-207.
14. J.J. Zhang, Y.P. Yi, H.L. He, S.Q. Huang, X.C. Mao, W.F. Guo, W. You, Y.L. Guo, F. Dong, and J.G. Tang. Kinetic model for describing continuous and discontinuous dynamic recrystallization behaviors of 2195 aluminum alloy during hot deformation. Mater. Charact., 2021, vol. 181, pp. 111492.
15. S. Ding, S.A. Khan, and J. Yanagimoto. Flow behavior and dynamic recrystallization mechanism of A5083 aluminum alloys with different initial microstructures during hot compression. Mater. Sci. Eng., A, 2020, vol. 787, pp. 139522.
16. H. Li, Y.C. Huang, and Y. Liu. Dynamic recrystallization mechanisms of as-forged Al-Zn-Mg-(Cu) aluminum alloy during hot compression deformation. Mater. Sci. Eng., A, 2023, vol. 878, pp. 145236.
17. C. Illgen, B. Bohne, M.F.X. Wagner, and P. Frint. Thermal stability of SPD-processed aluminum alloys–Internal friction as an indication for recovery, recrystallization and abnormal grain growth. J. Mater. Res. Technol., 2022, vol.17, pp. 1752-1759.
18. Z.J. Meng, C.S. Zhang, G.F. Zhang, K.Z. Wang, Z.J. Wang, L. Chen, and G.Q. Zhao. Hot compressive deformation behavior and microstructural evolution of the spray-formed 1420 Al-Li alloy. J. Mater. Res. Technol., 2023, vol. 27, pp. 4469-4484.
19. K.Z. Wang, C.S. Zhang, Z.N. Cheng, H.B. Zhao, Z.J. Meng, L. Chen, and G.Q Zhao. Dynamic evolution of the T1 phase and its effect on continuous dynamic recrystallization in Al-Cu-Li alloys. Int. J. Plast., 2024, vol. 175, pp. 103948.
20. X. Velay. Prediction and control of subgrain size in the hot extrusion of aluminium alloys with feeder plates. J. Mater. Process. Technol., 2009, vol. 209, pp. 3610-3620.
21. C. Poletti, M. Rodriguez-Hortalá, M. Hauser, and C. Sommitsch. Microstructure development in hot deformed AA6082. Mater. Sci. Eng., A, 2011, vol. 528, pp. 2423-2430.
22. C. Sellars, and Q. Zhu, Microstructural modelling of aluminium alloys during thermomechanical processing, Mater. Sci. Eng., A, 2000, vol. 280, pp. 1-7.
23. T. Furu, R. Ørsund, and E. Nes, Subgrain growth in heavily deformed aluminium-experimental investigation and modelling treatment. Acta Metall. Mater., 1995, vol. 43, pp. 2209-2232.

24. E. Nes, H.E. Vatne, O. Daaland, T. Furu, R. Ørsund, and K. Marthinsen. Physical modelling of microstructural evolution during thermomechanical processing of aluminium alloys. 1994, Report STF24 S94003, SINTEF, Trondheim, Norway.
25. E. Nes. Modelling of work hardening and stress saturation in FCC metals. Prog. Mater. Sci., 1998, vol. 41, pp. 129-193.
26. T. Sheppard. Development of structure, recrystallization kinetics and prediction of recrystallized layer thickness in some Al-alloys. 1996, Proceedings of the 6th International Seminar on Aluminium Extrusion Technology, vol. 1. Aluminium Association and Aluminium Extruder Council, Chicago, USA, pp. 163-170.
27. X. Duan, and T. Sheppard. Simulation of substructural strengthening in hot flat rolling. J. Mater. Process. Technol., 2002, vol. 125-126, pp. 179-187.
28. X. Duan, and T. Sheppard. Three dimensional thermal mechanical coupled simulation during hot rolling of aluminium alloy 3003. J. Mater. Sci., 2002, vol. 44, pp. 2155-2172.
29. K. Marthinsen, and E. Nes. Modelling strain hardening and steady state deformation of Al-Mg alloys. Mater. Sci. Technol., 2001, vol. 17, pp. 376-388.
30. S. Gourdet, and F. Montheillet. A model of continuous dynamic recrystallization. Acta Mater., 2003, vol. 51, pp. 2685-2699.
31. Z.C. Sun, H.L. Wu, J. Cao, and Z.K. Yin. Modeling of continuous dynamic recrystallization of Al-Zn-Cu-Mg alloy during hot deformation based on the internal-state-variable (ISV) method. Int. J. Plast., 2018, vol. 106, pp. 73-87.
32. S.F. Chen, D.Y. Li, S.H. Zhang, H.N. Han, H.W. Lee, and M.G. Lee. Modelling continuous dynamic recrystallization of aluminum alloys based on the polycrystal plasticity approach. Int. J. Plast., 2020, vol. 131, pp. 102710.
33. F. Chen, X. Tian, G.S. Wu, H.J. Zhu, H.A. O, and Z.S. Cui. Coupled quantitative modeling of microstructural evolution and plastic flow during continuous dynamic recrystallization. Int. J. Plast., 2022, vol. 156, pp. 103372.
34. T. Furu, H.R. Shercliff, C.M. Sellars, and M.F. Ashby. Physically-based modelling of strength, microstructure and recrystallisation during thermomechanical processing of Al-Mg alloys. Mater. Sci. Forum, 1996, vol. 217, pp. 453-458.
35. O.D. Sherby, R.H. Klundt, and A.K. Miller. Flow stress, subgrain size, and subgrain stability at elevated temperature. Metall. Trans. A, 1977, vol. 8, pp. 843-850.
36. H. Hallberg, M. Wallin, and M. Ristinmaa. Modeling of continuous dynamic recrystallization in commercial-purity aluminum. Mater. Sci. Eng., A, 2010, vol. 527, pp. 1126-1134.

37. Y. Huang, and F.J. Humphreys. Subgrain growth and low angle boundary mobility in aluminium crystals of orientation {110}〈001〉. Acta Mater., 2000, vol. 48, pp. 2017-2030.
38. P. Sherstnev, P. Lang, and E. Kozeschnik: in Eur. congr. comput. methods appl. sci. eng. (ECCOMAS 2012), 10.-14.9.2012, J. Eberhardsteiner et.al., ed., Vienna, Austria, 2012, pp. 1-8.
39. J. Kreyca, and E. Kozeschnik. State parameter-based constitutive modelling of stress strain curves in Al-Mg solid solutions. Int. J. Plast., 2018, vol. 103, pp. 67-80.
40. H. Buken, and E. Kozeschnik. Modeling static recrystallization in Al-Mg alloys. Metall. Mater. Trans. A, 2021, vol. 52, pp. 544-552.
41. D. Raabe, 23 - Recovery and Recrystallization: Phenomena, Physics, Models, Simulation, in: D.E. Laughlin, K. Hono (Eds.), Physical Metallurgy, Elsevier, Oxford, 2014, pp. 2291-2397.
42. H.J. McQueen, and M.E. Kassner. Comments on 'a model of continuous dynamic recrystallization' proposed for aluminum. Scr. Mater., 2004, vol. 51, pp. 461-465.
43. T. Federighi. A possible determination of the activation energy for self-diffusion in aluminium. Philos. Mag., 1959, vol. 4, pp. 502-510.
44. J.P. Hirth and J. Lothe. Theory of dislocations. Krieger Publishing Company, 1991.
45. E.I. Galindo-Nava and P.E.J. Rivera-Díaz-del-Castillo. A thermostatistical theory of low and high temperature deformation in metals. Mater. Sci. Eng., A, 2012, vol. 543, pp. 110-116.
46. H. Mecking, B. Nicklas and N. Zarubova. A universal temperature scale for plastic flow. Acta Mater., 1986, vol. 34, pp. 527-535.
47. H. Frost and M. Ashby. Deformation-mechanism maps, first ed. Pergamon Press, Oxford, 1982.
48. Y. Bergström. The plastic deformation of metals-a dislocation model and its applicability. Rev. Powder Metall. Phys. Ceram., 1983, vol. 2, pp. 79-265.
49. A. Alankar, D.P. Field and D. Raabe. Plastic anisotropy of electro-deposited pure a-iron with sharpcrystallographic <111>// texture in normal direction: Analysis by an explicitly dislocation-based crystal plasticity model. Int. J. Plast., 2014, vol. 52, pp. 18-32.
50. H. Mirzadeh, J.M. Cabrera, and A. Najafizadeh. Modeling and prediction of hot deformation flow curves. Metall. Mater. Trans. A, 2012, vol. 43, pp. 108-123.
51. S. Gourdet, and F. Montheillet. An experimental study of the recrystallization mechanism during hot deformation of aluminium. Mater. Sci. Eng., A, 2000, vol. 283, pp. 274-288.

52. Z. Yanushkevich, A. Belyakov, and R. Kaibyshev. Microstructural evolution of a 304-type austenitic stainless steel during rolling at temperatures of 773-1273 K. Acta Mater., 2015, vol. 82, pp. 244-254.
53. G.C. Wu, Y.C. Lin, M.S. Chen, W. Qiu, N.F. Zeng, S. Zhang, M. Wan, D.G. He, Y.Q. Jiang, and M. Naseri. Continuous dynamic recrystallization behaviors in a single-phase deformed Ti-55511 alloy by cellular automata model. J. Alloys Compd., 2024, vol. 1002, pp. 175293.
54. J.A. Hines, K.S. Vecchio, and S. Ahzi. A model for microstructure evolution in adiabatic shear bands. Metall. Mater. Trans. A, 1998, vol. 29, pp. 191-203.
55. S. Wu, K. Fan, P. Jiang, and S. Chen. Grain refinement of pure Ti during plastic deformation. Mater. Sci. Eng., A, 2010, vol. 527, pp. 6917-6921.
56. N. Hansen. Hall-Petch relation and boundary strengthening. Scr. Mater., 2004, vol. 51, p. 801-806.
57. P.T. Summers, A.P. Mouritz, S.W. Case, and B.Y. Lattimer. Microstructure-based modeling of residual yield strength and strain hardening after fire exposure of aluminum alloy 5083-H116. Mater. Sci. Eng. A, 2015, vol. 632, pp. 14-28.

Paper III

A dislocation-based model for substructure evolution and flow stress of aluminum alloys during high-temperature compression

Qi Yang, Tomasz Wojcik and Ernst Kozeschnik

Manuscript (submitted)

A dislocation-based model for substructure evolution and flow stress of aluminum alloys during high-temperature compression

Qi Yang, Tomasz Wojcik, and Ernst Kozeschnik*

Institute of Materials Science and Technology, TU Wien, Getreidemarkt 9, 1060 Vienna, Austria
*Correspondence: ernst.kozeschnik@tuwien.ac.at

Abstract: The microstructure evolution of aluminum alloys during plastic deformation is a complex metallurgical process controlled by interacting physical mechanisms, such as recovery, continuous dynamic recrystallization (CDRX), and substructure evolution. The present study proposes a dislocation-based model framework to describe the microstructural evolution of dislocation density, subgrain size, misorientation angle, and flow stress. The wall dislocation density is modeled on the basis of the average subgrain size and misorientation evolution. The dislocation density and substructure evolution are independently simulated and compared with electron backscatter diffraction (EBSD) experimental results. Their mechanisms are thoroughly discussed. The framework is successfully applied and validated for AA1050 and AA5052 aluminum alloys across different deformation conditions.

Keywords: microstructure evolution, hot deformation, dynamic recrystallization, dynamic recovery, dislocation density, physical modeling.

1. Introduction

Many researchers [1-9] have studied the microstructure evolution laws under various conditions for high-stacking fault energy materials, such as aluminum alloys, indicating that recovery and DRX are essential softening mechanisms during hot forming. Recovery is a softening process during which defects, primarily dislocations, are either annihilated or rearranged to reduce the internal energy of the material [10-11].

Consequently, continuous deformation contributes to an increased misorientation of low-angle subgrain boundaries (LAGBs), which progressively transform into high-angle grain boundaries (HAGBs) with misorientation angles exceeding 15°, as observed in continuous dynamic recrystallization (CDRX) [12-13]. CDRX is the most common mechanism observed in Al alloys during hot forming. The other two forms are discontinuous dynamic

recrystallization (DDRX) [14-15] and geometric dynamic recrystallization (GDRX) [16-17]. In contrast to DDRX, CDRX is a non-nucleation process, the primary mechanism of CDRX being the continuous rotation of subgrains [18-20]. Sakai et al. [9] and Huang and Logé [10] reviewed the mechanism of microstructural evolution and DRX in Al alloy during hot deformation and severe plastic deformation (SPD).

Understanding and modeling complex dislocation density reactions are the keys to controlling the DRX and deformation behavior of Al alloy. Several approaches [21-23] are reported in the literature describing the dislocation density and flow curves of aluminum alloys during hot deformation.

The dislocation density-based models for metal plasticity rely on the work of Kocks [24], Bergström [25], Bergström and Roberts [26], and Mecking and Estrin [27]. Kocks and Mecking [28] modeled and reviewed the dislocation-caused flow stress with dislocation accumulation and annihilation during the deformation of FCC metals, called the Kocks and Mecking (KM) dislocation model, which is the basis of many subsequent microstructure evolution models. Roters, Raabe, and Gottstein [29] established a new work-hardening model for homogeneous and heterogeneous cell-forming alloys. They distinguish three internal state variables in terms of three categories of dislocations: mobile and immobile dislocations in the cell interiors and immobile dislocations in the cell walls.

Material models for DDRX-based microstructure evolution are frequent in the literature [30-33], while physical models of substructure evolution and subsequent CDRX processes are more scarce. A physically-based CDRX model was proposed by Gourdent and Montheillet [34], the GM model, which considers the average dislocation density, the average crystallite size, and subgrain boundary misorientation. Sun et al. [35] modified the GM model by adding subgrain boundary area, recrystallized grain boundary area, and high-angle grain boundary area as internal-state variables. Chen et al. [36] modified the GM model with a coupled CDRX-VPSC (visco-plastic self-consistent) model that employs dislocation density. Buzolin et al. [37] developed a microstructure model for two-phase titanium alloys, comprising microstructure, yield stress, constitutive equations, plastic strain partitioning, and rate equations for the internal variables. Furthermore, Li et al. [38] and Chen et al. [39] have also developed models recently based on the GM model.

The present work proposes a dislocation-based model framework to reproduce dislocation population dynamics and microstructural evolution in Al alloys. The dislocation model accounts for work hardening and various annihilation mechanisms within cell interiors. Additionally, a wall density model is established by incorporating substructure evolution

calculations. The microstructural evolution laws are simulated as functions of temperature, strain, and strain rate. Moreover, the models are individually analyzed and validated against independent experimental data, showing good agreement between the simulations and experiments.

2. State of the art

Fig. 1 illustrates the microstructure evolution laws during continuous compression as used here. The initial microstructure, before deformation, consists of a parent structure with a low number of pre-existing dislocations (Fig. 1a). As deformation progresses, the accumulation and rearrangement of tangled dislocations results in the formation of newborn cells and subgrains through DRV (Fig. 1b). These subgrains gradually increase their boundary misorientation due to subgrain rotation, ultimately converting some of the low-angle subgrains into HAGBs [34] (Fig. 1c). Additionally, as the subgrains absorb dislocations, their misorientation further increases, as suggested by Huang and Logé [10]. With continued compression, the microstructure eventually reaches a steady state.

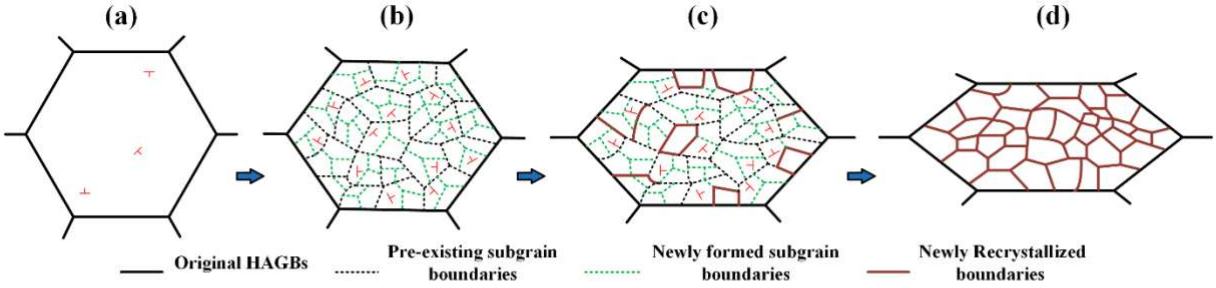

Evolution / Variables	Step (a)	Step (b)	Step (c)	Step (d)
Excess Dislocation density ρ	0	↑	↓	Constant
δ_{sub}	None	↓	δ_{DRX}	Constant
X_{DRX}	0	0	↑	=100%
Subgrain misorientation θ	0°	>2° ↑	Some>15° ↑	Constant
D	D0	D0	↓	δ_{DRX}

Fig. 1. Illustration of the microstructure evolution laws during continuous compression: (a) initial microstructure before deformation; (b) generation of cells and subgrains; (c) generation of recrystallized grains; (d) full recrystallization state.

The microstructure evolution and associated discussions in the literature [9-10,20] describe the formation of a well-defined substructure and subsequent DRX. The main microstructural evolution mechanisms observed in Al alloys can be summarized as follows: (i) dislocations with a density ρ accommodate plastic deformation. The changes in density stem

from the balance between their generation, annihilation, and transformation into wall dislocations. (ii) The average subgrain size δ_{sub} decreases with deformation and reaches a "saturation value" at large strains [10,40-42]. (iii) The misorientation angle of subgrains θ gradually increases to a critical angle with the evolution of dislocation density and subgrain size. (iv) DRX can occur during the hot compression of Al alloys [20], with the DRX fraction X_{DRX} increasing as the misorientation of low-angle subgrains increases, leading to their progressive transformation into HAGBs. (v) The average grain size D continues to decrease from the initial mean grain size D_0 until complete recrystallization is achieved, resulting in a newly recrystallized grain size δ_{DRX}.

These variables are incorporated into the present dislocation-based CDRX model for Al alloys to simulate the microstructure evolution under various deformation conditions. The work primarily develops models for interior and wall dislocation densities, average subgrain size, subgrain boundary misorientation, and flow stress based on substructure evolution.

3. Model development

3.1. Dislocation density evolution model

In high-stacking fault energy materials, such as Al alloys, dislocations can arrange themselves into well-organized cell or subgrain structures with continued deformation, leading to the gradual increase of subgrain misorientation [9-10]. The wall dislocation density of subgrain boundaries strongly depends on the various deformation parameters.

In the present work, the proposed evolution models incorporate dislocation density, average subgrain size, and subgrain misorientation angle as internal variables representing the material's microstructure. The total dislocation density (ρ_{t}) is divided into two populations: the interior dislocations with a density ρ_{i} and the wall dislocations with a density ρ_{w}. The interior dislocation density represents the dislocations within parent grains and newly formed subgrains, while the wall dislocation density represents the dislocations at the newly formed cell or subgrain walls.

Considering the rule of mixtures applied to two populations, the total dislocation density (ρ_{t}) can be calculated as

$$\rho_{\mathrm{t}} = f_{\mathrm{i}}\rho_{\mathrm{i}} + f_{\mathrm{w}}\rho_{\mathrm{w}}, \tag{1}$$

where f_{i} represents the material coefficient related to the fraction of interior dislocations, and f_{w} is a material coefficient related to the fraction of wall dislocations, with $f_{\mathrm{i}} + f_{\mathrm{w}} = 1$.

The interior dislocation density model incorporates several mechanisms that determine the

dislocation evolution. It is described with the ABC dislocation model [23, 43-44] and the GM model [34]. This model mainly describes the following evolution processes: work hardening (WH), the reduction of dislocation density through DRV and static recovery (SRV), as well as the average dislocation reduction caused by HAGBs movement as

$$d\rho_{\mathrm{i}}/dt = \frac{M\sqrt{\rho_{\mathrm{i}}}}{Ab}\dot{\varepsilon} - 2BM\rho_{\mathrm{i}}\frac{d_{\mathrm{crit}}}{b}\dot{\varepsilon} - 2CD_{\mathrm{d}}\frac{Gb^3}{k_{\mathrm{B}}T}\left({\rho_{\mathrm{i}}}^2 - \rho_{\mathrm{eq}}^2\right) - 2f_{\mathrm{H}}v_{\mathrm{H}}\rho_{\mathrm{i}}\frac{1}{\delta_{\mathrm{w}}}, \quad (2)$$

where A, B and C are material-dependent coefficients, M is the Taylor factor, G the shear modulus, b the Burger's vector, $\dot{\varepsilon}$ the strain rate, k_{B} the Boltzmann constant, T the deformation temperature, d_{crit} the critical distance of dislocation annihilation, D_{d} the diffusion coefficient along dislocation pipes, ρ_{eq} is the equilibrium dislocation density, δ_{w} the average size (diameter) of low-angle walls/subgrains, f_{H} the fraction of HAGBs, and v_{H} is the migration rate of HAGBs.

The last term in eq. (2) accounts for the reduction of the average internal dislocation density accompanying the migration of HAGBs. The rate of HAGBs is adopted from Gourdet and Montheillet [34] as

$$v_{\mathrm{H}} = v_0\left(\frac{\dot{\varepsilon}}{\dot{\varepsilon_0}}\right)^m, \quad (3)$$

where $\dot{\varepsilon_0}$ is the initial value of the strain rate, v_0 the initial migration rate of HAGBs, and m is a material constant related to the migration rate.

The average dislocation annihilation due to DRV occurs when two dislocations with antiparallel Burgers vectors approach each other within a critical distance d_{crit}, leading to their annihilation. The critical distance d_{crit} can be theoretically derived from the dislocation annihilation mechanism, which is expressed as [45]

$$d_{\mathrm{crit}} = \frac{Gb^4}{2\pi(1-\nu)Q_{\mathrm{vac}}}, \quad (4)$$

where ν is the Poisson's ratio, and Q_{vac} is the vacancy formation energy.

The diffusion coefficient along dislocation pipes D_{d} can be expressed as [46]

$$D_{\mathrm{d}} = D_{\mathrm{d0}}\exp\left(\frac{Q_{\mathrm{d}}}{RT}\right), \quad (5)$$

where D_{d0} is the pre-exponential factor for pipe diffusion, Q_{d} is the activation energy for pipe diffusion, and R is the gas constant.

Since dislocation generation continues while deformation proceeds, an increasing number of dislocations are piled up, leading to the formation of new low-angle subgrains/LAGBs [9-10]. The evolution of the wall dislocation density is directly considered with changes in the corresponding substructure variables, reproducing the expected evolution of substructure and dislocations using physically-based parameters. The wall dislocation density model is

represented as the total length of wall dislocation lines per unit volume, expressed as [47]

$$\rho_{\mathrm{w}} = \frac{\sum_1^i L_{\mathrm{w}i}}{\sum_1^i V_{\mathrm{w}i}} = f_{\mathrm{s}} \frac{\theta_{\mathrm{w}i}}{2b} r_i, \tag{6}$$

where $L_{\mathrm{w}i}$ is the total length of wall dislocation lines of the i-th subgrain wall, $V_{\mathrm{w}i}$ is the total volume of the i-th subgrain wall, $\theta_{\mathrm{w}i}$ is the average misorientation angle of the i-th subgrain walls, r_i is the ratio of subgrain surface to subgrain volume of the i-th subgrain walls, and f_{s} is a materials coefficients related to the subgrain boundary fraction, is taken as 1/8 in present work.

Subsequently, the average low-angle subgrain size (diameter of subgrains), denoted as δ_{w} and the subgrain misorientation angle θ_{w} are introduced for modeling, allowing the wall dislocation density to be expressed as

$$\rho_{\mathrm{w}} = f_{\mathrm{s}} \frac{\theta_{\mathrm{w}}}{2b} \pi {\delta_{\mathrm{w}}}^2 / \left(\frac{4}{3}\pi \left(\frac{\delta_{\mathrm{w}}}{2}\right)^3\right), \tag{7}$$

where θ_{w} is the average misorientation angle of subgrain walls (cells).

3.2. Subgrain size evolution model

The high-temperature deformation of Al alloys typically occurs in three stages [1, 9-10, 47]: (i) An initial stage where cells/subgrain boundaries are formed, followed by (ii) subgrain refinement and (iii) thermal coarsening of subgrains. The substructure-based model for the average subgrain size evolution has been reported in a previous paper and literature [42,48-49] and reads

$$d\delta_{\mathrm{w}}/dt = -f_{\mathrm{r}} \frac{\sqrt{3}\dot{\varepsilon} b^{1/2}}{\bar{\theta}_{\mathrm{s}}^{\,3/2} \bar{\delta}_{\mathrm{s}}^{\,2}} {\delta_{\mathrm{w}}}^{v_1} + f_{\mathrm{c}} \nu_{\mathrm{D}} b^2 \sqrt{\rho_{\mathrm{t}}} \left[\exp - \left(\frac{U_{\mathrm{s}} - PV_{\mathrm{a}}}{k_{\mathrm{B}} T}\right)\right], \tag{8}$$

where ν_{D} is the Debye frequency, P the driving force on the subgrain boundary, V_{a} the average activation volume of subgrain boundaries, U_{s} the activation energy for self-diffusion in Al, f_{r} and f_{c} are material coefficients related to subgrain evolution, $\bar{\theta}_{\mathrm{s}}$ is the average subgrain boundary misorientation in the steady-state stage, v_1 a material coefficient that controls the subgrain refinement rate and which is set to 1 in the present work, and $\bar{\delta}_{\mathrm{s}}$ is the average subgrain size in the steady-state stage.

The driving force for subgrain coarsening is governed by the evolution of subgrain boundary energy and subgrain size, as described in Eq. (9). In this equation, the prediction of subgrain boundary energy is performed using the Read-Shockley relationship [48-50] with

$$P = \frac{4\gamma}{\delta_{\mathrm{w}}}, \text{ with } \gamma = \gamma_{\mathrm{m}} \frac{\theta_{\mathrm{w}}}{\theta_{\mathrm{m}}} \left(1 - \ln\left(\frac{\theta_{\mathrm{w}}}{\theta_{\mathrm{m}}}\right)\right), \tag{9}$$

where γ represents the subgrain boundary energy, γ_{m} is the boundary energy of HAGBs, and θ_{m} is the misorientation angle at which a boundary is defined as a HAGB, typically taken as 15°.

The activation volume of subgrain boundaries is determined by the average misorientation angle, which is used as [48]

$$V_{\mathrm{a}} = \frac{b^3}{\theta_{\mathrm{w}}} \tag{10}$$

3.3. Misorientation angle evolution model

In section 3.1, we evaluate the dislocation density evolution during DRV and SRV. Following the methodology of Gourdet and Montheillet [34], the calculation incorporates both the annihilation and transformation of dislocations during recovery. A fraction α_{s} of the dislocations is removed by recovery, while the remaining fraction $1-\alpha_{\mathrm{s}}$, contributes to the formation of new subgrains and an increase of the misorientation angle. The rate of the dislocation density during deformation and subgrain rotation is then [34]

$$d\rho_{\mathrm{sr}}/dt = \frac{(1-\alpha_{\mathrm{s}})}{\alpha_{\mathrm{s}}}\left(2BM\rho_{\mathrm{i}}\frac{d_{\mathrm{crit}}}{b}\dot{\varepsilon} - 2CD_{\mathrm{d}}\frac{Gb^3}{k_{\mathrm{B}}T}\left({\rho_{\mathrm{i}}}^2 - \rho_{\mathrm{eq}}^2\right)\right), \tag{11}$$

where ρ_{sr} represents the total recovered dislocation density involved in subgrain rotation, and $1-\alpha_{\mathrm{s}}$ is the fraction of recovered dislocations that participate in subgrain rotation. This quantity is taken as 0.5.

Subsequently, an extended subgrain misorientation angle model is developed that considers various factors, including dislocation density, strain rate, average subgrain size, and subgrain boundary energy. The equation reads as

$$d\theta_{\mathrm{w}}/dt = f_{\theta}\frac{b\dot{\varepsilon}\delta_{\mathrm{w}}}{2n}\frac{(1-\alpha_{\mathrm{s}})}{\alpha_{\mathrm{s}}}\left(2BM\rho_{\mathrm{i}}\frac{d_{\mathrm{crit}}}{b}\dot{\varepsilon} - 2CD_{\mathrm{d}}\frac{Gb^3}{k_{\mathrm{B}}T}\left({\rho_{\mathrm{i}}}^2 - \rho_{\mathrm{eq}}^2\right)\right)\gamma^{c_2}, \tag{12}$$

where n is the number of dislocation pairs within the boundary, with a value of 3 as suggested by Gourdet and Montheillet [34]. c_2 is a material constant that describes the relationship between the average misorientation angle and the subgrain boundary energy, and f_{θ} is a material coefficient related to the saturated misorientation angle.

Numerous researchers have observed that the average misorientation of subgrains consistently reaches a steady-state value of about 4° to 8° for aluminum alloys when subjected to critical strain levels [10,51-52], such that the misorientation angle is no longer sensitive to increasing deformation strain, since $d\theta_{\mathrm{w}}/dt = 0$. Consequently, a material coefficient f_{θ} is introduced into the model, with the saturated misorientation angle θ_{sat} being expressed as

$$f_{\theta} = c_3\left(1 - \frac{\theta_{\mathrm{w}}}{\theta_{\mathrm{sat}}}\right), \tag{13}$$

where c_3 is a material constant that describes the relationship between the average misorientation angle and the saturated misorientation angle. θ_{sat} is the saturated misorientation angle with continuing deformation.

3.4. Constitutive model

Here, various strengthening theories are employed to describe the relationship between macroscopic flow stress and the microstructure of an AA1050 Al alloy, focusing on the basic yield strength and dislocation strengthening mechanisms. The contributions of two types of dislocations (interior dislocation density ρ_i and wall dislocation density ρ_w) to the flow stress are accounted for in a modified Taylor equation [53] as

$$\sigma = \sigma_0 + \alpha MGb(f_i\sqrt{\rho_i} + f_w\sqrt{\rho_w}), \tag{14}$$

where σ_0 is the basic yield strength, and α is the strengthening coefficient related to interior and wall dislocation densities.

From the above discourse, the set of constitutive equations is

$$\begin{cases} d\rho_i/dt = \frac{M\sqrt{\rho_i}}{Ab}\dot{\varepsilon} - 2BM\rho_i\frac{d_{crit}}{b}\dot{\varepsilon} - 2CD_d\frac{Gb^3}{k_BT}\left({\rho_i}^2 - \rho_{eq}^2\right) - 2f_H v_H \rho_i \frac{1}{\delta_w} \\ \rho_w = f_s\frac{\theta_w}{2b}\pi{\delta_w}^2/(\frac{4}{3}\pi(\frac{\delta_w}{2})^3) \\ d\delta_w/dt = -f_r\frac{\sqrt{3}\dot{\varepsilon}b^{1/2}}{\bar{\theta}_s^{3/2}\bar{\delta}_s^{2}}{\delta_w}^{v_1} + f_c v_D b^2\sqrt{\rho_t}\left[\exp - \left(\frac{U_s - PV_a}{k_BT}\right)\right] \\ d\theta_w/dt = c_3\left(1 - \frac{\theta_w}{\theta_{sat}}\right)\frac{b\dot{\varepsilon}\delta_w}{2n}\frac{(1-\alpha_s)}{\alpha_s}(2BM\rho_i\frac{d_{crit}}{b}\dot{\varepsilon} - 2CD_d\frac{Gb^3}{k_BT}\left({\rho_i}^2 - \rho_{eq}^2\right))\gamma^{c_2}, \\ \sigma = \sigma_0 + \alpha MGb(f_i\sqrt{\rho_i} + f_w\sqrt{\rho_w}) \\ P = \frac{4\gamma}{\delta_w}, \text{with } \gamma = \gamma_m\frac{\theta_w}{\theta_m}(1 - \ln(\frac{\theta_w}{\theta_m})) \\ V_a = \frac{b^3}{\theta_w} \end{cases} \tag{15}$$

The integration of the rate equations is performed with the MATLAB software version R2016b. The simulation results and discussion are presented in the following section.

4. Results and discussion

4.1. Model input parameters for AA1050 Al alloy

The initial average subgrain size δ_0 is set to 100 μm, and the initial subgrain boundary misorientation is assigned a non-zero value of 0.05°. The value of the activation energy Q is 142 kJ.mol^{-1} for pure Al [54]. The energy of HAGBs γ_m is taken as 0.324 J.m^{-2}, as suggested by Murr [55]. The activation energy for self-diffusion in Al [56] is $2\cdot10^{-19}$ J.atom^{-1}. The model input parameters of the subgrain size evolution model have been reported in a previous paper [42].

The fraction coefficient α_s is taken as 0.5 and the saturated misorientation angle with continuing deformation θ_{sat} is 5°. The material constants c_2 and c_3 are set to 0.75 and 50, respectively. The basic yield strength σ_0=1.1$[\dot{\varepsilon}\cdot\exp(Q/RT)]^{0.1}$. The strengthening coefficient α is taken as 0.2. The other input parameters for the model are summarized in Table 1.

Table 1. List of input parameters for AA1050 Al alloy

Symbol	Name	Unit	Value	Ref.
ν	Poisson's ratio	-	0.347	[57]
G	Shear modulus	MPa	29438.4−15.052T	[58-59]
b	Burgers vector	m	$2.86 \cdot 10^{-10}$	[60]
M	Taylor factor	-	3.06	[61]
Q_{vac}	Activation energy for vacancy formation	eV	0.67	[62]
Q_d	Activation energy for pipe diffusion	$J.mol^{-1}$	$83.2 \cdot 10^3$	[46]
D_{d0}	Pre-exponential factor for pipe diffusion	$m^2.s^{-1}$	$1.5 \cdot 10^{-6}$	[46]
ν_D	Debye frequency	s^{-1}	$1 \cdot 10^{13}$	[48]
A	A parameter	-	$1.8\exp(0.0066T)$	This work
B	B parameter	-	3	This work
C	C parameter	-	$1 \cdot 10^{-3}$	This work
f_r	Material coefficient related to subgrain refinement	-	$3.5 \cdot 10^9[\dot{\varepsilon}\exp(Q/RT)]^{-0.21}$	This work
f_c	Material coefficient related to subgrain coarsening	-	$10000[\dot{\varepsilon}\exp(Q/RT)]^{0.55}$	This work
f_i	fraction of interior dislocations	-	0.95	This work
f_w	fraction of wall dislocations	-	0.05	This work

4.2. Model application and discussion

4.2.1 Experimental

The material investigated in this research is an AA1050 aluminum alloy provided by Neuman Aluminium Austria GmbH (Marktl, Austria). Single-pass isothermal compression experiments are conducted at temperatures of 300 °C, 400 °C and 500 °C, and strain rates of 0.01 s^{-1} and 0.1 s^{-1}, using a deformation dilatometer DIL 805 A/D (Hüllhorst, Germany).

The corresponding experimental results are presented in Fig. 2. The detailed parameters of the electron backscatter diffraction (EBSD) experiment are reported in a previous publication [20]. A duplex subgrain/grain structure is observed, with the recovered microstructure showing numerous low-angle subgrains within the elongated parent grains due to DRV. Additionally, some recrystallized grains have formed as a result of DRX. These features are characteristics of a dominant CDRX mechanism [9-12].

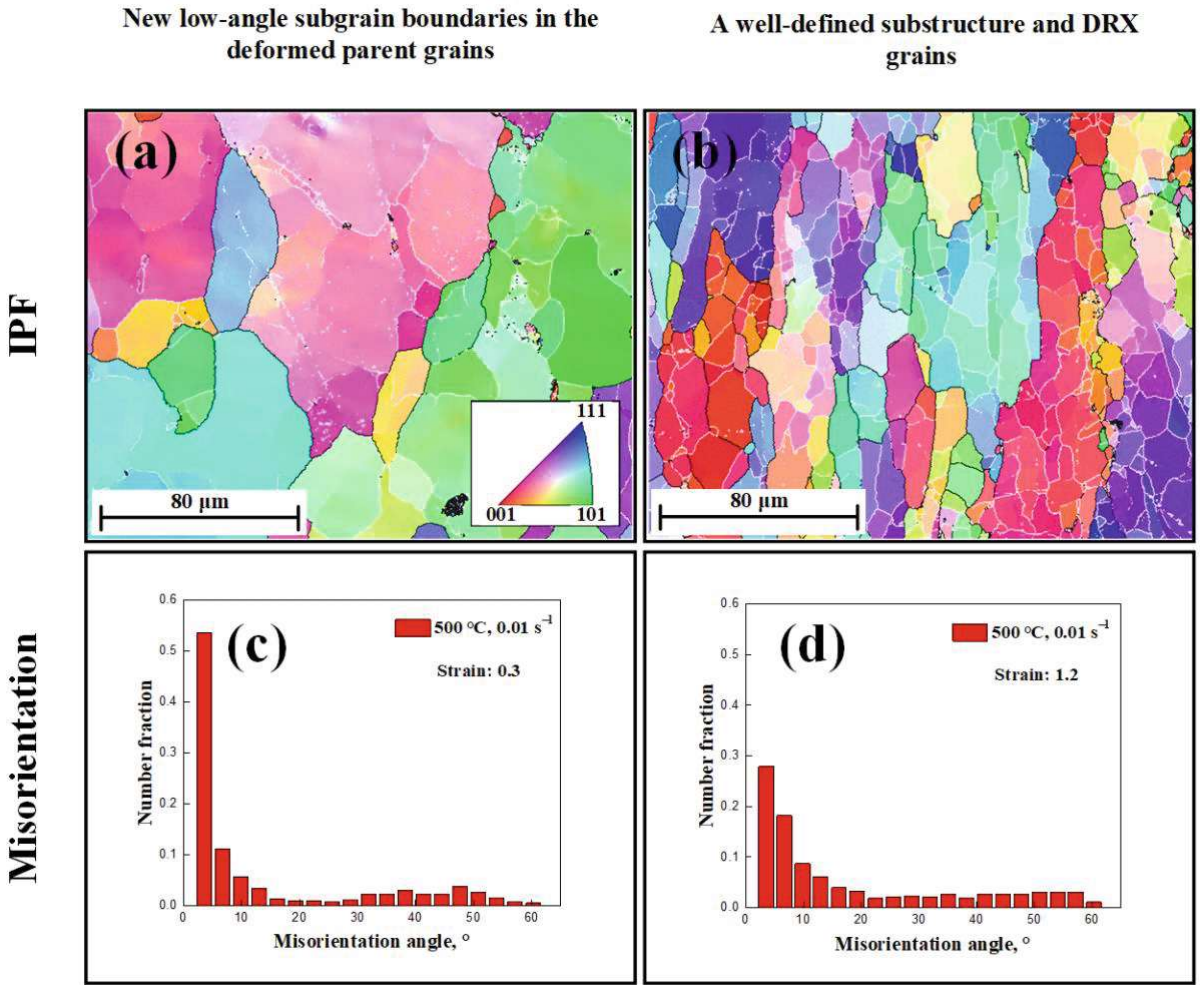

Fig. 2. EBSD images of AA1050 Al alloy deformed to a different strain at a temperature of 500 °C and a strain rate of 0.01 s^{-1}: (a)-(b) inverse pole figure (IPF) maps of the specimens deformed with strain 0.3 and 1.2, and (c)-(d) corresponding distribution histograms of misorientation angle.

The refinement of subgrains plays a crucial role, with the average subgrain size being highly sensitive to the deformation parameters [42]. The average size of the newly recrystallized grains is nearly identical to that of the subgrains, further supporting the transformation of low-angle subgrain boundaries into HAGBs, and in agreement with results from Huang and Logé [10]. As plastic strain increases, the gradual accumulation of dislocations along subgrain boundaries accelerates the formation of HAGBs, thereby increasing the average misorientation angle. Fig. 2(c)-(d) shows the corresponding distribution of misorientation angles under various strains. The low-angle subgrain boundaries represent the major fraction for both strain conditions, accounting for 75% and 65%, respectively. This observation indicates that subgrain boundaries continue to form extensively even at high strain. Additionally, a gradual increase in subgrain boundary misorientation is observed with increasing strain.

4.2.2 Flow curves

The flow curves obtained from the experiments are represented by symbols in Fig. 3. Subsequent simulations are performed using MATLAB software with one single set of input parameters (refer to Section 4.1) for all deformation conditions.

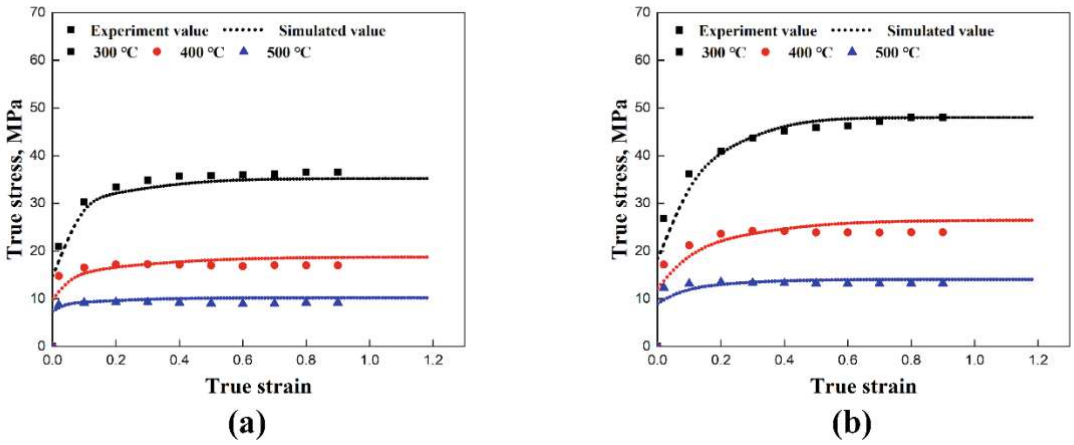

Fig. 3. The comparison between the experimental and simulated values of the flow stress with different deformation conditions of (a) 0.01 s^{-1}, and (b) 0.1 s^{-1}.

At the onset of deformation, work hardening (WH) dominates, caused by the multiplication and tangling of dislocations, which results in a continuous increase in flow stress. Simultaneously, numerous new subgrain boundaries are formed during compression, resulting in a rapid reduction of the average subgrain size [9-10]. As deformation commences, the dynamic softening mechanisms become increasingly prominent and eventually balance the continuous generation of dislocations [34-39]. The analysis indicates that the dislocation-based model potentially reproduces the measured flow curves.

To further evaluate the performance of the dislocation-based model, the correlation coefficient (R) and root mean square error ($RMSE$) [63] are evaluated as

$$R = \frac{\sum_{i=1}^{N}(\delta_{ei}-\bar{\delta}_e)(\delta_{ci}-\bar{\delta}_c)}{\sqrt{\sum_{i=1}^{N}(\delta_{ei}-\bar{\delta}_e)^2 \sum_{i=1}^{N}(\delta_{ci}-\bar{\delta}_c)^2}}, \tag{16}$$

$$RMSE = \sqrt{\frac{1}{N}\sum_{i=1}^{N}(\delta_{ci} - \delta_{ei})^2} \cdot 100\%, \tag{17}$$

where δ_{ci} represents the calculated flow stress, δ_{ei} represents the experimental flow stress, $\bar{\delta}_c$ is the average calculated flow stress, $\bar{\delta}_e$ is the average experimental flow stress, and N is the total number of data points used in this study. The corresponding error analysis for different tested conditions is shown in Fig. 4. The values of R and $RMSE$ are 0.98 and 2.0 MPa, respectively.

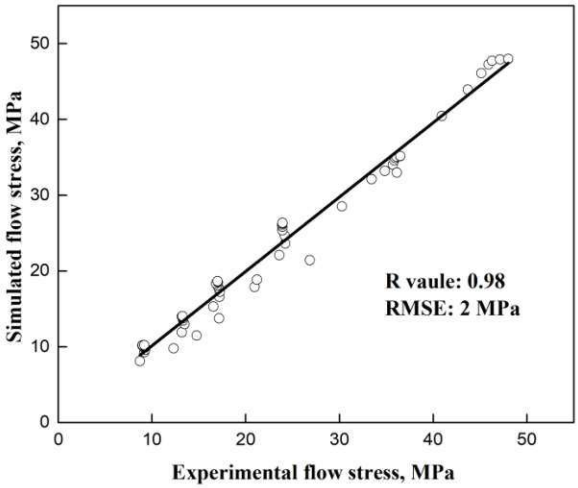

Fig. 4. Error analysis for the dislocation-based model

4.2.3 Evolution of dislocation density

By numerically solving Eq. (2) and Eq. (7), the dislocation densities in both cell walls and cell interiors are obtained and the total dislocation density is calculated using Eq. (1). Fig. 5 illustrates the simulated total dislocation density, as well as the dislocation densities in cell walls and cell interiors, at the temperature of 400 ℃ and a strain rate of 0.1 s^{-1}. The simulation results presented in Fig. 5 indicate that the interior dislocation density increases rapidly during the initial stages of deformation. This trend is easily reasoned when considering the hardening and softening mechanisms. As deformation progresses, the interior dislocation density reaches a plateau, reflecting a balance between the generation and annihilation of interior dislocations, in agreement with the observations of Prasad et al. [64].

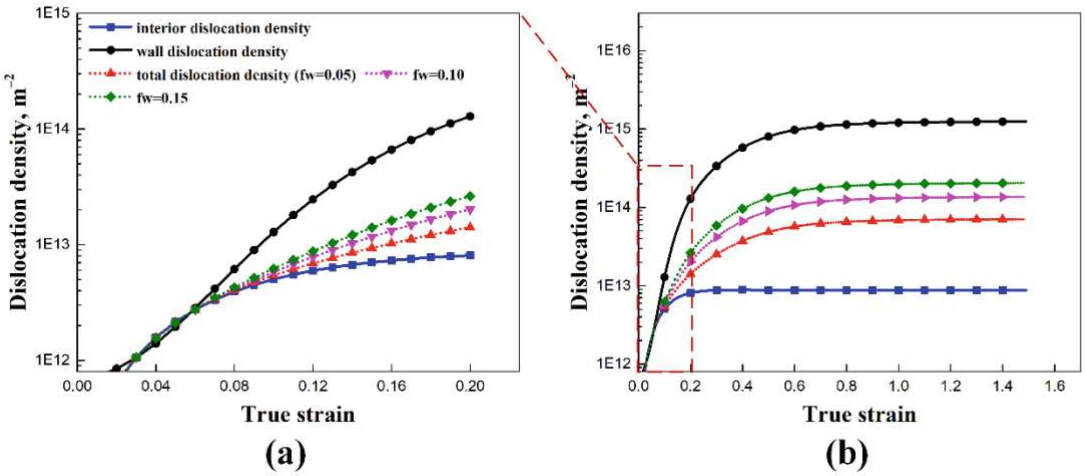

Fig. 5. Simulated total dislocation density (ρ_t), dislocation densities of cell walls (ρ_w) and cell

interiors (ρ_i) at 400 °C/0.1 s^{-1} of (a) strain 0.2 (the initial stage), and (b) strain 1.5.

As illustrated in Fig. 5, the wall dislocation density also increases rapidly in the early stages. Wall dislocations are closely associated with subgrain formation and misorientation angles, which leads to a distinct plateau in their development at larger strains. During compression, the density of wall dislocations rises as subgrains continue to form, reflecting the transformation of mobile interior dislocations into wall dislocations. The simulation results are consistent with the established 3IVM model [29,65], wherein the density of wall dislocations is calculated based on the annihilation of dipole dislocations ρ_{dip}, as $d\rho_w/dt = (1/f_w)(d\rho_{dip}/dt)$.

The simulated total dislocation density using different coefficients for the cell wall fraction f_w (Eq. (1)), is displayed in Fig. 5 by the dash-dotted lines. The total dislocation densities increase when increasing f_w, which leads to an increase in flow stress in the end.

Fig. 6 and Fig. 7 present the simulated results for the interior and wall dislocation densities at other deformation conditions. The dislocation density increases with decreasing temperature or increasing strain rate. Low temperatures promote the accumulation of dislocations and reduce their annihilation rate, resulting in a higher dislocation density, in accordance with the conclusions of Yang et al. [20,42]. Furthermore, according to Taylor's strength equation, the dislocation density decreases as temperature increases. Similarly, high strain rates promote the formation and rotation of low-angle subgrains and dislocation cells, which is consistent with findings reported by Sakai et al [9].

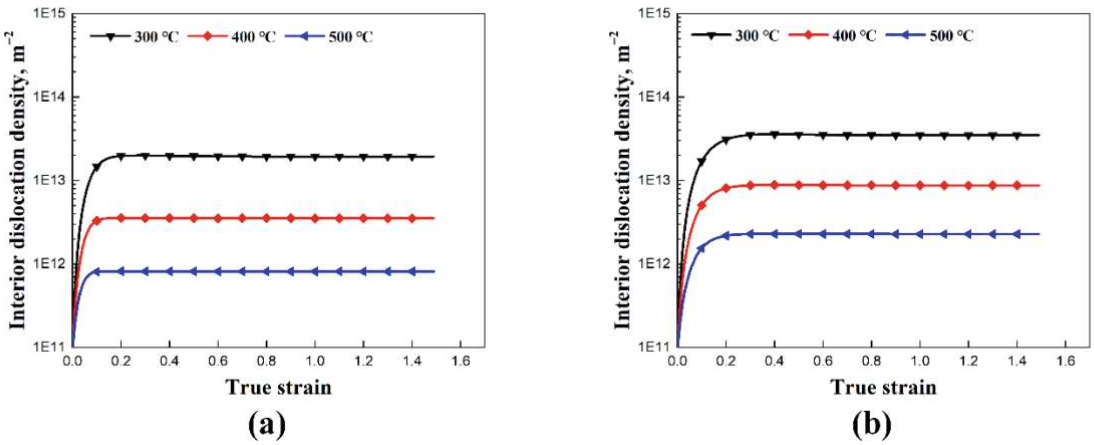

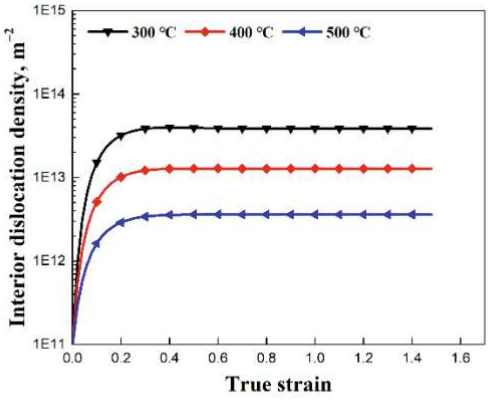

Fig. 6. Simulated interior dislocation density (ρ_i) at different deformation conditions: (a) 0.01 s^{-1}, (b) 0.1 s^{-1}, and (c) 1 s^{-1}.

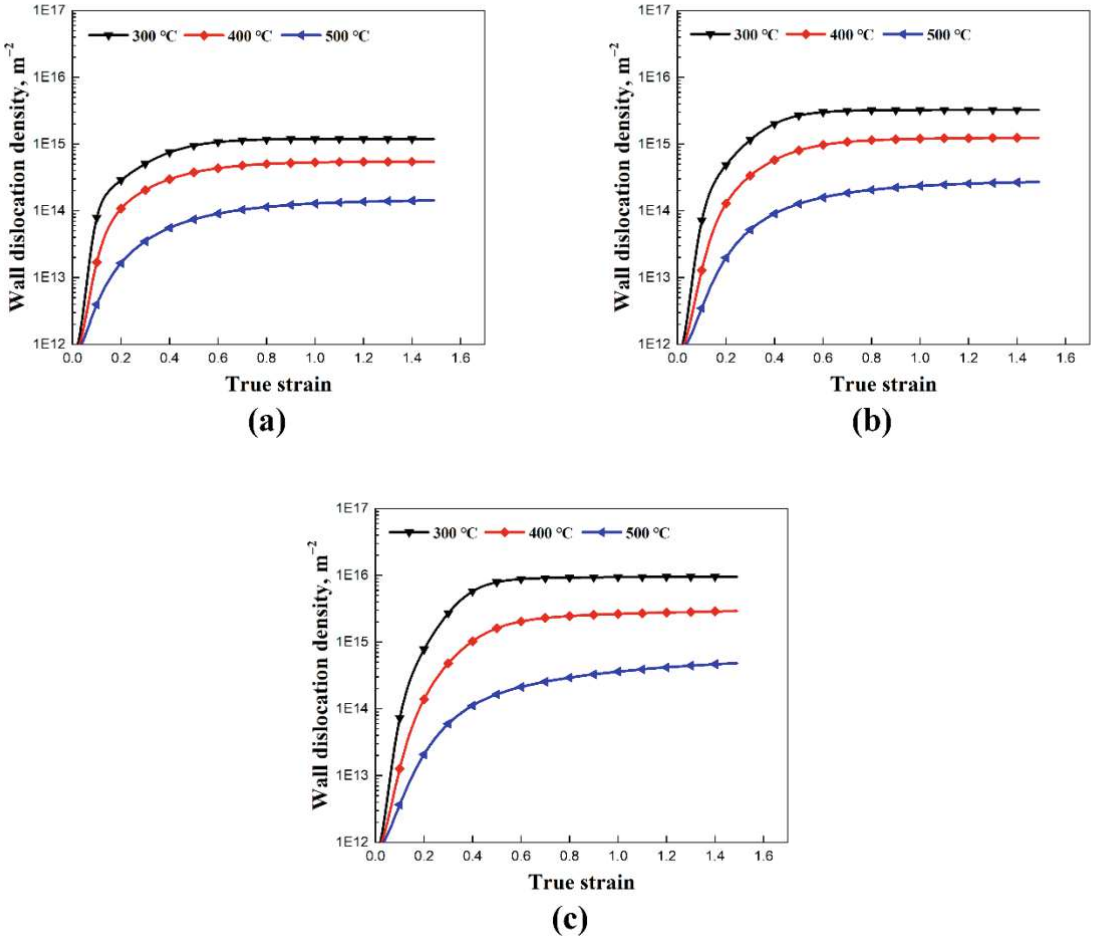

Fig. 7. Simulated wall dislocation density (ρ_w) at different deformation conditions: (a) 0.01 s^{-1}, (b) 0.1 s^{-1}, and (c) 1 s^{-1}.

4.2.4 Evolution of average subgrain size and subgrain misorientation angle

Fig. 8 shows the simulated results for the average subgrain size evolution, accounting for both, refinement and thermal coarsening of subgrains. The subgrain size gradually decreases

and nearly saturates at a constant value, which is consistent with findings in the literature [1, 9-10, 42, 48]. Subgrain refinement caused by continuous new subgrain formation is accompanied by subgrain growth at high temperatures. The migration of subgrain boundaries leads to thermally induced coarsening of subgrains, achieving a dynamic balance at higher strains [9-10].

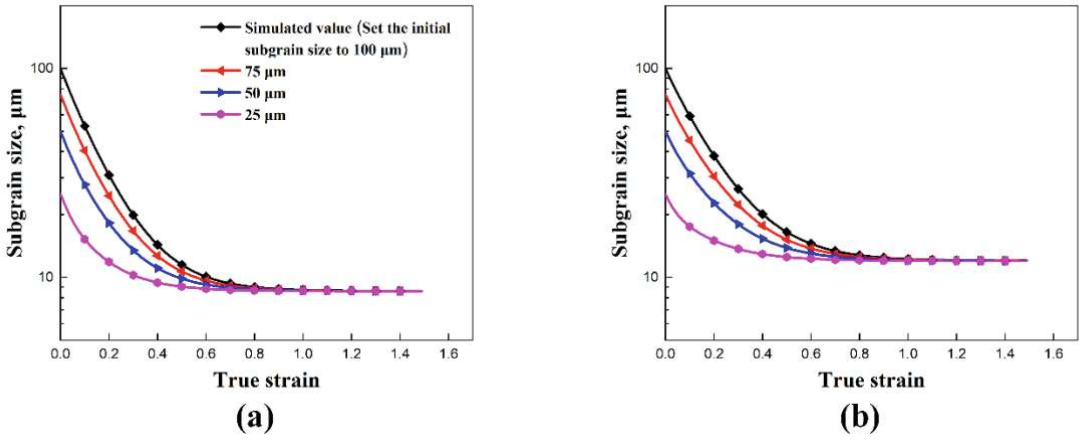

Fig. 8. (a). Evolution of simulated average subgrain size under various deformation temperatures and strain rates of (a) 350 ℃/0.01 s^{-1}, and (b) 400 ℃/0.01 s^{-1}.

The simulated results in Fig. 9 show that the average subgrain misorientation increases continuously during deformation across all temperatures and strain rates. As suggested by McQueen and Kassner [52], the average misorientation angle in Al increases rapidly due to the formation of dislocation dipoles and the absorption of mobile dislocations. This increase continues until a critical misorientation angle is reached, which subsequently leads to the transformation of these boundaries into HAGBs. The evolution of subgrain misorientation can also be described by the classical relationship $\theta = b/L$, where L is the spacing distance between two neighboring dislocations, typically associated with the dislocation density [34-39].

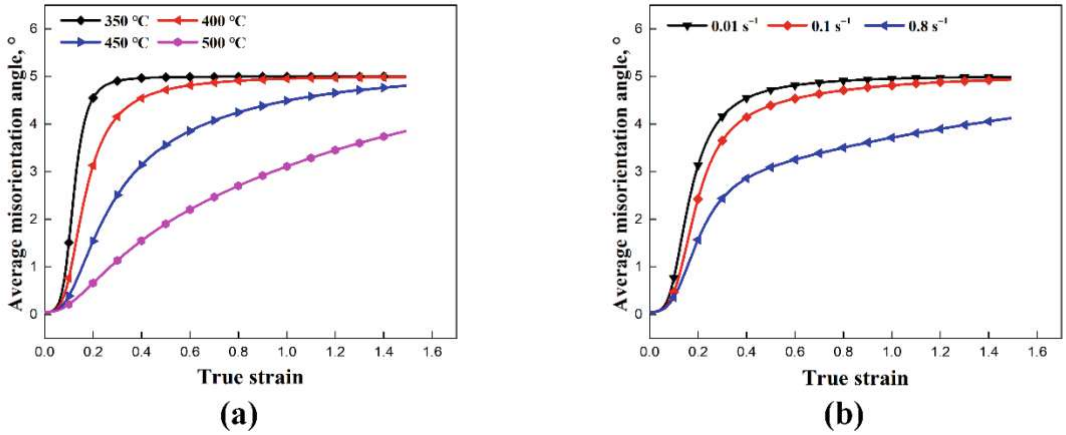

Fig. 9. Simulated average subgrain misorientation angle (θ_w) at different deformation conditions: (a) 0.01 s^{-1}, and (b) 400 °C.

Our results for the deformed microstructure are in line with the measured evolution of average subgrain size and average misorientation angle of subgrain boundaries as dislocations accumulate [20, 42]. A decrease in temperature promotes the generation of low-angle subgrain boundaries, resulting in a rapid increase in subgrain misorientation. For Al and Al alloys, the annihilation of dislocations and subgrain boundary migration are more likely to occur at elevated temperatures [10-12].

4.3 Model application to an AA5052 alloy

To verify the applicability of the proposed model across various Al alloys, the present model framework is tested against experimental results for the AA5052 Al alloy from Gourdet [66]. The experimental flow curves have been measured under different deformation conditions: Three temperatures at a strain rate of 0.01 s^{-1} and three strain rates at a temperature of 333 °C, as shown in Fig. 10. The comparison shows good agreement between the experimental and simulated flow stress values (Fig. 10). The input parameters for the constitutive model of the AA5052 alloy are provided below.

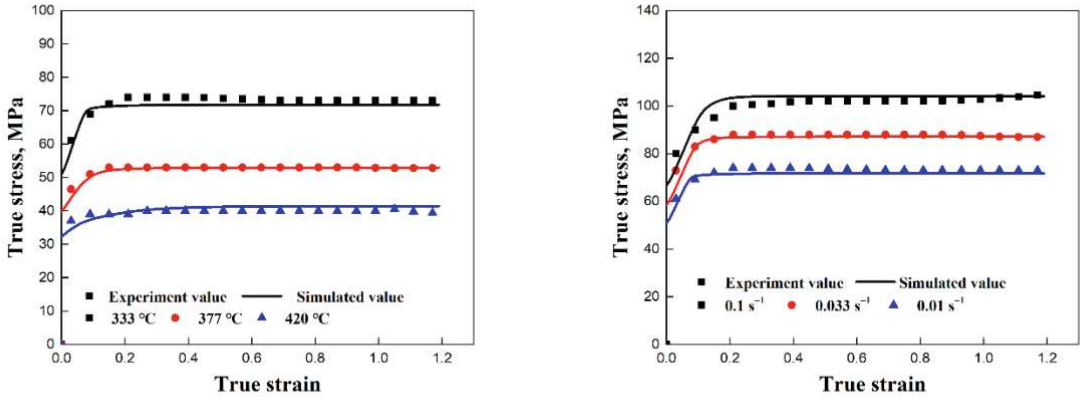

Fig. 10. The comparison between the experimental and simulated values of the flow stress with different deformation conditions of (5052 Al alloy): (a) 0.01 s^{-1}, and (b) 333 °C.

The dislocation density evolution parameters *A*, *B*, *C,* and other parameters are chosen to best fit the AA5052 alloy results. The parameters that differ from that of the AA1050 alloy are shown in Table II, the others remain the same as the ones in Table I. The value of the activation energy Q is 156 kJ.mol^{-1} for the AA5052 alloy [67]. Due to the difference in flow stress, the value of the material coefficient c_1 is taken as 80, and the calculation of $\bar{\sigma}_s$ is temperature and strain rate-dependent, with $\bar{\sigma}_s = 1.20[\dot{\varepsilon} \cdot \exp(Q/RT)]^{0.15}$ MPa. The basic yield strength σ_0 is described as $\sigma_0 = 2.1[\dot{\varepsilon} \cdot \exp(Q/RT)]^{0.12}$.

Table II. List of different input parameters for AA5052 Al alloy

Symbol	Name	Unit	Value	Ref.
A	A parameter	(-)	$0.005\exp(0.015T)$	This work
B	B parameter	(-)	2	This work
C	C parameter	(-)	1×10^{-3}	This work
f_i	Fraction of interior dislocations	(-)	0.9	This work
f_w	Fraction of wall dislocations	(-)	0.1	This work

5. Conclusions

A dislocation-based model framework for the deformation of Al alloys based on substructure evolution is proposed. The model is designed to simulate the micro/substructural changes occurring during high-temperature compression, including the evolution of dislocation

density, subgrain size, misorientation angles, and flow stress. The key findings of this study are:

(1) The main microstructural evolution mechanisms observed in Al alloys are summarized, including dislocation densities, low-angle subgrain size, subgrain boundary misorientation, and flow stress. These microstructural variables are individually simulated and compared.

(2) EBSD experiments are conducted to support the microstructure analysis. The mechanism of subgrain boundary formation and corresponding microstructural evolution are discussed. The results describe the dependence of the microstructural variables on deformation conditions such as temperature, strain rate, and strain.

(3) A physical dislocation model is proposed with separate populations of interior and wall dislocation densities.

(4) Special substructure models are developed and combined for the subgrain size, misorientation angle, and macroscopic mechanical response. These models are based on physically-based parameters.

(5) The dislocation-based model framework is successfully applied and validated for AA1050 and AA5052 aluminum alloys. The model consistently predicts flow curves and substructure evolution.

Author Contributions: Conceptualization, Q.Y. and E.K.; methodology, Q.Y., T.W., and E.K.; validation, Q.Y. and E.K.; formal analysis, Q.Y.; investigation, Q.Y. and T.W.; resources, E.K. and T.W.; data curation, Q.Y. and T.W.; writing—original draft preparation, Q.Y. and E.K.; writing—review and editing, E.K.; visualization, Q.Y., T.W., and E.K.; supervision, E.K.; project administration, E.K.; funding acquisition, Q.Y. and E.K. All authors have read and agreed to the published version of the manuscript.

Funding: Open access funding is provided by the library of TU Wien (TUW).

Data Availability Statement: The raw data supporting the conclusions of this article will be made available by the authors on request.

Acknowledgments: Qi Yang appreciates the financial support from the State Scholarship Fund of China (No. 202107710006) during his PhD at TU Wien.

Conflicts of Interest: The authors declare no conflicts of interest.

References

1. F.J. Humphreys, and M. Hatherly. Recrystallization and Related Annealing Phenomena. 2004, 2nd edn. Elsevier, Oxford.
2. R.D. Doherty, D.A. Hughes, F.J. Humphreys, J.J. Jonas, D. Juul Jensen, M.E. Kassner, T.R. McNelley, H.J. McQueen, and A.D. Rollet. Current issues in recrystallization: a review. Mater. Sci. Eng., A, 1997, vol. 238, pp. 219-274.
3. P. Choudhury, K. Das, and S. Das, Evolution of as-cast and heat-treated microstructure of a commercial bearing alloy. Mater. Sci. Eng., A, 2005, vol. 398, pp. 332-343.
4. T. Sakai, and J.J. Jonas. Dynamic recrystallization: Mechanical and microstructural considerations. Acta Metall., 1984, vol. 32, pp. 189-209.
5. H. Mirzadeh. Grain refinement of magnesium alloys by dynamic recrystallization (DRX): A review. J. Mater. Res. Technol., 2023, vol. 25, pp. 7050-7077.
6. W.S. Xia, X.B. Zhao, L. Yue, and Z. Zhang. Microstructural evolution and creep mechanisms in Ni-based single crystal superalloys: A review. J. Alloys Compd., 2020, vol. 819, pp. 152954.
7. W. Liu, Y.H. Zhao, Y.T. Zhang, C. Shuai, L.W. Chen, Z.Q. Huang, and H. Hou. Deformation-induced dynamic precipitation of 14H-LPSO structure and its effect on dynamic recrystallization in hot-extruded Mg-Y-Zn alloys. Int. J. Plast., 2023, vol. 164, pp. 103573.
8. E. Tsekpuia, A. Guery, N. Gey, and S. Berbenni. A microstructure-based three-scale homogenization model for predicting the elasto-viscoplastic behavior of duplex stainless steels. Int. J. Plast., 2023, vol. 164, pp. 103575.
9. T. Sakai, A. Belyakov, R. Kaibyshev, H. Miura, and J.J. Jonas. Dynamic and post-dynamic recrystallization under hot, cold and severe plastic deformation conditions. Prog. Mater. Sci., 2014, vol. 60, pp. 130-207.
10. K. Huang, and R.E. Logé. A review of dynamic recrystallization phenomena in metallic materials. Mater. Design, 2016, vol. 111, pp. 548-574.
11. D. Raabe, 23 - Recovery and Recrystallization: Phenomena, Physics, Models, Simulation, in: D.E. Laughlin, K. Hono (Eds.), Physical Metallurgy, Elsevier, Oxford, 2014, pp. 2291-2397.
12. T. Sakai, H. Miura, A. Goloborodko, and O. Sitdikov. Continuous dynamic recrystallization during the transient severe deformation of aluminum alloy 7475. Acta Mater., 2009, vol. 57, pp. 153-162.
13. G. Maizza, R. Pero, M. Richetta, and R. Montanari. Continuous dynamic recrystallization (CDRX) model for aluminum alloys. J. Mater. Sci., 2018, vol. 53, pp. 4563-4573.

14. T. Sheppard and M. G. Tutcher. Development of duplex deformation substructure during extrusion of a commercial Al-5Mg-0.8Mn alloy. Met. Sci., 1980, vol.14, pp. 579-590.
15. F. R. Castro-Fernández and C. M. Sellars. Static recrystallisation and recrystallisation during hot deformation of Al-1Mg-1Mn alloy. Mater. Sci. Technol., 1988, vol.4, pp. 621-627.
16. H.J. McQueen, O. Knustad, N. Ryum and J.K. Solberg. Microstructural evolution in Al deformed to strains of 60 at 400°C. Scr. Mater., 1985, vol.19, pp. 73-78.
17. W. Blum, Q. Zhu, R. Merkel and H.J. McQueen. Geometric dynamic recrystallization in hot torsion of Al-5Mg-0.6Mn (AA5083). Mater. Sci. Eng., A, 1996, vol. 205, pp. 23-30.
18. R. Kaibyshev, and S. Malopheyev. Mechanisms of dynamic recrystallization in aluminum alloys. Mater. Sci. Forum, 2014, vol. 794, pp. 784-789.
19. D. Canelo-Yubero, Z. Kovács, J.F. Thierry Simonet Fotso, D. Tolnai, N. Schell, I. Groma, and C. Poletti. In-situ characterization of continuous dynamic recrystallization during hot torsion of an Al-Si-Mg alloy. J. Alloys Compd., 2020, vol. 822, pp. 153282.
20. Q. Yang, T. Wojcik, and E. Kozeschnik. Continuous dynamic recrystallization and deformation behavior of an AA1050 aluminum alloy during high-temperature compression. Metals, 2024, vol. 14, pp. 889.
21. H. Mecking, and U.F. Kocks. Kinetics of flow and strain-hardening. Acta Metall., 1981, vol. 29, pp. 1865-1875.
22. M. Goerdeler, and G. Gottstein. A microstructural work hardening model based on three internal state variables. Mater. Sci. Eng., A, 2001, vol. 309, pp. 377-381.
23. P. Sherstnev, P. Lang, and E. Kozeschnik: in Eur. Congr. Comput. Methods Appl. Sci. Eng. (ECCOMAS 2012), 10.-14.9.2012, J. Eberhardsteiner et.al., ed., Vienna, Austria, 2012, pp. 1-8.
24. U. F. Kocks. A statistical theory of flow stress and work-hardening. Philos. Mag., 1966, vol. 13, pp. 541-566.
25. Y. Bergström. A dislocation model for the stress-strain behaviour of polycrystalline α-Fe with special emphasis on the variation of the densities of mobile and immobile dislocations. Mater. Sci. Eng., 1970, vol. 5, pp. 193-200.
26. Y. Bergström, and W. Roberts. The dynamical strain ageing of α-iron: effects of strain rate and nitrogen content in the jerky-flow region. Acta Metall., 1973, vol. 21, pp. 741-745.
27. H. Mecking, and Y. Estrin. The effect of vacancy generation on plastic deformation. Scripta Metall., 1980, vol. 14, pp. 815-819.

28. U. F. Kocks, and H. Mecking. Physics and phenomenology of strain hardening: the FCC case. Prog. Mater. Sci., 2003, vol. 48, pp. 171-273.
29. F. Roters, D. Raabe, and G. Gottstein. Work hardening in heterogeneous alloys-a microstructural approach based on three internal state variables. Acta Metall., 2000, vol. 48, pp. 4181-4189.
30. H.J McQueen, and N.D Ryan. Constitutive analysis in hot working. Mater. Sci. Eng., A, 2002, vol. 322, pp. 43-63.
31. Y.C. Lin, and X.M. Chen. A critical review of experimental results and constitutive descriptions for metals and alloys in hot working. Mater. Des., 2011, vol. 32, pp. 1733-1759.
32. F. Siciliano, Jr., K. Minami, T. M. Maccagno, and J. J. Jonas. Mathematical modeling of the mean flow stress, fractional softening and grain size during the hot strip rolling of C-Mn steels. ISIJ Int., 1996, vol. 36, pp. 1500-1506.
33. J. J. Jonas, X. Quelennec, L. Jiang, and É. Martin. The Avrami kinetics of dynamic recrystallization. Acta Mater., 2009, vol. 57, pp. 2748-2756.
34. S. Gourdet and F. Montheillet. A model of continuous dynamic recrystallization. Acta Metall., 2003, vol. 51, pp. 2685-2699.
35. Z.C. Sun, H.L. Wu, J. Cao, and Z.K. Yin. Modeling of continuous dynamic recrystallization of Al-Zn-Cu-Mg alloy during hot deformation based on the internal-state-variable (ISV) method. Int. J. Plast., 2018, vol. 106, pp. 73-87.
36. S.F. Chen, D.Y. Li, S.H. Zhang, H.N. Han, H.W. Lee and M.G. Lee. Modelling continuous dynamic recrystallization of aluminum alloys based on the polycrystal plasticity approach. Int. J. Plast., 2020, vol. 131, pp. 102710.
37. R.H. Buzolin, M. Lasnik, A. Krumphals, and M.C. Poletti. A dislocation-based model for the microstructure evolution and the flow stress of a Ti5553 alloy. Int. J. Plast., 2021, vol. 136, pp. 102862.
38. Y.B. Li, B. Gu, S. Jiang, Y.Q. Liu, Z.S. Shi, and J.G. Lin. A CDRX-based material model for hot deformation of aluminium alloys. Int. J. Plast., 2020, vol. 134, pp. 102844.
39. F. Chen, X. Tian, G.S. Wu, H.J. Zhu, H.A. O and Z.S. Cui. Coupled quantitative modeling of microstructural evolution and plastic flow during continuous dynamic recrystallization. Int. J. Plast., 2022, vol. 156, pp. 103372.
40. C. Poletti, M. Rodriguez-Hortalá, M. Hauser, and C. Sommitsch. Microstructure development in hot deformed AA6082. Mater. Sci. Eng., A, 2011, vol. 528, pp. 2423-2430.

41. C. Sellars, and Q. Zhu, Microstructural modelling of aluminium alloys during thermomechanical processing, Mater. Sci. Eng., A, 2000, vol. 280, pp. 1-7.
42. Q. Yang, T. Wojcik and E. Kozeschnik. Subgrain size modeling and substructure evolution in an AA1050 aluminum alloy during high-temperature compression. Materials, 2024, vol. 17, pp. 4385.
43. J. Kreyca, and E. Kozeschnik. State parameter-based constitutive modelling of stress strain curves in Al-Mg solid solutions. Int. J. Plast., 2018, vol. 103, pp. 67-80.
44. H. Buken, and E. Kozeschnik. Modeling static recrystallization in Al-Mg alloys. Metall. Mater. Trans. A, 2021, vol. 52, pp. 544-552.
45. S. Brinckmann, R. Sivanesapillai, and A. Hartmaier. On the formation of vacancies by edge dislocation dipole annihilation in fatigued copper. Int. J. Fatigue, 2011, vol. 33, pp. 1369-1375.
46. G Stechauner, and E Kozeschnik. Assessment of substitutional self-diffusion along short-circuit paths in Al, Fe and Ni. Calphad, 2014, vol. 47, pp. 92-99.
47. J. Peŝiĉka A. Dronhofer, and G. Eggeler. Free dislocations and boundary dislocations in tempered martensite ferritic steels. *Mater. Sci. Eng., A*, 2004, vol. 387, pp. 176-180.
48. E. Nes. Modelling of work hardening and stress saturation in FCC metals. Prog. Mater. Sci., 1998, vol. 41, pp. 129-193.
49. K. Marthinsen, and E. Nes. Modelling strain hardening and steady state deformation of Al-Mg alloys. Mater. Sci. Technol., 2001, vol. 17, pp. 376-388.
50. Y. Huang, and F.J. Humphreys. Subgrain growth and low angle boundary mobility in aluminium crystals of orientation {110}〈001〉. Acta Mater., 2000, vol. 48, pp. 2017-2030.
51. T. Furu, R. Orsund, and E. Nes. Substructure evolution during different hot deformation processes of commercial non-heat treatable aluminium alloys. Mater. Sci. Eng., A, 1996, vol. 214, pp. 122-132.
52. H.J. McQueen, and M.E. Kassner. Comments on 'a model of continuous dynamic recrystallization' proposed for aluminum. Scr. Mater., 2004, vol. 51, pp. 461-465.
53. G.I. Taylor. The Mechanism of Plastic Deformation of Crystals. Part I. Theoretical. Proc. R. Soc. Lond. A, 1934, vol. 145, pp. 362-387.
54. O.D. Sherby, R.H. Klundt, and A.K. Miller. Flow stress, subgrain size, and subgrain stability at elevated temperature. Metall. Trans. A, 1977, vol. 8, pp. 843-850.
55. L.E. Murr. Interfacial Phenomena in Metals and Alloys. Addison-Wesley, Reading, MA, 1975.

56. T. Federighi. A possible determination of the activation energy for self-diffusion in aluminium. Philos. Mag., 1959, vol. 4, pp. 502-510.
57. J.P. Hirth, and J. Lothe. Theory of Dislocations. Krieger Publishing Company, 1991.
58. E.I. Galindo-Nava, and P.E.J. Rivera-Díaz-del-Castillo. A thermostatistical theory of low and high temperature deformation in metals. Mater. Sci. Eng., 2012, vol. 543, pp. 110-116.
59. H. Mecking, B. Nicklas, and N. Zarubova. A universal temperature scale for plastic flow. Acta Mater., 1986, vol. 34, pp. 527-535.
60. H. Frost, and M. Ashby. Deformation-mechanism Maps, first ed. Pergamon Press, Oxford, 1982.
61. Y. Bergström. The plastic deformation of metals-a dislocation model and its applicability. Rev. Powder Metall. Phys. Ceram., 1983, vol. 2, pp. 79-265.
62. P. Tzanetakis, J. Hillairet, and G. Revel. The formation energy of vacancies in aluminium and magnesium. physica status solidi (b), 1976, vol. 75, pp. 433-439.
63. H. Mirzadeh, J.M. Cabrera, and A. Najafizadeh. Modeling and prediction of hot deformation flow curves. Metall. Mater. Trans. A, 2012, vol. 43, pp. 108-123.
64. G.V.S.S. Prasad, M. Goerdeler, and G. Gottstein. Work hardening model based on multiple dislocation densities. Mater. Sci. Eng., 2005, vol. 400, pp. 231-233.
65. M. Goerdeler, and G. Gottstein. A microstructural work hardening model based on three internal state variables. Mater. Sci. Eng., A, 2001, vol. 309, pp. 377-381.
66. S. Gourdet. Étude des mécanismes de recristallisation au cours de la déformation a chaud de l'aluminium. Matériaux. Doctoral dissertation, Ecole Nationale Supérieure des Mines de Saint-Etienne, 1997. Français.
67. B. Kowalski, A.J. Lacey, and C.M. Sellars. Correction of plane strain compression data for the effects of inhomogeneous deformation. Mater. Sci. Technol., 2003, vol. 19, pp. 1564-1570.